SHALE GAS/OIL RESERVOIR CHARACTERIZATION AND MATURITY DETERMINATION BASED ON VARIOUS EXPERIMENTAL ANALYSES

by

MD GOLAM KIBRIA

DISSERTATION

Submitted in partial fulfillment of the requirements

for the degree of Doctor of Philosophy at

The University of Texas at Arlington

May 2019

Arlington, Texas

Supervising Committee:

Qinhong Hu, Ph.D. Supervising Professor
John S Wickham, Ph.D.
Majie Fan, Ph.D.
William Ashley Griffith, Ph.D.
Cheng Luo, Ph.D.

ABSTRACT

SHALE GAS/OIL RESERVOIR CHARACTERIZATION AND MATURITY DETERMINATION BASED ON VARIOUS EXPERIMENTAL ANALYSES

Md Golam Kibria, Ph.D.

The University of Texas at Arlington, 2019

Supervising Professor: Qinhong Hu

Despite the successful shale hydrocarbon exploration and production in the U.S. started about 20 years ago, the producing wells experience a current low total recovery of tight oil (5%-10%) and shale gas (12%-30%). One of the critical obstacles to sustainable shale development is related to the low recovery factor, which still needs much investigation. Hydrocarbon movement through shale reservoirs is controlled by two factors related to pore structure: one is pore size distribution (geometry), and another one is pore connectivity (topology). This Ph.D. research is divided into three different projects: 1) The 1st one is to improve the understanding of shale reservoir nanopore structure and wettability characteristics of Woodford Shale. For this research I examine mineralogy, pore structure, wetting characteristics, imbibition behavior, and edge-accessible porosity with the following complementary tests: X-ray diffraction (XRD), mercury injection capillary pressure (MICP), contact angle measurement of various fluids, fluid imbibition into initially dry shale, and edge-accessible pore connectivity from vacuum saturation-high pressure impregnation with tracers-containing n-decane. The wettability and imbibition tests use both hydrophilic (DI water) and hydrophobic (n-decane) fluids; 2) the second research is to use Laser Raman spectra of kerogens, G (graphitic) and D (disordered) bands of disordered carbonaceous matter, to relate the thermal maturity of representative shale oil samples, with the intention of

establishing an empirical equation to determine thermal maturity directly using Laser Raman spectra with minimal sample preparation for potential 'on rig' use including the down-hole environment; 3) The third and last research is to investigate two different shale plays Haynesville and Pearsall Shale for an improved understanding of their petrophysical properties based on various experimental analyses. Overall, this dissertation will help to understand nanopore structure and wettability characteristics of unconventional shale, their nanopore structure characteristics and fluid flow behavior and establishing a method to determine thermal maturity directly using Laser Raman spectra.

ACKNOWLEDGMENTS

This thesis would not have been possible without the help, support and patience of dissertation committee chair Dr. Qinhong Hu and all committee members Dr. John S Wickham, Dr. William Ashley Griffith, Dr. Majie Fan, and Dr. Cheng Luo, to mention their advice and unsurpassed knowledge that helped me pull through. I am very much indebted to Dr. Qinhong Hu for the many valuable discussions that helped me understand my research and execute my experiments in the best possible way. The excellent advice and support of Dr. John S Wickham have been invaluable on the academic level, for which I am incredibly grateful. I want to thank Post-Doctoral scholar Dr. Souvik Das for providing experimental support and shear research knowledge during the research and writing.

I want to acknowledge the University of Texas at Arlington for providing me necessary financial support throughout my studies. I would like to thanks American Association of Petroleum Geologist (AAPG) for their graduate student research fund. I would also like to thank Southwest Section of American Association of Petroleum Geologist (AAPG) for providing me a scholarship for two consecutive years, which helped me immensely. Immense thanks to Gulf Coast Association of Geological Societies (GCAGS) for providing two successive years of a research grant for my experimental work. Special thanks to Dr. Asish R. Basu, Dept of Earth and Environmental Sciences to allowing me to use his laboratory.

We are grateful to Dr. Harry Rowe, Robert Villegas, Jordan Bevers, Paul Huggins, Marvin Dunbar, and Scott Leaseburge for their assistance in sample procurement. I want to thank Dr. Yuxiang Zhang, Troy Barber, Zeynep Doner, Nabil Mzee**,** Ashley Chang and Qiming Wang, who are as good friends, were always willing to help and give their best suggestions, encouragement, practical and scientific advice. It would have been a lonely lab without them.

TABLE OF CONTENTS

LIST OF FIGURES

Chapter 2

Chapter 3

Chapter 4

LIST OF TABLES

Chapter 2

Chapter 3

Chapter 4

Chapter 1: Introduction

Exploration and production of petroleum from shales in various basins in the United States have experienced significant growth over the last decade. This is largely due to scientific and technological improvements in hydraulic fracturing and horizontal drilling, which is changing the landscape of oil and gas industry worldwide (EIA, 2019). U.S. shale gas production was approximately 23 trillion cubic feet (Tcf) in 2018 and contributed 78% of the total gas production. This was a sharp increase compared to the 1.6 tcf produced in 2007 (EIA, 2019). Similarly, 2018 saw the highest level of oil production in the U.S. since 2009, mostly due to the growth in shale plays ("tight oil formations"), with close to 10.2 million barrels per day (EIA, 2019). However, most shale wells experience a sharp production decline after hydraulic fracturing or re-fracking in the first several years. Shale heterogeneity and the controls on the evolution of porosity, pore geometry and permeability are still incompletely understood, despite their influence on reservoir quality and liquid & gas movement in such a complex matrix.

In order to obtain sustained production and reduced decline rates, studies on the understanding of hydrocarbon migration behavior in tight shale have attracted much attention (Soeder, 1988; Javadpour et al., 2007; Makhanov et al., 2012; Jarvie, 2012; Dehghanpour et al., 2013; Slatt & O'Brien, 2011; Yuan et al., 2014; Zhou et al., 2014; Gao & Hu, 2016; Yang et al., 2017; 2019?). Shales have reservoir characteristics which can be represented as having poor macroscopic qualities and complex microscopic pore structures (Zou et al., 2012; Huang et al., 2017; Xiao et al., 2017). Geometric shape and size of pores, the distribution of pore throats diameter and their connectivity can be defined by their nano-pore system (Fu et al., 2015; Hu et al., 2017), and the role that such nanopores play in controlling hydrocarbon flow and transport has been investigated by several authors (Anovitz and Cole, 2015; Schmitt et al., 2015; Zhao et al., 2017;

Wang et al., 2017). For this reason, characterization of pore structure parameters, such as volume, surface area, shape, pore size distribution, connectivity and fractal dimensions, is critical in order to understand adsorption, desorption, diffusion and flow mechanism of hydrocarbons (Ross and Bustin, 2009; Chen et al., 2011; Hao et al., 2013; Hu et al., 2014). Commonly used petrophysical analyses on rocks include low-pressure nitrogen (N_2) gas physisorption, mercury injection capillary pressure (MICP), spontaneous fluid imbibition using different fluids, contact angle measurement, and vacuum saturation tests. The N_2 gas physisorption and MICP approaches are widely acknowledged to successfully quantify the porosity and pore volume in tight samples (Ross and Bustin., 2009; Lockes et al., 2012; Clarkson et al., 2013).

Another critical aspect of shale play assessment is the geochemical evaluation (screening), specifically, assessing the quantity, quality, and thermal maturity of sedimentary organic matter and their role in hydrocarbon generation, retention, and expulsion. The thermal maturity assessment of source-reservoir rocks is routinely performed using pyrolysis (T_{max}) and vitrinite reflectance (VR_r) data, though there are some other less common methods available, such as spore coloration index, solid bitumen reflectance and spectral micro-fluorescence (e.g., Tissot 1984; Taylor et al., 1998). Raman spectroscopy is potentially an attractive technique for non-destructive and rapid maturity evaluation of hydrocarbon source rocks (Kelemen and Fang, 2001; Marshall et al., 2012; Wilkins et al., 2014). Raman Spectroscopy enables the analysis of data where the peaks of carbon are resolved into Gaussian bands (Wilkins et al., 2014). The Raman spectrums of the carbon materials show two primary bands: G (graphitic) band near ~ 1580 cm^{-1} and D (disordered) band around ~ 1350 cm^{-1} (Tuinstra and Koenig, 1970; Gruber et al., 1994; Spotl et al., 1998; Kelemen and Fang, 2001; Marshall et al., 2012; Schito et al., 2017).

This dissertation work is separated into three chapters covering the investigation of petrophysical properties and thermal maturity of shale. Chapter 2 provides a case study of the e pore structure characterization and fluid flow behavior of samples from the Woodford shale formation, West Texas, using MICP, wettability, and spontaneous imbibition. Chapter 3 presents a method of applying Raman spectroscopy for identifying shale samples thermal maturity and its comparison with vitrinite reflectance and pyrolysis. Chapter 4 uses similar methodologies to Chapter 2 for assessing petrophysical characteristics of Haynesville and Pearsall shale from Texas.

References:

Anovitz, L.M., Cole, D.R., Sheets, J.M., Swift, A., Elston, H.W., Welch, S., Chipera, S.J., Littrell, K.C., Mildner, D.F.R. and Wasbrough, M.J. 2015. Effects of maturation on multiscale (nanometer to millimeter) porosity in the Eagle Ford Shale. Interpretation, 3(3), pp.SU59-SU70.

Carvajal-Ortiz, H. and Gentzis, T., 2015. Critical considerations when assessing hydrocarbon plays using Pyrolysis and organic petrology data: Data quality revisited. Int. J. Coal Geol.,152, 13-122.

Clarkson, C.R., Solano, N., Bustin, R.M., Bustin, A.M.M., Chalmers, G.R.L., He, L., Melnichenko, Y.B., Radlin´ ski, A.P., Blach, T.P. (2013). Pore structure characterization of North American shale gas reservoirs using USANS/SANS, gas adsorption, and mercury intrusion. Fuel, 103, 606–616.

Energy Information Administration (EIA), 2019. Annual Energy Outlook 2019: With Projections to 2050, released on January 24, 2019.

Gruber, T., Zerda, T.W. and Gerspacher, M. 1994. Raman studies of heat-treated carbon blacks. Carbon, 32(7), 1377-1382.

Hu, Q.H., Liu, H., Yang, R., Zhang, Y.X., Kibria, G., Sahi, S., Alatrash, N., MacDonnell, F.M. and Chen, W. 2017. Applying molecular and nanoparticle tracers to study wettability and

connectivity of Longmaxi Formation in Southern China. Journal of Nanoscience and Nanotechnology, 17(9),6284–6295.

Jarvie, D.M. 2012. Shale Resource Systems for Oil and Gas: Part 1—Shale-gas Resource Systems. Shale Reservoirs—Giant Resources for the 21st Century. AAPG Memoir 97, 89–119.

Javadpour, F., Fisher, D., and Unsworth, M. 2007. Nanoscale gas flow in shale gas sediments. Journal of Canadian Petroleum Technology, 46(10), 55-61

Kelemen, S., Fang, H. 2001. Maturity trends in Raman spectra from kerogen and coal. Energy & Fuels, 15, 653–658.

Loucks, R. G., Reed, R. M., Ruppel, S. C., & Hammes, U. 2010. Preliminary classification of matrix pores in mudrocks. Gulf Coast Association of Geological Societies Transactions, 60(2), 435–441.

Makhanov, K., Dehghanpour, H. and Kuru, E., 2013. Measuring liquid uptake of organic shales: A workflow to estimate water loss during shut-in periods. In SPE Unconventional Resources Conference Canada, Calgary, Alberta, Canada. SPE-167157-MS.

Marshall, A.O., Wehrbein, R.L., Lieberman, B.S. and Marshall, C.P. 2012. Raman spectroscopic investigations of burgess shale–type preservation: a new way forward Raman spectroscopy of bst deposits. Palaios, 27(5), 288-292

Ross, D.J. and Bustin, R.M. 2009. The importance of shale composition and pore structure upon gas storage potential of shale gas reservoirs. Marine and Petroleum Geology, 26(6), 916-927.

Schito, A., Corrado, S., Aldega, L., Grigo, D. 2016. Overcoming pitfalls of vitrinite reflectance measurements in the assessment of thermal maturity: the case history of the lower Congo basin. Marine and Petroleum Geology,74, 59–70.

Spötl, C., Houseknecht, D.W. and Jaques, R.C. 1998. Kerogen maturation and incipient graphitization of hydrocarbon source rocks in the Arkoma Basin, Oklahoma and Arkansas: a combined petrographic and Raman spectrometric study. Organic Geochemistry 28(9-10), 535-542.

Taylor, G.H., Teichmüller, M., Davis, A.C.F.K., Diessel, C.F.K., Littke, R. and Robert, P. 1998. Organic Petrology. Borntraeger, Berlin-Stuttgart, 704 p.

Tissot, B.P., 1984. Recent advances in petroleum geochemistry applied to hydrocarbon exploration. AAPG Bulletin, 68(5), pp.545-563.

Tuinstra, F. and Koenig, J.L., 1970. Raman spectrum of graphite. The Journal of Chemical Physics, 53(3), pp.1126-1130.

Wang, S., Javadpour, F. and Feng, Q. 2016. Confinement correction to mercury intrusion capillary pressure of shale nanopores. Scientific Reports, 6: 20160, doi: 10.1038/srep20160.

Wilkins, R.W., Boudou, R., Sherwood, N. and Xiao, X., 2014. Thermal maturity evaluation from inertinites by Raman spectroscopy: the 'RaMM'technique. International Journal of Coal Geology, 128, pp.143-152.

Yang, R., Hao, F., He, S., He, C., Guo, X., Yi, J., Hu, H., Zhang, S. and Hu, Q. 2017. Experimental investigations on the geometry and connectivity of pore space in organic-rich Wufeng and Longmaxi shales. Marine and Petroleum Geology, 84, 225–242.

Zhou, S., Liu, D., Karpyn, Z.T., Cai, Y. and Yao, Y., 2018. Effect of coalification jumps on petrophysical properties of various metamorphic coals from different coalfields in China. Journal of Natural Gas Science and Engineering, 60, pp.63-76.

Zhou, S., Yan, G., Xue, H., Guo, W. and Li, X. 2016. 2D and 3D nanopore characterization of gas shale in Longmaxi formation based on FIB-SEM. Marine and Petroleum Geology, 73, pp.174-180.

Chapter 2

Pore structure, wettability, and spontaneous imbibition of Woodford Shale, Permian Basin, West Texas

Md Golam Kibria[1], Qinhong Hu[1*], Hong Liu[2], Yuxiang Zhang[1], and Jianhong Kang[3]

[1]Department of Earth and Environmental Sciences, The University of Texas at Arlington, 500 Yates Street, Arlington, TX 76019, USA

[2]Petroleum and Natural Gas Technology Institute, Chongqing University of Science and Technology, Chongqing 401331, China.

[3]School of Safety Engineering, China University of Mining and Technology, Xuzhou 221116, China

Published at:

Marine and Petroleum Geology

[*] Corresponding author: maxhu@uta.edu

Abstract

Even after more than 30 years of exploration and production, low total recovery of shale gas (<30%) and tight oil (5%-10%) constrains sustainable shale hydrocarbon development in the United States. Since the Woodford Shale is one of the principal source rocks of the Permian Basin, West Texas, this study uses core samples of Woodford Shale from the Reliance Triple Crown (RTC) #1 well in Pecos County, Texas, to examine mineralogy, pore structure, wetting characteristics, imbibition behavior, and edge-accessible porosity with the following complementary tests: X-ray diffraction (XRD), mercury injection capillary pressure (MICP), contact angle measurement of various fluids, fluid imbibition into initially dry shale, and edge-accessible pore connectivity from vacuum saturation-high pressure impregnation with tracers-containing n-decane. The wettability and imbibition tests use both polar (hydrophilic, DI water) and nonpolar (hydrophobic, n-decane) fluids. Our results indicate that Woodford Shale samples (Upper, Middle, and Lower Members) have different geologic (mineralogy) and reservoir (e.g., total organic carbon, porosity, and permeability) characteristics. MICP analyses show that the median pore-throat diameters for the Woodford Shale are 3.7–5.4 nm, and almost 70–80% of pore-throats by volume are smaller than 100 nm, with high tortuosity for fluid flow and mass movement. Spontaneous fluid imbibition into Woodford Shale exhibits imbibition slopes (from the plots of log imbibition vs. log time) close to ¼ for DI water and ½ for n-decane, consistent with contact angle measurements that indicate a marginally water-wet, but very strong oil-wet, nature for these shales. Edge-accessible pore connectivity tests indicate that well-connected hydrophobic pore networks (primarily organic matter-hosted pores) have pore-throat sizes of approximately 5 nm and experience molecular entanglement with nm-sized tracers used in vacuum saturation tests. Our analyses suggest that the middle Woodford member will be the best

interval for stimulation and hydrocarbon production. The findings from these complementary experimental approaches suggest low connectivity of tortuous nanopore networks and mixed-wet characteristics, which could have implications for total hydrocarbon recovery in Woodford Shale.

1. Introduction

Shale hydrocarbon exploration and production from various basins in the United States have experienced significant growth due to scientific and technological improvements in hydraulic fracturing and horizontal drilling; this is changing the oil and gas industry worldwide (EIA, 2014). Contributing to 44% of the total gas production, in 2016, U.S. shale gas production was approximately 14 trillion cubic feet (Tcf), a sharp increase compared to the 1.6 tcf produced in 2007 (EIA, 2016). Similarly, since 2009, U.S. oil production saw the highest level of oil production in 2016, mostly from the growth in shale plays ("tight oil formations"), with close to 3.5 billion barrels per year (9.4 million barrels per day) (EIA, 2016).

The Woodford Shale is considered an important source of hydrocarbons within the Permian Basin (Galley, 1958; Comer, 1991; Cardott, 2012; Hackley et al., 2016). Based on its geographic location and depositional characteristics, this Shale has been discovered in three different basins: the Woodford (Arkoma Basin) and Cana-Woodford (Anadarko Basin) of Oklahoma, and the Barnett Woodford (Delaware Basin) of Texas. These three Woodford Shales are projected to contain technically recoverable shale gas resources of 22.21 tcf, 5.72 tcf, and 32.15 tcf, respectively (Gupta et al. 2013; EIA, 2014).

In the research area for this study, in Pecos County, Texas, the Barnett Woodford (Delaware Basin) is an organic-rich formation with 2-6 wt.% TOC (total organic carbon). This formation has solid bitumen, which is an organic assemblage, and ~1.35% R_o maturity indicates that the formation is within the condensate-wet gas window (Hackley et al., 2016). Similarly, the Woodford Shale of the Cana-Woodford (Anadarko Basin) and Woodford (Arkoma Basin) in Oklahoma has been well known as oil- and condensate-rich plays. The thermal maturity of the Woodford Shale in the Arkoma Basin is 0.55% R_o at depths of approximately 2300 ft (700 m) in

the western portion of the Basin, while the eastern part of the Basin is overmature (6.0% R_o) at depths up to 17000 ft (5200 m); the average thermal maturity is 1.67% R_o for the Arkoma Basin Woodford Shale (Cardott, 2012). For the Cana-Woodford (Anadarko Basin), the thermal maturity varies from 0.49% R_o at a depth of 3600 ft (1100 m) to 4.89% R_o at 22,500 ft (6800 m) (Cardott et al., 1990).

There are numerous publications with an attempt to understand the Woodford Shale as a source rock, yet most of these studies focus on the geochemical signatures of stratigraphic sequences (Ellison, 1950; Comer, 1991; Mnich, 2009; Rowe et al., 2012; Harris et al 2013; Hemmesch et al., 2014), or the mechanical properties and fracturing potential (Aoudia, 2009; Harris et al., 2011). This research investigates pore structure and wettability and their effects on fluid flow, which have rarely been studied for the Permian Basin's Woodford Shale; the work of Mnich (2009) and Aoudia, (2009) only reported the measurements of porosity and permeability. This study focuses on an area in the southwestern part of the Permian Basin (Figure 1), where the Woodford Shale is reported to produce dry gas, condensate, and sometimes oil, from an averaged 46 m-thick formation (Comer, 1991). In this work, we quantify pore structure with mercury injection capillary pressure (MICP), evaluate wettability characteristics from the contact angle measurement, and assess pore connectivity by spontaneous imbibition; both contact angle and imbibition tests involve both polar and non-polar (e.g., deionized water and n-decane) fluids to examine hydrophilic and hydrophobic surfaces and pore networks. Using tracers in n-decane, we also employ a vacuum saturation & high-pressure impregnation approach to identifying the distribution of edge-accessible connected pore spaces. This work will bridge the knowledge gap of pore size distribution, pore connectivity, wettability, and stimulation interval implicated in the

hydrocarbon extraction for the Woodford Shale; the approaches and findings are also beneficial for other shale reservoirs.

2. Geological Background

Occupying western Texas and southeastern New Mexico, the Permian Basin has become the common location name used for a significant oil and gas province (Dutton et al., 2005). The Woodford Shale is one of the major hydrocarbon source rocks in the western Texas Permian Basin area. The Tobosa Basin is the basin below the Permian Basin within West Texas where the Woodford Shale was deposited, while the Delaware and Midland Basins are two subdivisions of the younger Permian Basin (Galley, 1958; Comer, 1991). Formed in Late Devonian time, the Tobosa Basin is bounded by the siliciclastic Pedernal Massif in the northern area, the Concho Arch (a shallow water platform) borders the eastern side, and the Diablo platform (another shallow platform) borders the western side (Figure 1). The highest burial depth of the Woodford Shale in the Delaware and Val Verde Basins is approximately 6400 m, while the burial depth in the Midland Basin and Central Basin Platform is lower (Comer, 1991).

The thickness of the Woodford Shale in the basin center is 180 m and decreases to less than 30 m around basin margins (Comer, 1991). Based on the well log patterns, the Woodford Shale can be divided into three stratigraphic members: Upper, Middle, and Lower Woodford (Comer, 1991; Harris et al., 2011; Hemmesch et al., 2014). The Lower and Upper Woodford Shale Members show high gamma-ray amplitude differences over a scale of 3–10 m. With a range of 400-800 API units, the Middle Woodford Shale also shows steadily higher gamma-ray values (Comer, 1991; Aoudia, 2009; Harris et al., 2011; Hemmesch et al., 2014).

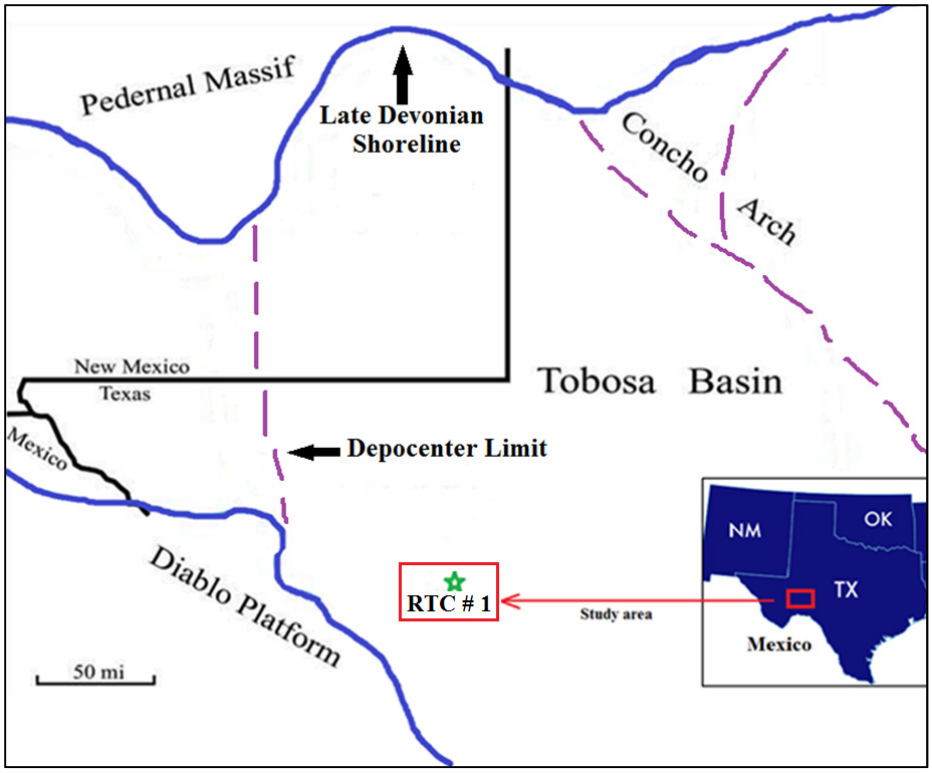

Figure 1. The geographic location of the Reliance Triple Crown #1 well in the western Permian Basin, Texas, as well as the stratigraphic column (redrawn from Comer, 1991).

3. Materials and methods

3.1 Core samples and preparation

This work uses core samples collected from the Reliance Triple Crown (RTC) #1 well (103.46°W, 30.79°N; API 42-371-37790), completed by Pioneer Natural Resources in 2007, in Pecos County, Texas (Figure 1). The total thickness of the retrieved core is approximately 100 m, with the Woodford Shale alone covering 85% of the total section. In this core, the Upper Woodford Member is irregularly thin, and the top of the Woodford Shale Mississippian Lime has unconformable intervals (Harris et al., 2011). In our study, we use the following five core samples at different depths below ground surface (Figure 2; Table 1): 3912-U (for 12835 ft or 3912.11 m), 3931-U (3930.70 m), 3942-M (3941.67 m), 3955-M (3955.39 m), and 3967-L (3967.28 m). Here, letters U, M, and L denote Upper, Middle, and Lower Woodford Members.

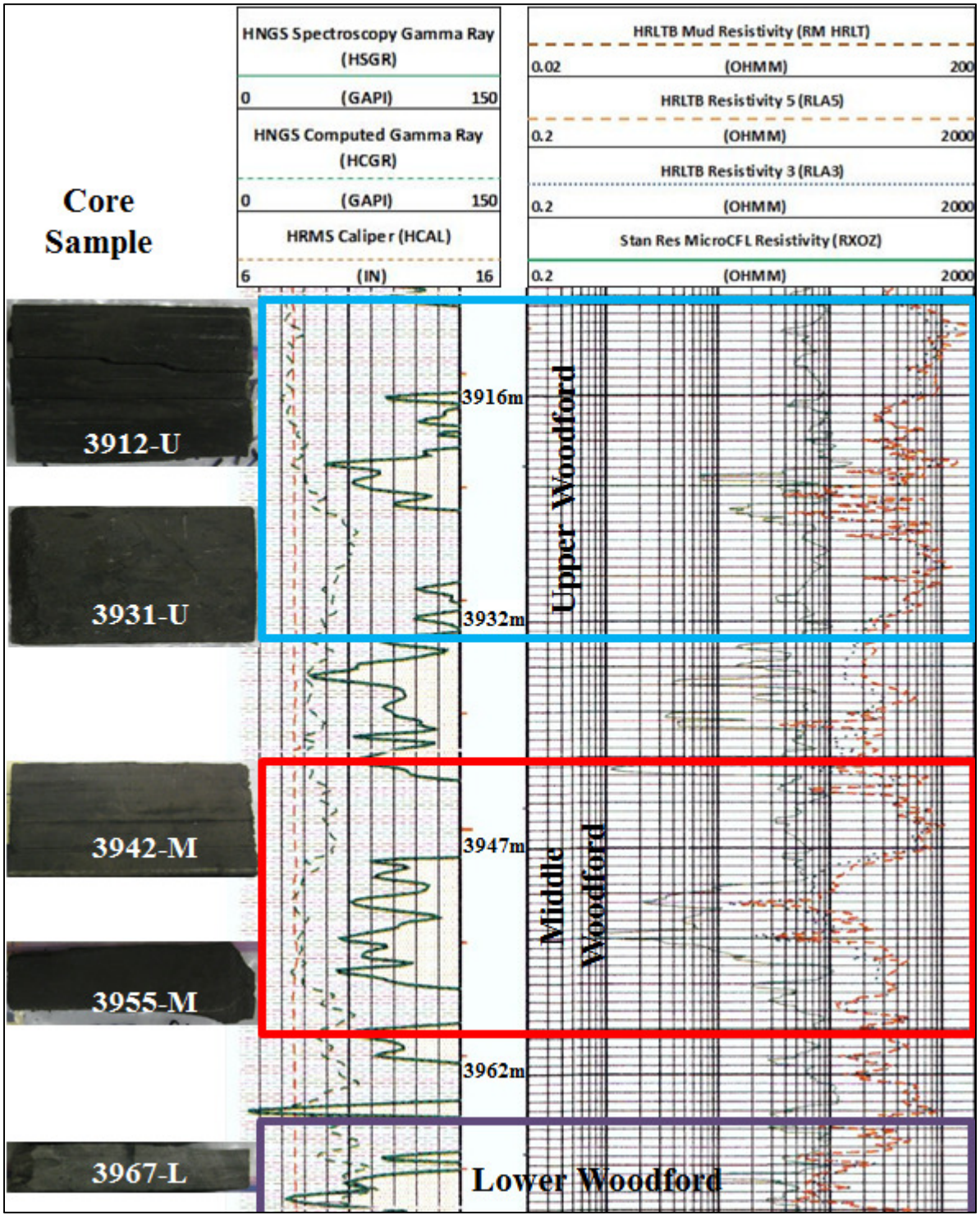

Figure 2: Well log of Woodford intervals and sample photos.

For MICP and spontaneous imbibition (SI) tests, the core slab was cut into cubes with a linear dimension for each side of 10-11 mm, using a 6" Lapidary trim saw (Kingsley North Inc., Norway, MI) and minimal use of cooling water. To investigate the contact angle, the cubes were further cut into thin slabs (10 mm × 10 mm × 3 mm) using a circular saw (IsoMet Low-Speed Saw, Buehler, Lake Bluff, IL). After that, the slabbed samples were polished on a 240-grit sandpaper. To investigate edge-accessible connected porosity, 3931-U sample was dried in an oven at 60±2°C for at least two days, then subject to vacuum saturation, followed by high-pressure impregnation, a process with n-decane containing tracers (detail is provided in the Section vacuum saturation & high-pressure impregnation). The powdered shale sample fraction (<75 μm) was used to determine mineralogical composition with X-ray diffraction (XRD) (Maxima XRD-7000, Shimadzu Corporation, Kyoto, Japan), and TOC using Shimadzu TOC-VWS Wet Chemical Total Organic Carbon Analyzer.

Table 1. Mineralogy and TOC of the Woodford Shale samples.

Sample ID	Depth (ft/m)	Zone	TOC(%)	Mineralogy (weight %)					
				Quartz	Clay	Pyrite	Feldspar	Magnesite	Dolomite
3912-U	12835/3912.11	Upper	6.5	76.5	10.6	3.4	5.8	3.7	
3931-U	12896/3930.7		3.1	91.8	5.5	1.5		1.2	
3942-M	12932/3941.67	Middle	5.7	85.7	4.4	3.6	6.2		
3955-M	12977/3955.39		7.7	69.0	4.4	7.5	11.5	3.4	3.2
3967-L	13016/3967.28	Lower	1.1	47.2	32.0	20.8			

3.2. Mercury injection capillary pressure (MICP) analysis

The MICP method is one of the most efficient and cost-effective ways to characterize pore structure for porous solids such as shales (Gao and Hu, 2013). The porosity, particle density, bulk density, and pore-throat size distribution of a porous medium can be directly measured by

MICP tests (Webb, 2001; Gao and Hu, 2013; Zhang et al., 2016). In addition, permeability (Katz and Thompson, 1986; 1987; Gao and Hu, 2013) and tortuosity (Hager, 1998; Webb, 2001; Hu et al., 2015) can be indirectly derived from MICP results.

Utilizing a mercury intrusion porosimeter (AutoPore IV 9510, Micromeritics Instrument Corporation, Norcross, GA), liquid mercury was incrementally injected with an increasing hydrostatic pressure to occupy the pore spaces of increasingly smaller pore-throat sizes in shale. Considering the high surface energy and non-wetting characteristics of mercury and assuming that the pores are cylindrical, Washburn (1921) determined pore throat diameters from equivalent pressures.

Before the MICP tests, a cube-sized shale sample was placed in an oven at 60°C for at least two days to remove moisture. Then, the samples were kept in a desiccator with a relative humidity of less than 10% at room temperature (23°C) for cooling. At the beginning of MICP test, the connected pore spaces in a sample are evacuated until 50 µm Hg pressure (at 6.7 Pa or 99.993% vacuum). Then, the sample is subjected to low-pressure conditions, followed by a high-pressure test up to 413 MPa or 60,000 psi, which corresponds to a pore throat diameter of 2.8 nm using the corrected Washburn equation to consider variable contact angle and surface tension in nm-sized pore spaces (Wang et al., 2016). A penetrometer (narrow-bore sample holder), used for samples with less than 5% porosity, recorded the largest pore throat diameter at 50 µm under low-pressure MICP analysis with 5 psi filling pressure. An equilibration time of 10 sec was selected as pressures proceeded from one level to another, and a mercury volume change was set to be <0.1 µL for each step, initial evacuation and low-pressure mercury injection took approximately 30 minutes. For the high-pressure test, the equilibration time was 30 sec with a

total analysis time of approximately 3 hrs at about 80 pressure points between 30 to 60000 psi for both intrusion and extrusion tests.

To estimate permeability, we used Equation 1, proposed by Katz and Thompson (1986; 1987) and detailed in Gao and Hu (2013).

$$k = \frac{1}{89}(L_{max})^2(^{L_{max}}/_{L_c})\varphi S(L_{max}) \quad (1)$$

Using the MICP data, we derived another important topological feature, effective tortuosity, τ, using Equation 2 (Hager, 1998; Webb, 2001):

$$\tau = \sqrt{\frac{\rho}{24k(1+\rho V_{tot})}\int_{\eta=r_{c,min}}^{\eta=r_{c,max}} \eta^2 f v(\eta)\, d\eta} \quad (2)$$

3.3. Wettability and contact angle measurement

Studying the wettability of shale surfaces is essential to understanding the gas flow and the flow-back behavior of fracking fluids in shale formations (Fernø et al., 2011). The reservoir can be permanently damaged due to incorrect assessment of wettability behavior (Morrow, 1990; Sulucarnain et al., 2012; Singh, 2016). A growing number of researchers have started to experimentally investigate the wettability characteristics of various shales (Borysenko et al., 2009; Odusina et al., 2011; Makhanov et al., 2013; Gao and Hu, 2016). Wettability can be straightforwardly assessed by measuring the contact angle of different fluids on a solid surface.

A contact angle meter and interface tensiometer (Model SL200K, USA Kino Industry Co., Norcross, GA) were used to measure the contact angle of polished Woodford Shale samples at 23°C; the contact angle measurements require the solid surface to be smooth because surface roughness has a significant effect on the wetting angle (Singh, 2016).. Contact angle values were obtained for different polar and nonpolar fluids, including deionized water (DI water), API brine (8% NaCl and 2% $CaCl_2$ by weight; Crowe, 1969) (a representative formation water), 20% IPA

(isopropyl alcohol, C_3H_7OH) in DI water, and n-decane (a representative oil-phase fluid) (Yang et al., 2017). A droplet of each fluid at 2 μL was placed onto the shale sample surface (Figure 3), and an image for the air-liquid-solid interface was captured to calculate contact angle using CAST™2.0 software.

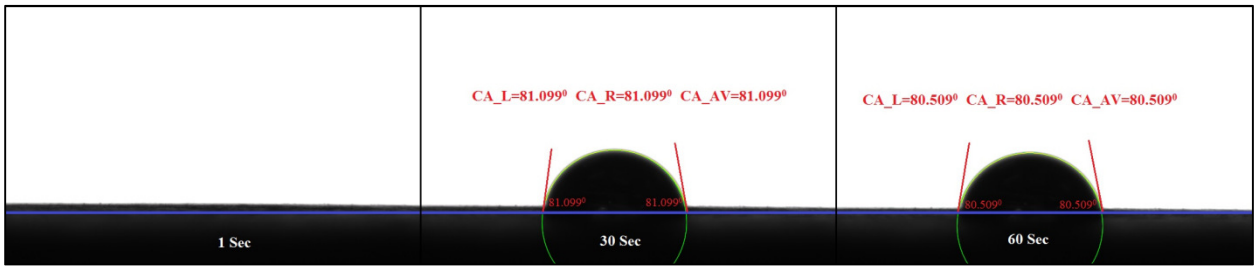

Figure 3: Fluid droplet contact angle tests for API brine on Woodford shale 3955-M sample (CA: contact angle; L: left; R: right; AV: average).

3.4. Spontaneous imbibition (SI)

Spontaneous imbibition (SI) is a capillarity-controlled process that shows the displacement of a non-wetting fluid by a wetting fluid under the influence of capillary pressure. Considering the importance of imbibition, a significant number of researchers had been studying imbibition in various rocks (e.g., Hu et al., 2001; Takahashi and Kovscek, 2010; Ghanbari and Dehghanpour, 2015). Furthermore, the imbibition process helps assess pore connectivity for a given sample using the slope of log-imbibed fluid mass versus log-time (Hu et al., 2012), aided by the pore network model approach (Ewing and Horton, 2002).

Four side-walls, except for the bottom and top faces, of each cubic sample were covered with a thin coating of quick-cure epoxy to produce co-current imbibition. The dimensions of the samples tested and the other relevant properties are listed in Table 3. All samples were dried in a similar fashion to the MICP tests, before the imbibition test was run. The apparatus for spontaneous imbibition is illustrated in Figure 4, using a semi-microbalance at 0.01 mg

resolution (Model AUW220D, Shimadzu, Kyoto, Japan). Hu et al. (2001) detailed the steps of conducting the imbibition tests and analyzing resultant data. In this research, DI water and n-decane were used as the imbibing liquids to displace air from pore spaces. Changes in sample weight over time were automatically recorded, and the fluid mass imbibed by the samples was calculated after adjusting for the buoyancy change and evaporation losses (Hu et al., 2001). The imbibition test was run for approximately 3-4 hours for n-decane and 8-9 hours for DI water before the sample was detached from the fluid contact.

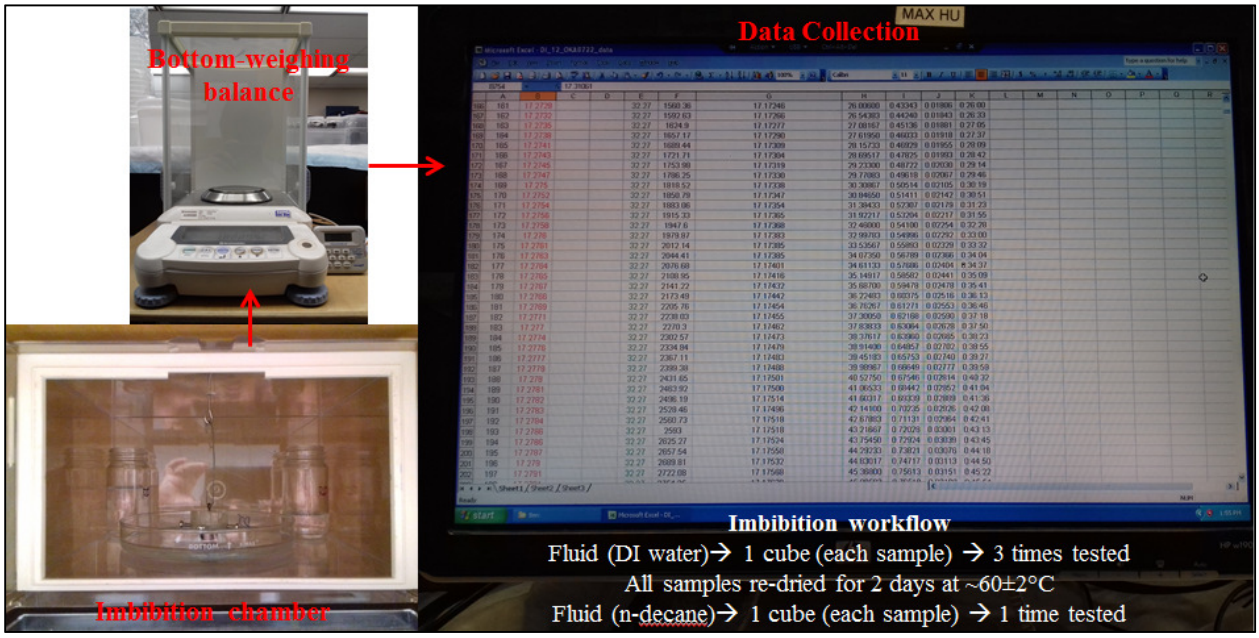

Figure 4: Imbibition apparatus and workflow.

When imbibition occurs vertically with negligible gravitational force, the SI process in a liquid–air system is expressed by Equation 3 (Handy, 1960):

$$Q_w^2 = \left(\frac{2P_c k_w \varphi A^2 S_w}{\mu_w}\right) t \tag{3}$$

With the assumption of well-connected pore space for a porous medium, Equation 3shows a square-root-of-time relationship. A plot of cumulative imbibition mass/height vs. imbibition time

on log-log coordinates shows Fickian diffusion-type behavior (Fick 1855), where the percentage of fluid absorption increases steadily with $t^{1/2}$ in the initial stage and then tends to level off following the saturation point. Without an assumption of pore connectivity, Hu et al. (2012) reported three types of imbibition slopes for different rocks in such log-log plots, with values at 0.5, 0.26, and 0.26 transitioning to 0.5. Theoretical studies with percolation theory suggest that higher slope values are a representation of good connectivity in a porous media, while lower slope values are a sign of low pore connectivity (Stauffer and Aharony, 1994; Hu et al., 2012; Hunt et al., 2014).

3.5. Vacuum saturation & high-pressure impregnation

This test quantifies the edge-accessible connected pore distribution, where only pores connected to the sample edge are accessible to an invasion of fluid or gas; such a distribution is related to pore connectivity (Hu et al., 2015). We used n-decane fluid for analyzing edge-accessible pores, considering its wetting behavior on Woodford Shale. The n-decane fluid includes two organic-phase molecular tracers with >99% pure tracer element-containing reagents: 1-iododecane {$CH_3(CH_2)_9I$, with a molecular weight of 268.18 g/mol, termed organic-I in this paper} and trichlorooxobis (triphenylphosphine) rhenium(V) {$[(C_6H_5)_3P]_2ReOCl_3$, with a molecular weight of 833.14 g/mol, termed organic-Re}. Hu et al. (2017) reported that the molecular dimensions of organic-Re are 1.27 nm length (L)×0.92 nm width (W)×0.78 nm height (H), while organic-I has dimensions of 1.39 nm (L)×0.29 nm (W)×0.18 nm (H).

The vacuum saturation setup consists of a sample chamber connected to a vacuum pump (SD-90, Varian Inc., Palo Alto, CA), a compressed gas (CO_2) cylinder with 0-60 psi single-gauge CO_2 regulator (Chudnow Manufacturing, Oceanside, NY), and a reservoir of saturating fluid. The goal is to evacuate the sample chamber and thus the pores connected to the edge of the sample.

This is achieved by producing a vacuum to 0.05 Torr (1 Torr=1 mm Hg=133.3 Pa), equivalent to a 99.993% vacuum, as indicated from 0.01-20 Torr Pressure/Vacuum Meter for Pirani-Type Sensor (Cole-Parmer, Vernon Hills, IL) after 100 min, and staying at this pressure for nearly 2 hrs. Flushing with CO_2 was conducted for three cycles at approximately 1 hr for each cycle, with vacuum pulling for 1-2 hrs between cycles; this is followed by further evacuation of the sample at 0.04 Torr for 40 hrs. Then, while the sample was still under a vacuum, a saturating fluid (n-decane with tracers) was introduced into the chamber until the sample was immersed so that the fluid would occupy the evacuated pore spaces connected to the sample edge. Subsequent to immersion, pressurized CO_2 at 50 psi was applied to the chamber for 12 hrs, further driving the tracer-containing fluid into the pore spaces.

Following vacuum saturation, the saturated sample is further subjected to pressure of 50000-60000 psi for one hour, by placing saturated sample inside a wrapped glove finger in the high-pressure chamber of the MICP instrument. Instead of pressurizing mercury into the sample during a MICP analysis, the tracer-containing n-decane is impregnated into the connected pore spaces under high hydrostatic pressure. The saturated samples were then weighed, immediately frozen in liquid nitrogen, freeze-dried at -50.5^0C and 0.054 Torr, and stored at low relative humidity before being mapped with Laser Ablation-Inductively Coupled Plasma-Mass Spectrometry (LA-ICP-MS) (Hu et al., 2015; Hu et al., 2017).

We used a 213-nm laser for the laser ablation system (UP-213, New Wave; Freemont, CA) to produce sub-micron depth holes in the shale sample. The laser ablates the shale into vaporized elements, which were analyzed with ICP-MS (PerkinElmer/SCIEX ELAN DRC II; Sheldon, CT). First, the top and bottom of the sample (reservoir) face is identified based on the tracers presence using a laser ablation spot grid. After that, the sample is cut, under dry conditions, in

the middle from the top face crosswise relative to the imbibition direction. Then, LA-ICP-MS is performed, with a grid of spot analyses on the sawed inner face. The tracer-containing fluid occupies the evacuated connected pore spaces, so the tracer concentration profile is a proxy for the distribution of edge-accessible porosity.

4. Results and Discussion

4.1. Mineralogy and TOC

Values for total organic carbon (TOC) and mineralogy in wt% percentage are shown in Table 1, which indicate differences among core samples at different depths (Table 1). Except for sample 3012-U, quartz content in this core decreases with depths, at 91.8% for 3930.7 m (3931-U) and 47.2% for 3967.28 m (3967-L). Conversely, from a depth of 3930 m downward, pyrite content steadily increases from 1.5% in 3931-U to 20.8% for 3967-L. Due to the higher pyrite content in 3967-L, the sample has higher bulk (2.77 g/cm^3) and apparent (2.79 g/cm^3) densities as identified by MICP (Table 2). Clay content shows high values only for the top and bottom intervals. The top interval in 3912-U has a clay content of 10.6%, compared to 32% for the bottom interval in 3967-L. The clay percentage for the three samples between the top and the bottom range is within 4.4 to 5.5% (Table 1).

Varying from 1.1 to 7.7%, different depths of the RTC core have different TOC content (Table 1). TOC values for the Upper, Middle and Lower Woodford Members are 3.1 to 6.5%, 5.7 to 7.7%, and 1.1%, respectively. Woodford Shale from 3967 m depth (3967-L) shows 1.1% TOC, a small percentage of TOC in a relatively mature interval as a result of chemical alteration from kerogen to hydrocarbons and the expulsion of oil (Harris et al., 2011). The Lower and Middle Woodford Members show purely marine organic matter accumulation, while the Upper

Woodford Member contains more terrestrial organic matter (Mnich, 2009; Harris et al., 2011; Hackley et al., 2016). The vitrinite reflectance for the 3931-U sample is ~ 1.17 R_o (Harris et al., 2011), indicating that the Woodford Shale at the RTC well is in the wet gas window.

4.2. Pore structure characteristics from MICP tests

In this work, a single 1 cm-sized cube of smooth surface is used to perform the MICP analyses to avoid the conformance effect. The MICP results show a significant volume of nm-sized pores in the Woodford Shale. The median (at 50% by pore volume) pore-throat diameter is 3.7 to 5.4 nm, and more than 70–80% of pores by volume are less than 100 nm in pore-throat diameter (Table 2; Figure 5). Fluids with molecular sizes similar to pore-throat diameters can cause significant steric interference (Hu and Wang, 2003). Nelson (2009) showed that most petroleum species of concern in oil/gas exploration have a molecular diameter at 0.5 to 10 nm, whereas the molecular size of mercury is 0.31 nm. Pores less than 3 nm do not play a critical role in petroleum movement because of the Knudsen effect (Javadpour et al., 2007). Therefore, petroleum movement is expected to occur mostly within a pore network with 5 to 100 nm pore-throat sizes, based on a factor of 10 for pore to molecular size ratio (Hu and Wang, 2003).

Table 2. MICP analysis-derived pore structure properties for the Woodford Shale samples.

Sample ID	Bulk density (g/cm^3)	Apparent (skeletal) density (g/cm^3)	Total pore area (m^2/g)	Porosity (%)	Median pore-throat diameter (Area) (nm)	Permeability (nD)	"Tortuosity" (D_0/D_e)	Le/L [square root of (tortuosity * total porosity)]
3912-U	2.30	2.40	8.88	4.05	3.70	1.98	2193	9.43
3931-U	2.46	2.48	2.09	0.80	3.90	0.50	4085	5.70
3942-M	2.40	2.43	3.58	1.29	3.70	0.71	7267	9.70
3955-M	2.38	2.41	2.67	1.25	4.20	1.45	3142	6.26
3967-L	2.77	2.79	0.98	0.85	5.40	1.38	2853	4.94

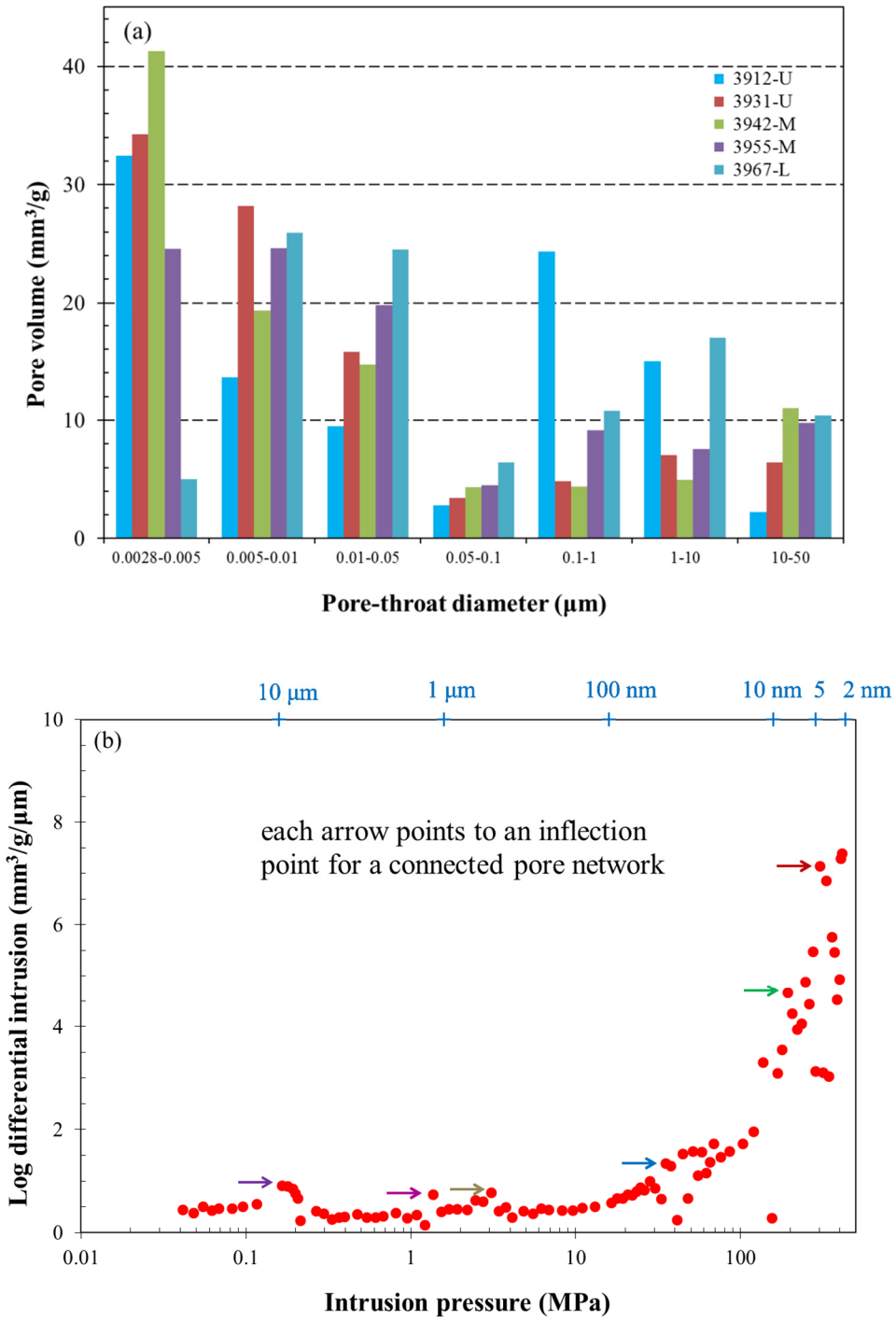

Figure 5. MICP results for (a) Pore volume distribution in diverse pore-throat regions for the Woodford Shale at five different depths; and (b) example 3955-M with multiple indications of connected pore networks from incrementally increasing intrusion pressures

While the SEM approach is ideal for the identification of pore types and shapes by image analyses, MICP analysis provides a cost-effective way to determine pore volume and pore-throat size. In this study, only 20-30% of the pore spaces are in the 100 nm-50 μm range of pore-throat size for the five Woodford Shale samples, though these pore-throat sizes play an important role as the primary conduits for hydrocarbon transport and the linkage of smaller nanopore regions. Using the equation of Katz and Thompson (1986) to calculate permeability, the permeability of the five Woodford samples is in the range of 0.51 to 1.98 nD (Table 2). This result is lower compared to the permeability values of 20-60 nD for the RTC core at 3974.90 m depth measured at a confining pressure of 5000 psi by Aoudia (2009). The permeability result by Aoudia (2009) is higher because of different methods, sample depth (3974.9 m of Lower Member), and sample size. In addition, the porosity of 146 RTC core samples, over depths of 3886 m to 3992 m, measured by helium pycnometry, is reported to be 0.03% to 14.5%, with an average of 4% (Aoudia, 2009). The pycnometry result is slightly different from our MICP-porosities of 0.8 to 4.05% with an average of 1.65% (Table 2), which is probably related to different sample sizes and methodologies. In the four Woodford core samples, the MICP porosities of 1-cm cubic samples are within 0.85 to 1.29%, and the permeability is 0.5 to 1.45 nD (Figure 6a). Only sample 3912-U has slightly higher values of porosity and permeability. A cross plot of median pore throat vs. permeability indicates that permeability does not depend on median pore-throat diameter for nanoporous shale samples (Figure 6b). Four samples have median-pore throat diameters within 3.7 to 4.2 nm, but permeability varies within the 0.5 to 2 nD range.

Effective tortuosity, τ, can be estimated by applying Hager's (1998) method to the MICP data, with values in the range of 2000–7000 (Table 2). Tortuosity describes the extent of intricate passageways for fluid migration within a porous medium (Epstein 1989; Hu and Wang, 2003).

Tight shale formations show comparably large values of tortuosity, which suggest that fluid within the rock will take a convoluted pathway to migrate from one location to another. These large tortuosity results imply that nanopores are sparsely connected with each other within the tight shale to take much more time to establish a connection to migrate hydrocarbon for an appreciable distance (Maytka et al., 2008; Hu et al., 2015).

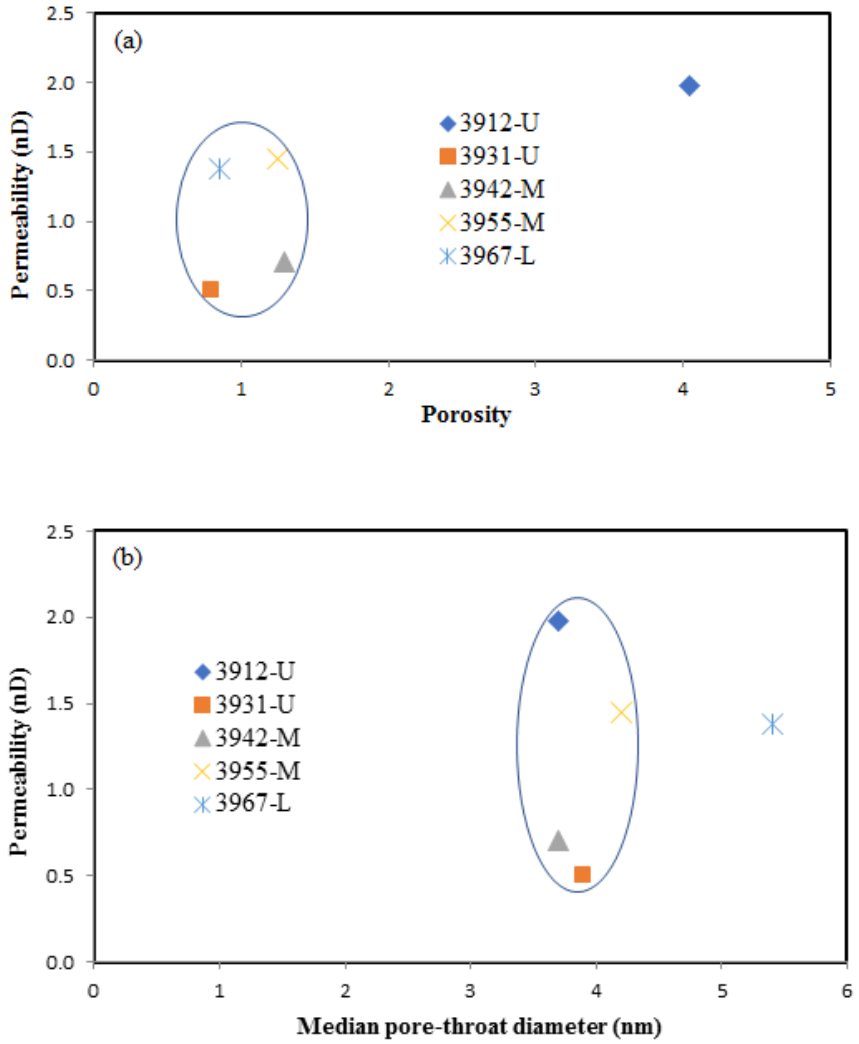

Figure 6: Relationships between MICP-derived (a) porosity vs. permeability and (b) median pore-throat vs. permeability.

4.3. Wettability and contact angle of Woodford Shale

The wettability of reservoir rocks can be classified as water wet, oil wet, and intermediate wet based on the contact angle formed between the fluid and rock surface (Craig, 1971). The water-wetting fluid has an attraction towards the water-wet rock surface. Oil-wet surfaces have an affinity for oil, rather than water, when spreading onto the surface. Intermediately-wet surfaces have affinities that do not lead to attraction toward water or oil. Within the mixed-wet reservoir rock, water- and oil-wet surfaces may coexist (Salathiel, 1973; Takahashi and Kovscek, 2010).

Table 3 shows the contact angle measurements obtained for the Woodford Shale, using four different fluids, DI water, API brine, 20% (v/v) IPA in DI water, and n-decane. Over the depths of 3912.11 m (3912-U) to 3955.39 m (3955-M), the contact angles of DI water are in the range of 43.6° to 54.6° at 30 sec after the droplet comes in contact with the sample surface. The Lower Woodford Member 3967-L shows a smaller contact angle of 16.7° for DI water (Table 3 and Figure 7). As shown in Table 3, the Woodford Shale samples are intermediately water-wet, except for the Lower Woodford Shale sample (3967-L), which is strongly water-wet; this sample also has the highest clay (32%) content (Table 1), with clay minerals mostly being water-wet. Furthermore, the four samples from the Upper and Middle Woodford members show higher contact angles (70.9° to 81.0°) for API brine, which indicates non-wetness toward API brine with high salinity. On the other hand, the Lower Woodford Member (3967-L) is wetting to API brine with a contact angle of 15.3°.

As an oil-wetting fluid, n-decane very quickly wets the sample surface to shows a much lower contact angle (angle 5.41° to 9.42° at milli-seconds to <3°, which is the detection limit) throughout the samples, regardless of the different mineralogy for the Woodford Shale members. Other publications report similar experimental results on shale from various formations around

the world, suggesting that kerogen-rich shales tend to have a higher affinity for oil than for water (Singh, 2016).

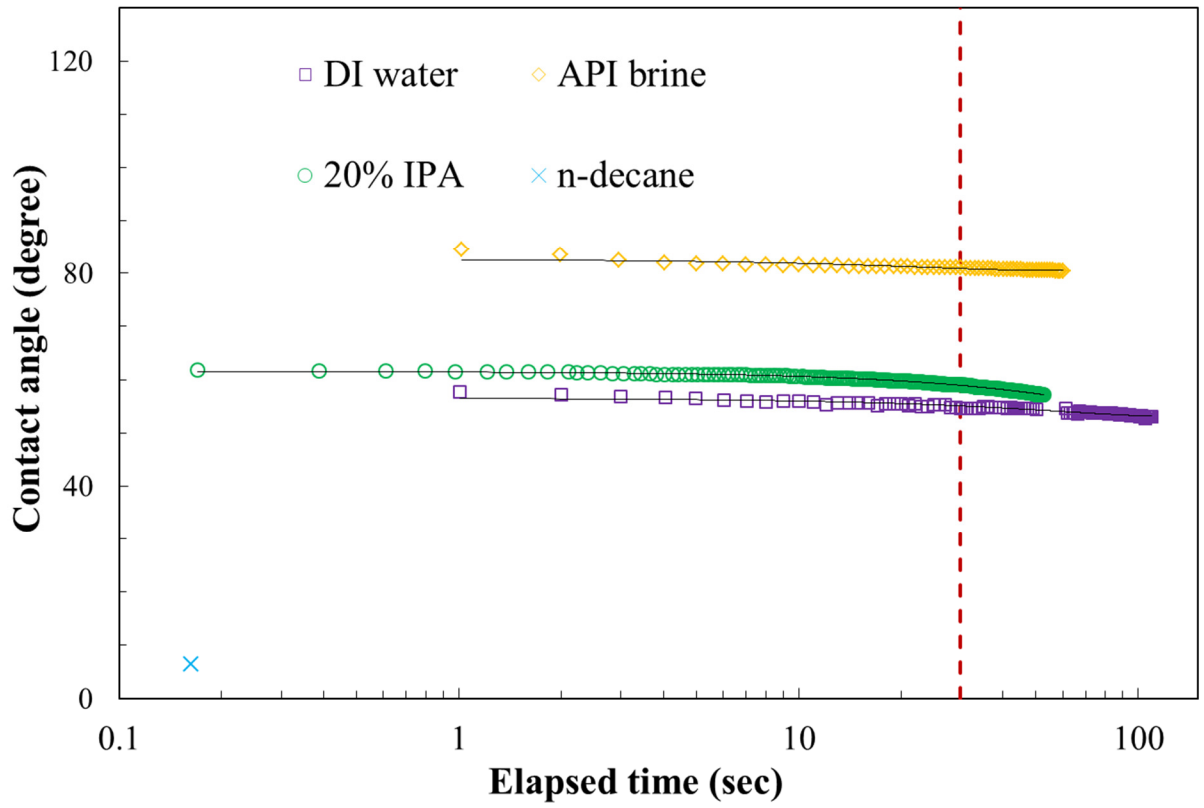

Figure 7. Contact angle measurements for 3955-M; a vertical line is drawn at 30 sec after the droplet tests.

As a zwitter fluid, IPA (100%) can access both water- and oil-wetting pores and was used to prepare a mixture with DI water to observe the intermediate wettability behavior between n-decane and DI water. However, at the low percentage of 20%, the contact angle for IPA used in this work is quite similar to DI water (Table 3 and Figure 7).

4.4. Spontaneous imbibition

The spontaneous imbibition process produces ½ slope for late-time imbibition [d log (liquid mass uptake)/d log (duration)] for well-connected porous media in contact with wetting fluid. Figure 8a serves as an exemplary DI water imbibition figure for sample 3942-M, steadily exhibiting a ¼ slope to indicate that this rock has poorly-connected pore spaces for water, as compared to 1/2 slope for Berea sandstone (benchmark reservoir rock in the research community of oil and gas industry) (Hu et al., 2012). Table 3 presents the spontaneous imbibition results for Woodford Shale at different depths. In general, low-connectivity porous media show a characteristic imbibition slope of ¼ (Hu et al., 2015; Gao and Hu, 2016). The Woodford Shale exhibits an imbibition slope close to ¼ for DI water, which is consistent with the intermediately water-wetting characteristics based on contact angle measurements.

Table 3. Contact angle (in degrees) measurements (at 30 secs after droplet contact) and slope values from spontaneous imbibition experiments for the Woodford Shale samples.

Sample ID	Fluid	Contact Angle (in degrees)	Imbibition slope
3912-U	DI water	49.7	0.207±0.058 (n=3)
	n-decane	<5.77	0.591
	API brine	78.9	
	20% IPA	42.7	
3931-U	DI water	48.7	0.256 ±0.028 (n=3)
	n-decane	<5.41	0.352
	API brine	76.5	
	20% IPA	49.1	
3942-M	DI water	43.6	0.273±0.048(n=3)
	n-decane	<9.42	
	API brine	70.9	
	20% IPA	61.2	
3955-M	DI water	54.7	0.33±0.035 (n=3)
	n-decane	<6.47	0.591
	API brine	81	
	20% IPA	59	
3967-L	DI water	16.7	0.264±0.032 (n=3)
	n-decane	<6.47	0.566
	API brine	15.3	
	20% IPA	16.8	

In Figure 8, the imbibition data for the first 20 sec show a steep and noisy initial phase; this is because of the settling of the sample from initial contact with the DI water. For some samples, during a subsequent brief time (within 1 minute), a stable slope of 0.50±0.012 (the ½ slope for classical Fickian behavior) is observed. Some researchers report that fluid migration up to the shale surface region of the side walls, and the associated good connectivity to exhibit Fickian behavior (Hu et al., 2015; Gao and Hu, 2016, Singh, 2016). Hu et al. (2012) showed that when a porous surface area increasingly gains moisture in a Fickian manner, it continuously shows ½ slope for spontaneous imbibition. After approximately 1 min, the entire bottom/external surface is wetted, and the imbibition slope switches to a value of ¼, which is maintained for the experimental period of 8-9 hrs.

Table 3 shows the imbibition characteristics of n-decane fluid for the Woodford Shale, and Figure 8b represents a typical plot of n-decane imbibition. Berea sandstone steadily exhibits a ½ slope to indicate that this rock has well-connected pore spaces for DI water imbibition (Hu et al., 2012). Four samples out of the five exhibit ½ slopes, which indicates that hydrophobic pore spaces are well connected for the Woodford Shale, consistent with their nearly 5° contact angles and suggesting an oil-wetting rock. Sample 3931-U shows a lower imbibition slope of 0.352, though the sample has the same contact angle as the other shales. Compared with other depths, this sample has a lower clay content (4.4%) and a higher quartz percentage (10.7%) (Table 1). Samples from 3967-L have higher clay (32%) and pyrite (20.8%) percentages and a low quartz percentage (47.2%), but we do not observe a similar change in imbibition characteristics for those samples. The imbibition curve for n-decane displays a relatively large amount of n-decane uptake during the first 10-15 min, indicating that the sample is more oil-wet than DI water-wet for all samples (an example is shown in Figure 8b for 3955-M).

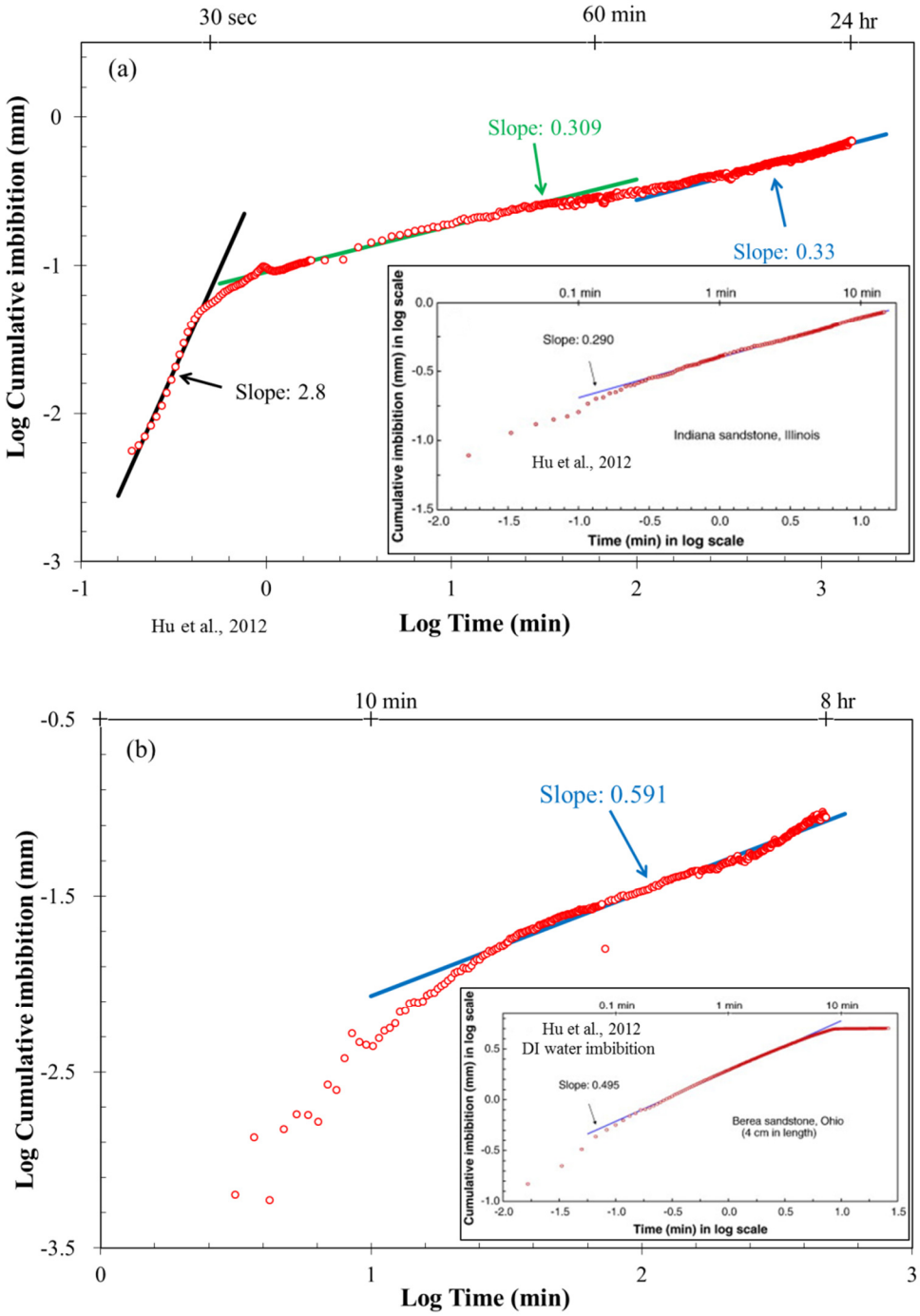

Figure 8. Log DI imbibition (mm) vs. Log time (min) for sample 3955-M: (a) DI water; (b) n-decane.

4.5. Edge-accessible pore connectivity from vacuum saturation & high-pressure impregnation

To further study the interrelationship of wettability and connectivity, the edge assessable porosity distribution was interrogated by vacuum saturation. As shown in Figure 9, the scatter plot on the top shows the normalized concentration (ratio of the average concentration from "bottom+top faces", with a total of 98 sampling spots, as the tracers come into the samples from all six faces of a cube) of tracers over the distance from the sample edge (the sample height is 8500 μm) to the interior surface. Figures at the bottom are mapped tracer distributions. Each vertical tracer panel consists of three (top, interior, and bottom) sample faces, with each dashed line on the top and bottom faces being 1000 μm apart. The LA-ICP-MS detection limits for I and Re tracer elements are 0.5 and 0.1 mg/kg, respectively; the color change directly indicates the extent of tracer penetration (i.e., edge-accessible pore connectivity). The white zones characterize the areas with tracer concentration below the detection limit.

The tracer penetrates most pore spaces of the shale matrix within the zone (Zone A) of 0.5-1 mm from the sample edge, as seen in concentrations similar to those at "bottom+top faces." Deeper into the shale matrix from this well-connected Zone A, detected organic-I concentrations are lower and more sporadic, indicative of sparse connectivity in Zone B.

Furthermore, the larger height/width of organic-Re with less conformational flexibility leads to molecular entanglement in pore networks with pore-throat sizes of only approximately 5 nm, as shown by its much lower presence even in Zone A. Such test design and the utility of wettability tracers of different molecular sizes help tease out the intertwined relationship of pore sizes, connectivity, and associated wettability of shale.

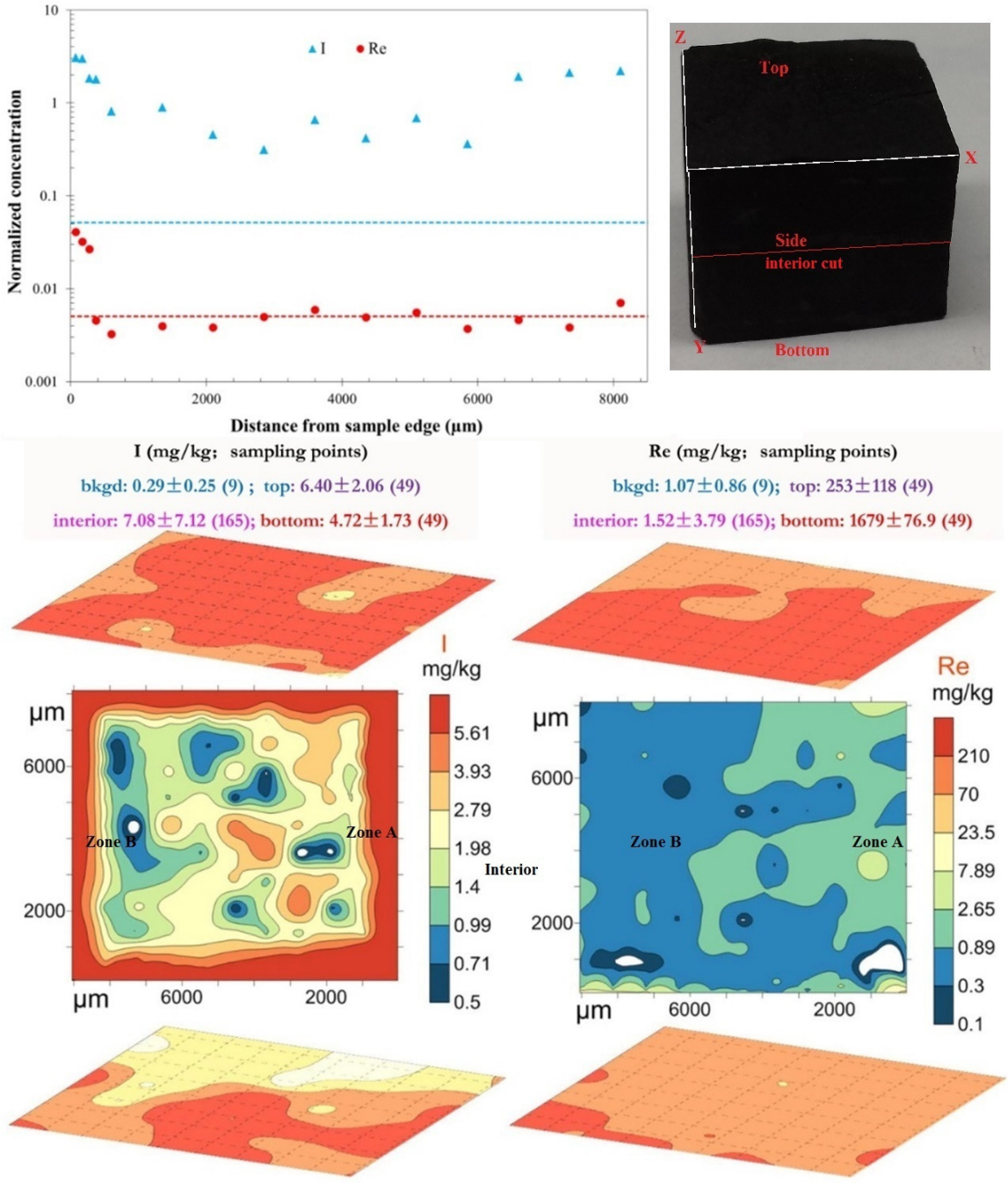

Figure 9: Profiles for organic-I and organic-Re tracers in the n-decane fluid after vacuum saturation-high pressure impregnation into sample 3931-U. Laser spot size for all faces is 100 μm. The spacing between spots is 1500 μm for both the top and bottom faces and 100 μm for the 1st 300 μm, which is then increased to 750 μm for the upward direction of the interior face.

4.6. Target production interval

In the case of the Woodford Shale in the Permian Basin, the higher TOC values (5.7-7.7%) for the Upper and Middle Woodford Members (3912-U to 3955-M) suggest that these intervals have high hydrocarbon generating potential. Moreover, production from a shale gas resource is influenced by a combination of several reservoir properties, and pore size distribution, wettability, mineralogical composition, porosity-permeability and TOC values are primary properties. This study shows that within the RTC Woodford core, based on mineralogical composition, the Upper and Middle Woodford Members belong to a category of silica-dominated lithotype, while the Lower Woodford is classified as a siliceous mudstone (Figure 10). These lithotype changes have a substantial influence on TOC, pore size distribution, wetting characteristics, the mechanical properties of the shale, and consequently the potential for shale gas development.

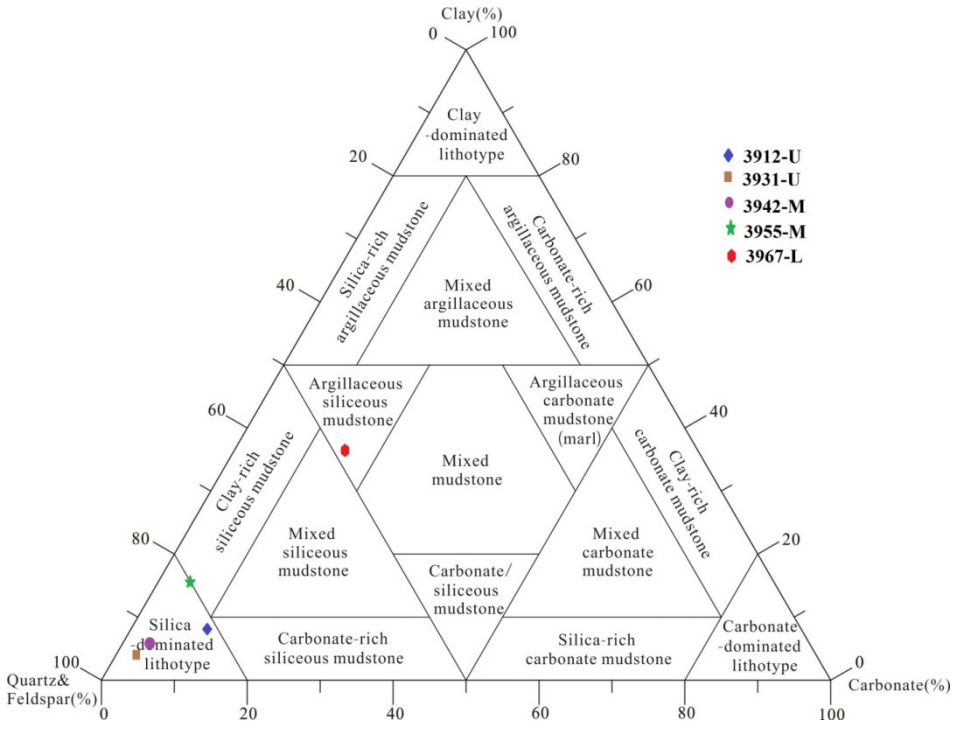

Figure 10: Schlumberger ternary diagram showing lithofacies of the five different samples.

Considering these reservoir properties based on our experimental results, we recommend that zone 3955-M is a suitable interval for hydraulic stimulation and hydrocarbon production. In this interval, TOC is 7.7%, brittle minerals (quartz+feldspar) measure 80.5%, there is low clay content of 4.4%, and porosity is moderate (1.25%). Due to the low permeability (1.45 nD) and medium pore-throat size (4.2 nm) of 3955-M; hydrofracturing is needed for viable hydrocarbon production. Quartz- and feldspar-dominated (80.5%) lithologies are more brittle and respond better to induced fracturing (Harris et al., 2011), while clay-dominated lithologies are more ductile, and clays may also swell when in contact with drilling fluids. Based on all these considerations, hydraulic fracturing within the 3955-M Woodford Member is the best to target. Tortuosity data indicate that the 3955-M zone has moderate tortuosity values among the other members, meaning that fracking will increase the flow of hydrocarbon more efficiently. Wettability and imbibition results show that the targeted zone is oil wet (imbibition slope 0.591 and contact angle 6.5° for n-decane) and moderately water wet (imbibition slope 0.33 and contact angle 54.7°). In addition, vitrinite reflectance ~1.17 R_o suggests that this member is within the wet gas window. Overall results indicate that possibly the best shale gas resource lies in the Middle Woodford.

5. Conclusions

In this paper, we consider nanopore structures (geometry and topology) and their relationship with fluids for Woodford core samples. Our experimental results indicate that pores within the Woodford Shale are predominantly in the nanometer size range, with a median pore throat diameter ranging from 3.7-5.4 nm, which is consistent with other shale basins. Based on these geometrical properties (narrow pore space, very low porosity, 0.8 to 4%, and 0.5-1.97 nD matrix permeability), the Woodford Shale is predicted to display restricted fluid flow.

Using several characterization methods to assess the shale's topology, we also confirm that pore connectivity in the Woodford Shale is quite low for hydrophilic fluids (DI water and API brine). For API brine and DI water, we observed low to moderate wettability, consistent with the Barnett Shale (Geo and Hu. 2016), and spontaneous imbibition showed a low imbibition slope, typical of sparsely connected hydrophilic pore networks. The impact of wettability on productivity is shown, for example, by Puntervold et al. (2008) about how wettability alteration and spontaneous imbibition are related to improved oil recovery for North Sea Chalk Formation. Edge-accessible pore distribution measured by spontaneous tracer imbibition and high-pressure intrusion steadily displayed a steep decline in accessible porosity with distance from the sample's external periphery, which indicates that only a small number of the inner pores are connected to the outside. All results point to the conclusion that pores more than a millimeter in size inside a sample are improbably connected to the peripheral area, which is shown by our tracers of different sizes.

This research bridges the gap between pore structure, pore connectivity, and wettability characteristics of the Woodford Shale. The results demonstrate that wettability and pore structure may be the most important restraints on petroleum movement and production. Nano-sized pore throats and mixed wettability characteristics may be the reasons for rapid production declines in shale hydrocarbon extraction. Future research will involve SEM imaging for pore-type characterization, as well as effective porosity determination as a function of sample size.

Acknowledgments

This research was supported by the Graduate Student Research Grant from the Gulf Coast Association of Geological Societies, National Natural Science Foundation of China (Nos. 41690134 and 51374265), National Science and Technology Major Project of China (No.

2016ZX05034-002-006), State Key Laboratory of Organic Geochemistry in Chinese Academy of Sciences in Guangzhou (No. OGL-201402), and the Fundamental Research Funds for the Central Universities (No. 2015XKZD03). Our special thanks go to Harold Rowe of Premier Oilfield for his assistance in sample procurement.

References

Aoudia, Khodi., 2009. Analysis of rock mechanical properties by mineralogy and their potential effects on hydraulic fracturing in the Woodford Shale, West Texas. M.S. thesis, Colorado School of Mines, 139 pp.

Borysenko, A., Clennell, B., Sedev, R., Burgar, I., Ralston, J., Raven, M., Dewhurst, D. and Liu, K., 2009. Experimental investigations of the wettability of clays and shales. Journal of Geophysical Research: Solid Earth, 114, p. B07202.

Cardott, B.J., Metcalf III, W.J. and Ahern, J.L., 1990. Thermal maturation by vitrinite reflectance of Woodford Shale near Washita Valley Fault, Arbuckle Mountains, Oklahoma. Rocky Mountain Section (SEPM), 139–146.

Cardott, B.J., 2012. Thermal maturity of Woodford Shale gas and oil plays, Oklahoma, USA. International Journal of Coal Geology, 103, 109–119.

Cardott, B.J., Landis, C.R. and Curtis, M.E., 2015. Post-oil solid bitumen network in the Woodford Shale, USA - A potential primary migration pathway. International Journal of Coal Geology, 139, 106–113.

Comer, J.B., 1991. Stratigraphic Analysis of the Upper Devonian Woodford Formation, Permian Basin, West Texas and Southeastern New Mexico (No. 201). Bureau of Economic Geology, the University of Texas at Austin.

Craig, Jr., F.F., 1971. The reservoir engineering aspects of waterflooding. Richardson, Texas, SPE Monograph Series 3, 12–44.

Crowe, C.W., 1969. Methods of lessening the inhibitory effects to fluid flow due to the presence of solid organic substances in a subterranean formation. U.S. Patent Office 3482636, patented on Dec. 9, 1969.

Dutton, S.P., Kim, E.M., Broadhead, R.F., Raatz, W.D., Breton, C.L., Ruppel, S.C. and Kerans, C., 2005. Play analysis and leading-edge oil-reservoir development methods in the Permian basin: Increased recovery through advanced technologies. AAPG Bulletin, 89(5), 553–576.

Ellison, S.P. Jr., 1950. Subsurface Woodford black shale, west Texas and southeast New Mexico. Bureau of Economic Report of Investigations, No. 7, 22 pp.

Energy Information Administration (EIA), 2014. Annual Energy Outlook 2014: With Projections to 2040, U.S. Department of Energy, DOE/EIA-0383, released on May 7, 2014.

Energy Information Administration (EIA), 2016. Natural Gas Gross Withdrawals and Production. (Available at https:// www.eia.gov/dnav/ng/ng_prod_sum_a_ EPG0_FGW_ mmcf_m.htm Accessed 17 May 2017)

Epstein, N., 1989. On tortuosity and the tortuosity factor in flow and diffusion through porous media. Chemical Engineering Science, 44(3), 777–779.

Ewing, R.P. and Horton, R., 2002. Diffusion in sparsely connected pore spaces: Temporal and spatial scaling. Water Resources Research, 38(12), DOI: 10.1029/2002WR001412.

Fernø, M.A., Haugen, Å. and Graue, A., 2011. Wettability effects on the matrix–fracture fluid transfer in fractured carbonate rocks. Journal of Petroleum Science and Engineering, 77(1), 146–153.

Fick, A., 1855. V. On liquid diffusion. Philosophical Magazine Series 4, 10(63), pp.30-39.

Galley, J.E., 1958. Oil and geology in the Permian Basin of Texas and New Mexico, in Weeks, L. G., ed., Habitat of oil. Tulsa, Oklahoma, American Association of Petroleum Geologists, 395–446.

Gao, Z.Y., and Hu, Q.H., 2013. Estimating permeability using median pore-throat radius obtained from mercury intrusion porosimetry. Journal of Geophysical Engineering, 10, 025014.

Gao, Z.Y., and Hu, Q.H., 2016. Wettability of Mississippian Barnett Shale samples at different depths: Investigations from directional spontaneous imbibition. AAPG Bulletin, 100(1), 101–114

Ghanbari, E. and Dehghanpour, H., 2015. Impact of rock fabric on water imbibition and salt diffusion in gas shales. International Journal of Coal Geology, 138, 55–67.

Gupta, N., Supratik S., and Kurt J.M., 2013. Seismic attribute driven integrated characterization of the Woodford Shale in west-central Oklahoma. Interpretation 1, No. 2, SB85-SB96.

Hackley, P.C. and Cardott, B.J., 2016. Application of organic petrography in North American shale petroleum systems: A review. International Journal of Coal Geology, 163, 8–51.

Hager, J., 1998. Steam drying of porous media. Ph.D. thesis, Department of Chemical Engineering, Lund University, Sweden.

Handy, L.L., 1960. Determination of effective capillary pressures for porous media from imbibition data. Trans. AIME 219, 75-80.

Harris, N.B., Miskimins, J.L. and Mnich, C.A., 2011. Mechanical anisotropy in the Woodford Shale, Permian Basin: Origin, magnitude, and scale. The Leading Edge, 30(3), 284–291.

Harris, N.B., Mnich, C.A., Selby, D. and Korn, D., 2013. Minor and trace element and Re–Os chemistry of the Upper Devonian Woodford Shale, Permian Basin, West Texas: Insights into metal abundance and basin processes. Chemical Geology, 356, 76–93.

Hemmesch, N.T., Harris, N.B., Mnich, C.A. and Selby, D., 2014. A sequence-stratigraphic framework for the Upper Devonian Woodford Shale, Permian Basin, West Texas. AAPG Bulletin, 98(1), 23–47.

Hu,Q.H., Persoff, P., and Wang, J.S.Y., 2001. Laboratory measurement of water imbibition into low-permeability welded tuff. Journal of Hydrology, 242, 64–78.

Hu, Q.H., and Wang, J.S.Y., 2003. Aqueous-phase diffusion in unsaturated geological media: A review. Critical Reviews in Environmental Science and Technology, 33(3), 275–297.

Hu, Q.H., Ewing, R.P., and Dultz, S., 2012. Pore connectivity in natural rock. Journal of Contaminant Hydrology, 133, 76–83.

Hu, Q.H., Ewing, R.P. and Rowe, H.D., 2015. Low nanopore connectivity limits gas production in Barnett formation. Journal of Geophysical Research: Solid Earth, 120(12), 8073–8087.

Hu, Q.H., Liu, H., Yang, R., Zhang, Y.X., Kibria, G., Sahi, S., Alatrash, N., MacDonnell, F.M. and Chen, W., 2017. Applying molecular and nanoparticle tracers to study wettability and connectivity of Longmaxi Formation in Southern China. Journal of Nanoscience and Nanotechnology, 17(9),6284–6295.

Hunt, A., Ewing, R. and Ghanbarian, B., 2014. Percolation Theory for Flow in Porous Media (Vol. 880): Springer.

Javadpour, F., Fisher, D., and Unsworth, M., 2007. Nanoscale gas flow in shale gas sediments. Journal of Canadian Petroleum Technology, 46(10), 55-61

Katz, A.J., and Thompson A.H., 1986. Quantitative prediction of permeability in porous rock. Physical Review B, 34, 8179–81.

Katz, A.J. and Thompson, A.H., 1987. Prediction of rock electrical conductivity from mercury injection measurements. Journal of Geophysical Research: Solid Earth, 92(B1), 599–607.

Makhanov, K., Dehghanpour, H. and Kuru, E., 2013. Measuring liquid uptake of organic shales: A workflow to estimate water loss during shut-in periods. In SPE Unconventional Resources Conference Canada, Calgary, Alberta, Canada. SPE-167157-MS.

Matyka, M., Khalili, A. and Koza, Z., 2008. Tortuosity-porosity relation in porous media flow. Physical Review E, 78(2), p. 026306.

Mnich, C.A., 2009. Geochemical signatures of stratigraphic sequences and sea-level change in the Woodford Shale, Permian Basin. M.S. thesis, Colorado School of Mines, 101 pp.

Morrow, N.R., 1990. Wettability and its effect on oil recovery. Journal of Petroleum Technology, 42(12), 1476–1484.

Nelson, P.H., 2009. Pore-throat sizes in sandstones, tight sandstones, and shales. AAPG Bulletin, 93(3), 329–340.

Odusina, E.O., Sondergeld, C.H. and Rai, C.S., 2011. NMR study of shale wettability. In The Canadian Unconventional Resources Conference, Alberta, Canada. Society of Petroleum Engineers. SPE-147371-MS.

Puntervold, T. and Austad, T., 2008. Injection of seawater and mixtures with produced water into North Sea chalk formation: Impact of fluid-rock interactions on wettability and scale formation. Journal of Petroleum Science and Engineering, 63(1), pp.23-33.

Rowe, H., Hughes, N., and Robinson, K., 2012. The quantification and application of handheld energy-dispersive x-ray fluorescence (ED-XRF) in mudrock chemostratigraphy and geochemistry. Chemical Geology, 324, 122–131.

Salathiel, R., 1973. Oil recovery by surface film drainage in mixed-wettability rocks. Journal of Petroleum Technology, 25, 1216–1224.

Singh, H., 2016. A critical review of water uptake by shales. Journal of Natural Gas Science and Engineering, 34, 751–766.

Stauffer, D., and Aharony, A., 1994. Introduction to Percolation Theory. 2nd ed., Taylor and Francis, London.

Sulucarnain, I.D., Sondergeld, C.H. and Rai, C.S., 2012. An NMR study of shale wettability and effective surface relaxivity. In SPE Canadian Unconventional Resources Conference, Calgary, 30 October–1 November. SPE-162236-MS.

Takahashi, S. and Kovscek, A.R., 2010. Wettability estimation of low-permeability, siliceous shale using surface forces. Journal of Petroleum Science and Engineering, 75(1), 33–43.

Wang, S., Javadpour, F. and Feng, Q., 2016. Confinement correction to mercury intrusion capillary pressure of shale nanopores. Scientific Reports, 6: 20160, doi: 10.1038/srep20160.

Washburn, E.W., 1921. Note on a method of determining the distribution of pore sizes in a porous material. Proceedings of National Academy of Sciences in the United States of America, 7, 115–116.

Webb, P.A., 2001. An introduction to the physical characterization of materials by mercury intrusion porosimetry with emphasis on reduction and presentation of experimental data. Micromeritics Instrument Corporation, Norcross, GA. Instrument Corporation, 22 pp.

Yang, R., Hao, F., He, S., He, C., Guo, X., Yi, J., Hu, H., Zhang, S. and Hu, Q., 2017. Experimental investigations on the geometry and connectivity of pore space in organic-rich Wufeng and Longmaxi shales. Marine and Petroleum Geology, 84, 225–242.

Zhang, N., He, M.C., Zhang, B., Qiao, F.C., Sheng, H.L., and Hu, Q.H., 2016. Pore structure characteristics and permeability of deep sedimentary rocks determined by mercury intrusion porosimetry. Journal of Earth Science, 27(4), 670–676.

Chapter 3

Thermal maturity evaluation using Raman spectroscopy for shale oil samples of USA: Comparisons with vitrinite reflectance and pyrolysis methods

Md Golam Kibria[1], Souvik Das[1], Qinhong Hu[1*], Asish. R. Basu[1], Wenxuan Hu[2], and Subhadip Mandal[3]

[1]Department of Earth and Environmental Sciences, The University of Texas at Arlington, 500 Yates Street, Arlington, TX 76019

[2]Institute of Energy Sciences, Nanjing University, Nanjing, 210093, China

[3]Integrated Reservoir Solutions, Core Laboratories, Houston, Texas, USA 77040

Submitted to:

Petroleum Science

[*] Corresponding author: maxhu@uta.edu

Abstract

The assessment of thermal maturity is a critical step in source-rock-reservoir evaluations, commonly performed by various geochemical screening methods (e.g., pyrolysis and vitrinite reflectance). However, both methods are quite time-consuming, strenuous and can be erroneous. In this contribution, we attempt to establish an alternative approach to estimating thermal maturity using Raman spectroscopy, using 24 North American shale-oil samples with thermal maturity data generated by vitrinite reflectance (VR_o%) and pyrolysis (T_{max})-based maturity calculation (VR_e%). The representative shale samples are from Haynesville (East Texas), Woodford (West Texas), Eagle Ford and Pearsall (South Texas), as well as Gothic, Mancos and Niobrara shale (all from Colorado). The Raman spectra of disordered carbonaceous matters (D1 and G bands) of these samples were directly obtained from the rock chips without prior sample preparation. Using the Gaussian and Lorentzian distribution approach, thermal maturities were correlated with carbon G and D1. Raman Band Separation (RBS) peak, height and peak ratio, and the area ratio of different subpeaks. We found that the Raman band separation (RBS) displayed a better correlation for equivalent VR_e% than vitrinite reflectance VR_o%. Correlation graphs show that the samples with greater RBS values have higher thermal maturity. The RBS (D1-G) distance vs. known total organic carbon (TOC), free hydrocarbons (S1) and the remaining hydrocarbon generating potential (S2) indicate that the RBS (D1-G) distance is also related to types of kerogen groups. However, some mature samples show a high (D1-G) distance with low values of TOC, S1, and S2, indicating expelled hydrocarbons. Considering the three primary methods of maturity determination of shale and their pitfalls, this study demonstrates the use of Raman spectroscopy as a quick and superior approach for thermal maturity assessment.

1. Introduction

Advances in completion technologies have recently revolutionized oil and gas production of source-rock reservoir plays in North America (Curtis, 2002; Hart et al., 2013; Jarvie et al., 2007; Hu et al., 2015; Kibria et al., 2018). The critical aspects in evaluating these plays are the geochemical evaluation (screening), specifically, assessing the quantity, quality, and thermal maturity of sedimentary organic matters with the implication in hydrocarbon generation, retention, and expulsion (Carvajal-Ortiz and Gentziz, 2015). The thermal maturity assessment of source-rock reservoir rocks is routinely performed using pyrolysis (T_{max}) and vitrinite reflectance (VR_o%) data, though there are some other less efficient methods available, such as spore coloration index, solid bitumen reflectance and spectral micro-fluorescence (e.g., Tissot 1984; Taylor et al., 1998).

Petrographic observations of shiny vitrinite bands perform vitrinite reflectance -based maturity assessment, the remains of woody materials, commonly found in source-rock-reservoir rocks, such as shales. Vitrinite reflectance (VR_o%) value increases with maturity (generally a function of depth) due to progressive changes in aromatization, condensation, and preferred arrangement of vitrinite molecular structure (McCartney and Teichmüller, 1972; Levine and Davis, 1984; Carr, 1999). Although this method is effective and widely used, it is expensive, labor-intensive, and dependent on organic petrographer's skill that can significantly vary person-to-person. Hackley et al. (2016) showed that the identification between vitrinite macerals and different macerals, such as various types of solid bitumens, inertinite, and semi-fusinite, is challenging. Moreover, large variations (20–30 %) in vitrinite reflectance of the same sample determined by different laboratories are a common problem.

Another widely used maturity assessment method, pyrolysis, involves thermal decomposition of organic matter in an inert atmosphere (Peters, 1986; Lafargue et al., 1998) yielding a peak temperature for pyrolysis of kerogen (T_{max}), along with other parameters, such as S1, S2, and S3. Additionally, a broad S2 peak in pyrogram often compromises the accuracy of T_{max} value. Peters 1986 showed that when $S_2 \leq 1$ mg HC/g rock or the formation is low organic-bearing, the measured T_{max} value could be unreliable and provides a wrong vitrinite reflectance equivalent.

Raman spectroscopy is potentially a better technique for non-destructive, rapid and precise maturity evaluations of hydrocarbon source rocks (Kelemen and Fang, 2001; Marshall et al., 2010; Wilkins et al., 2014). In recent years, Raman spectroscopy is emerging as an indispensable method that provides information about the short-range structural and chemical properties of carbon materials (e.g., Ferrari and Robertson, 2000; Beyssac et al., 2002; Xie et al., 2008; Wilkins et al., 2014, 2015; Schito et al., 2017; Sauerer et al., 2017; Schmidt et al., 2017, Khatibi et al., 2018, An et al., 2018). This method further can be used to study small, dispersed maceral grains that are difficult to study by other methods. This technique enables the analysis of data where the peaks of carbon are resolved into Gaussian bands (Wilkins et al., 2014). The Raman spectrum of the graphitic carbon materials show two primary bands G band (graphitic) near ~ 1580 cm^{-1} and D band (disordered) around ~ 1350 cm^{-1} (Tuinstra and Koenig, 1970; Gruber et al., 1994; Spotl et al., 1998; Kelemen and Fang, 2001; Marshall et al., 2010; Schito et al., 2017). However, with the increase in thermal maturity, the D and G peaks shift towards lower and higher wavelengths, respectively. The distance between G and D peaks is called Raman Band Separation (RBS), used as a reliable maturity indicator (Kelemen and Fang, 2001; Marshall et al., 2010; Wilkins et al., 2014; Sauerer et al., 2017; Schito et al., 2017).

Another important issue in all these recent works is that only the vitrinite reflectance is considered as the primary benchmark for their correlation purpose with Raman spectral data. The main problem with these works is that the vitrinite reflectance itself shows 10%–30% error as the measurement is based on the personal skill which is inconsistent. Recent studies such as Sauerer et al. (2017) conducted on 11 samples that are all type II organic matter, while Kelemen and Fang (2001) worked on shale samples of type II, and Spotl et al. (1998) on type III organic matter (OM), respectively. The studies of Wilkins et al. (2015) and Schito et al. (2016) are based on core samples at different depths from a single well and were correlated with Raman spectroscopy, while Khatibi et al. (2018) concentrated only on Willison basin, North Dakota. Our study will study Raman spectroscopy-based maturity assessment on samples from several different basins across the USA (Table 1). In this contribution, Raman spectral data are compared with both vitrinite reflectance based maturity, and pyrolysis derived equivalent reflectance maturity of the same samples. In contrast with other studies, we examine here the correlation of different Raman spectral parameters data with maximum, minimum and average vitrinite reflectance thermal maturity, and equivalent vitrinite reflectance (derived from pyrolysis experiments T_{max} value). Another unique aspect of our present study is that it focusses on the various type of kerogen material – Type II-III, Type III and Type IV.

2. Samples and methodologies

2.1. Samples

Twenty-four samples with known VR_o% (16 samples) and VR_e% (24 samples) were selected from multiple organic-rich mudstones, shale and chalk formations in active USA source-rock reservoir play (Table 1). The age of these samples ranges from Late Devonian to Cretaceous.

The total organic carbon (TOC) content in these samples varies between 0.74 wt% and 7.80 wt%. Samples were obtained as 10–20 gm splits from mostly drill cores (sidewall plugs), other than Eagle Ford samples those are from outcrops. Cores were chipped into pieces approximately 10 – 15 mm size cube for the Raman spectroscopy analyses. The powdered shale sample fractions (< 75 μm) were used to determine TOC using both Shimadzu TOC–VWS wet chemical total organic carbon analyzer in the University of Texas at Arlington, USA and a Leco CS-200 carbon/sulfur analyzer in Nanjing University, China. The pyrolysis (< 75 μm) and vitrinite reflectance data (core chips) were obtained from external laboratories, as described below.

Table 1: Samples depth, location, formation name, age, lithology, and maturity.

No.	Sample ID	Depth(m)	Location	Formation	Age	Lithology	VR_o%	Equivalent VR_e%	RBS (cm^{-1})
1	TX W-3912	3912.11	Pecos Co., TX	Woodford	Late Devonian-Early Mississipian	Shale/Mudrock	1.17±0.05 (N=31)	0.96	259.06±2.17
2	TX W-3930	3930.70						1.32	260.34±3.07
3	TX W-3941	3941.67						1.10	259.86±2.54
4	TX W-3955	3955.39						0.87	256.10±3.01
5	TX P-3987	3587.80	La Salle Co., TX	Pearsall	Lower Cretaceous	Shale/Mudrock	1.57±0.38 (N=29)	0.98	249.41±3.78
6	TX P-3609	3609.44						1.12	256.48±3.22
7	TX P-3635	3635.04						1.16	256.10±2.77
8	TX H-3346	3346.40	Harrison Co., TX	Haynesville	Jurassic	Shale/Mudrock		1.41	262.03±3.64
9	TX H-3374	3374.44						1.14	257.93±3.05
10	TX H-3421	3421.68					1.36±0.31 (N=20)	1.68	263.77±3.17
11	CO G-1797	1797.71	Montezuma Co., CO	Gothic	Pennsylvanian	Shale/Mudrock		0.89	256.49±1.86
12	CO G-1798	1798.62					1.40±0.14 (N=18)	1.64	268.05±3.78
13	CO G-1825	1825.45					1.17±0.22 (N=21)	0.92	243.26±2.06
14	CO G-2664	2664.26					1.03±0.24 (N=22)	1.03	251.39±3.87
15	CO M-725	725.42	Rio Blanco Co., CO	Mancos	Cretaceous	Shale/Mudrock	0.37±0.13 (N=18)	0.65	251.98±4.20
16	CO M-727	727.25					0.37±0.13 (N=24)	0.51	241.87±1.79
17	TX EF outcrop		Val Verde Co., TX	Eagle Ford	Cretaceous		0.66±0.47 (N=31)	0.49	236.28±1.36
18	CO N-891	891.54	Larimer Co., CO	Niobrara	Cretaceous	Chalk	1.68±0.66 (N=16)	0.63	236.24±4.82
19	CO N-910	910.74				Marl/Shale	1.83±0.49 (N=20)	0.78	242.34±2.94
20	CO N-932	932.69				Marl/Shale	1.56±0.88 (N=25)	0.40	229.48±4.45
21	CO N-936	936.96				Chalk	1.48±0.47 (N=27)	0.76	247.81±1.73
22	CO N-947	947.01				Marl	1.86±0.65 (N=29)	0.76	251.67±1.36
23	NM BS-2908	2908.71	Lea Co., NM	1st Bone Spring	Permian	Dolomite	0.63±0.21 (N=28)	0.90	258.42±1.82
24	NM BS-2919	2919.98				Sandstone	0.63±0.18 (N=21)	0.80	260.34±2.73

Note: TX: Texas; CO: Colorado; NM: New Mexico; W: Woodford shale; P: Pearsall Shale; H: Haynesville shale; G: Gothic Shale; EF: Eagle Ford Shale: N: Niobrara Shale; BS: 1st Bone Spring Shale

2.2. Pyrolysis and organic richness

Pyrolysis was performed on an OCE-II oil−gas evaluation workstation following Chinese Technical Standard GB/T 18602-2012 (SAC, 2012) in the China University of Geoscience in Wuhan. Previous work has explained in details about different pyrolysis apparatus – their operations, measured parameters, potential pitfalls, and applications to petroleum exploration (Behar and Peletet., 1985; Espitalie´ 1986; Peters and Cassa, 1994; Lafargue et al., 1998; Cheshire et al., 2017). The OCE-II oil−gas evaluation workstation performs temperature–programmed heating to (1) thermally distil ‘‘free’’ or adsorbed hydrocarbons (S1 peak) from the sample, (2) pyrolyze the kerogen to produce hydrocarbons (S2 peak) in a second oven, and (3) residual organic carbon content in mg/g (S4 unit mass) of hydrocarbon source rock after pyrolysis. This instrument is not equipped with the S3 measurement unit which can detect unit mass of released carbon dioxide (mg/g) which yield during thermal breakdown of kerogen for hydrocarbon source rocks. The T_{max} is estimated based on S2 peak temperature that coincides with the maximum generation of hydrocarbons. The total hydrocarbon potential of the sample is defined by (S1+S2), the hydrogen index (HI) ~ S2/TOC, and Production Index (PI) ~ S1 / (S1+S2). Other parameters obtainable from Pyrolysis are the bitumen index (BI), defined as S1/TOC (Killops et al., 1998), and the quality index (QI) ~ (S1+S2)/TOC (Pepper and Corvi, 1995). The equivalent vitrinite reflectance is deduced from T_{max} (°C) using the following equation from (Jarvie et al. 2001; Jarvie, D. M. 2012): $VR_e\% = [0.018 \times T_{max}] - 7.16$. A calculated estimation of the uncertainty on T_{max} based upon duplicate analyses of identical sample splits is 3–5 °C for samples with S2 values > 10 mg HC/g rock, equivalent to an internal precision of ± 0.05–0.10 for the estimated $VR_e\%$.

2.3. Vitrinite reflectance measurements

Performed at Nanjing University and GeoMark Research, the samples were prepared according to procedures described by the American Society for Testing and Materials (ASTM) as shown in D2798 and D7708 (ASTM, 2015a, b; Hackley et al., 2016). Whole-rock samples were crushed to 20 mesh (850 μm or 0.85 mm size) particle size. Ground particles are placed in specially-designed plastic molds (1.5 inches or 3.3 cm in diameter) to mix with epoxy resin and hardener (ratio of 2:1), leaving it for hardening overnight. Sample grinding and polishing were performed using Buehler EcoMet/AutoMet 250 automated polishing equipment. The sample surface is scratch- and relief- free for reliable VR_o% measurements because poorly polished surfaces can lower the VR_o % values (Hackley et al., 2016). Reflectance in oil (VR_o %) and fluorescence analyses were performed using a Carl Zeiss Axio Imager A2m microscope. For each sample, at least 25 – 30 readings of VR_o% in different parts of the pellet were obtained. Each vitrinite-reflectance value used in this study is the mean random reflectance in percentage, as calculated from the arithmetic average of individual readings. The standard deviation is calculated as the square root of the variance and represents the spread of VR_o% values. All measurements are reported to two decimal places, allowing an assignment of thermal maturity to a specific position within a broad possible range.

2.4. Raman spectroscopy measurements

Raman spectroscopic measurements were made on the flat surface of rock chips with minimum sample preparation (such as flat the surface to fit into the stage on Raman spectroscopy), with the aim to establish a fast and convenient thermal maturation determination method with minimal laboratory preparation and analysis. All data in this study were obtained with a Thermo Scientific DXRxi Raman imaging spectroscopy. Spectra were generated mainly using 10× and

sometimes using 50× objectives, by monochromatic excitation with 532 nm wavelength laser dispersed by a fixed 900 lines/mm holographic grating. The laser spot size for analyses was 10 μm using 10× objective and 2 μm while using 50× objectives. The operating conditions were 1 – 5 seconds for spectral acquisition, 1 – 10 accumulations, and 0.7 – 5 mW for laser power. Though the DXRxi Raman imaging microscope is calibrated through auto alignment, Si (520.5 cm^{-1} peaks) is used to check the calibration. The Raman spectra were obtained and processed using the OMNICxi Raman Imaging software.

Sometimes carbonaceous matters do not produce useful Raman spectra because of the 'fluorescence' effect, from the presence of certain organic matter. The fluorescence effect depends upon the interaction between the laser and the organic materials being examined and is sensitive to acquisition time and laser power. To minimize this effect, statistically, large amounts of data were generated from each sample in different operating conditions so that all the RBS data given in this contribution are an average of 20 spectra collected from different positions of the same rock chip. Here we did not differentiate maceral type for collecting different kerogens spectra.

2.5. Curve fitting of Raman spectroscopy

Raman spectra of highly disordered carbon materials are affected by interference due to fluorescence caused by the presence of long chain alkenes and presence of aromatic compounds. The first step in the analysis of the spectra is the removal of the high fluorescence background by a baseline subtraction procedure. The baseline subtraction was performed using a third order polynomial curve that best represents the real trend of the fluorescence in the most immature samples with high background. To avoid errors induced by differences in the spectral range

considered by the subtraction, we fixed baseline points at 1100 and 1700 cm^{-1} for all spectra. Once the process was optimized, it must be then reproduced for the entire set of samples. Deconvolution and fitting of the Raman spectra were made using five peaks with mixed Gaussian/Lorentzian profiles and linear baseline correction (Origin 2017 software). No constraints were put on the peak parameters in the curve fitting procedure to allow an optimal fit to the measured spectra. We observed that the maximum difference resulting from baseline corrections was detected for the D band intensity, whose values tend to be higher by 10 – 15%. After removal of the background, the spectra were de-convoluted using Origin software. As the Raman spectra of organic matter (OM) in diagenetic conditions show broad overlapping bands and by the existence of multiple curve-fitting solutions (Lünsdorf and Lünsdorf, 2016), we found that the best solution using the minimum number of components could be attained using a five-band deconvolution with a mixed Gaussian–Lorentzian band profile. All spectra were split using the five-peak deconvolution procedure. The band positions, amplitudes (intensities), full-widths at half maximum (FWHM), and integrated areas of all peaks were extracted from the resulting curve fits. Although the 20 spectra for each sample showed significant ranges in the peak widths, intensities, and areas, the mean G and D1 band positions and the error estimations for G and D1 positions were determined with a 1σ error ranges between 0 – 5 cm^{-1}.

3. Results

3.1. Pyrolysis and equivalent reflectance

Table 2 shows TOC, S1, S2, kerogen type, T_{max} values and estimated values, such as HI, BI, QI, and PI, from Pyrolysis of 21 samples. The TOC value ranges between 0.74–7.8 wt %, S1 values are between 0.18 – 4.24 mg HC/g rock and S2 values around 0.23–10 mg HC/g rock (Table 2). Hydrogen index (HI) of these samples are between 12.1–262 mg HC/g TOC. The HI, values

lower than 100 mg HC/g TOC suggesting that most of the OM are thermally mature to post-mature.

Table 2: Geochemical characteristics of 21 samples derived from pyrolysis method.

No.	TOC (wt%)	S1 (mg/g)	S2 (mg/g)	Tmax (°C)	QI	HI	BI	PI	Kerogen type	Formation
1	6.57	1.23	1.16	451	2.39	18	0.19	0.51	IV	Woodford
2	3.03	1.00	1.96	471	2.96	65	0.33	0.34	III	
3	5.69	0.99	1.87	459	2.86	33	0.17	0.35	IV	
4	7.80	1.45	1.92	446	3.37	25	0.19	0.43	IV	
5	1.09	0.44	0.46	452	0.90	42	0.40	0.49	IV	Pearsall
6	3.75	1.56	2.02	460	3.58	54	0.42	0.44	III	
7	1.94	1.02	1.15	462	2.17	59	0.53	0.47	III	
8	2.42	0.53	0.51	476	1.04	21	0.22	0.51	IV	Haynesville
9	3.32	0.18	0.44	461	0.62	13	0.05	0.29	IV	
10	2.23	0.20	0.27	491	0.47	12	0.09	0.43	IV	
11	0.98	0.52	0.23	447	0.75	23	0.53	0.69	III	Gothic
12	1.56	0.72	0.44	489	1.16	28	0.46	0.62	III	
13	2.14	1.37	3.53	449	4.90	165	0.64	0.28	IV	
14	1.21	0.25	0.18	455	0.43	15	0.21	0.58	III	
15	0.89	0.23	0.67	434	0.90	75	0.26	0.26	III	Moncos
16	0.74	0.30	0.63	426	0.93	85	0.41	0.32	III	
18	2.49	3.48	6.47	419	9.95	260	1.40	0.35	II-III	Niobrara
19	3.61	4.24	10.00	433	14.24	277	1.17	0.30	II-III	
20	0.74	1.94	6.59	420	8.53	891	2.62	0.23	I	
21	1.80	1.90	4.72	440	6.62	262	1.06	0.29	II-III	
22	3.35	2.47	8.29	440	10.76	247	0.74	0.23	III	

S1=''free'' or adsorbed hydrocarbons, S2= remaining hydrocarbon,
QI=(S1+S2), HI=(S2/TOC), BI=(S1/TOC), PI= S1/(S1+S2)

It is important to note that five Niobrara samples yield high S1, S2, HI and (S1/TOC) ×100, and respective T_{max} values range between 419 and 440°C. Vitrinite reflectance equivalence from T_{max} is estimated as 0.38 to 0.76VR_e% (Table 1). Calculated PI values are within the range of 0.23 – 0.69. Based on the pyrolysis data, all our samples showed that one sample had type I kerogen, three samples with type II-III kerogen, nine samples with type III kerogen and 8 samples with

type IV kerogens. The T_{max} vs. HI cross plot of pyrolysis data showed that half the samples are II-III and III type and thermally mature to the postmature window which represents an oil-to-gas generation condition. Three samples are in immature condition, and the rest of the samples show an inert state (Fig. 1). A correlation graph for S2 vs. TOC indicates a direct correlation as the S2 value increases with the TOC value rise for the same sample (Fig. 2a). The T_{max} vs. Bitumin Index (BI) and Quality Index (QI) shows that the with increment in T_{max} value, the BI and QI value decreases (Fig. 2b and 2c). A cross plot between TOC and QI shows no correlation between the amount of TOC and QI (Fig. 2d).

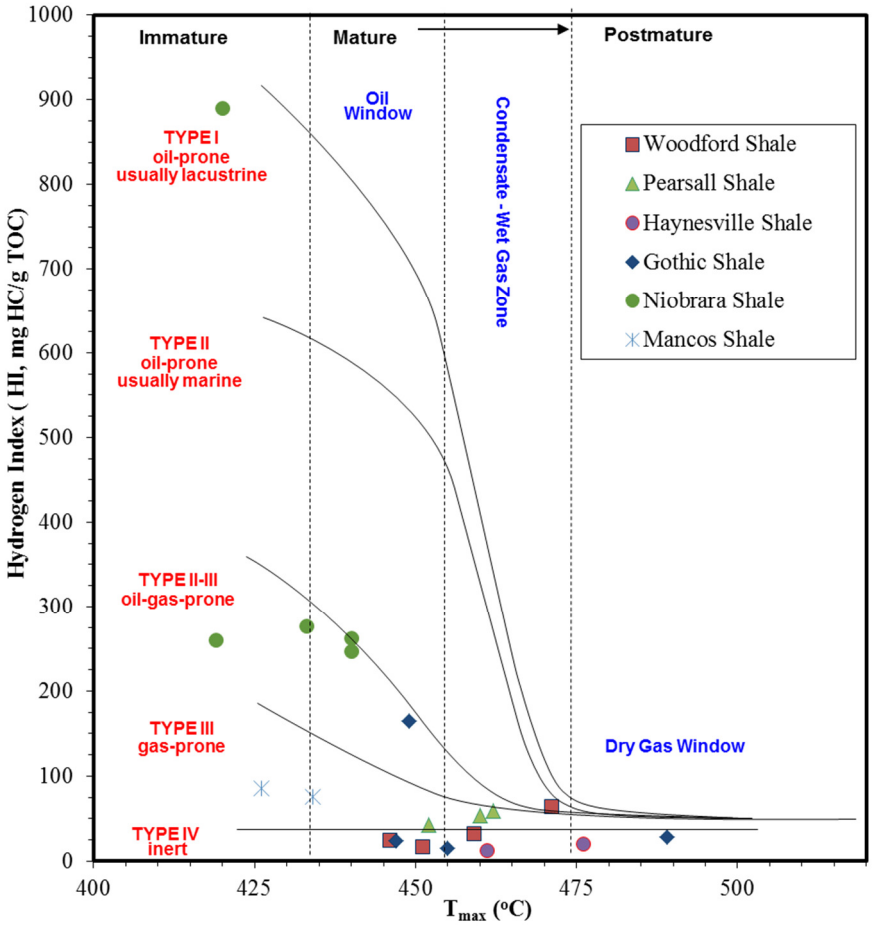

Fig. 1: Plot of hydrogen index (HI) versus pyrolysis T_{max} for the analyzed 21 samples, showing kerogen-type and thermal maturity stages.

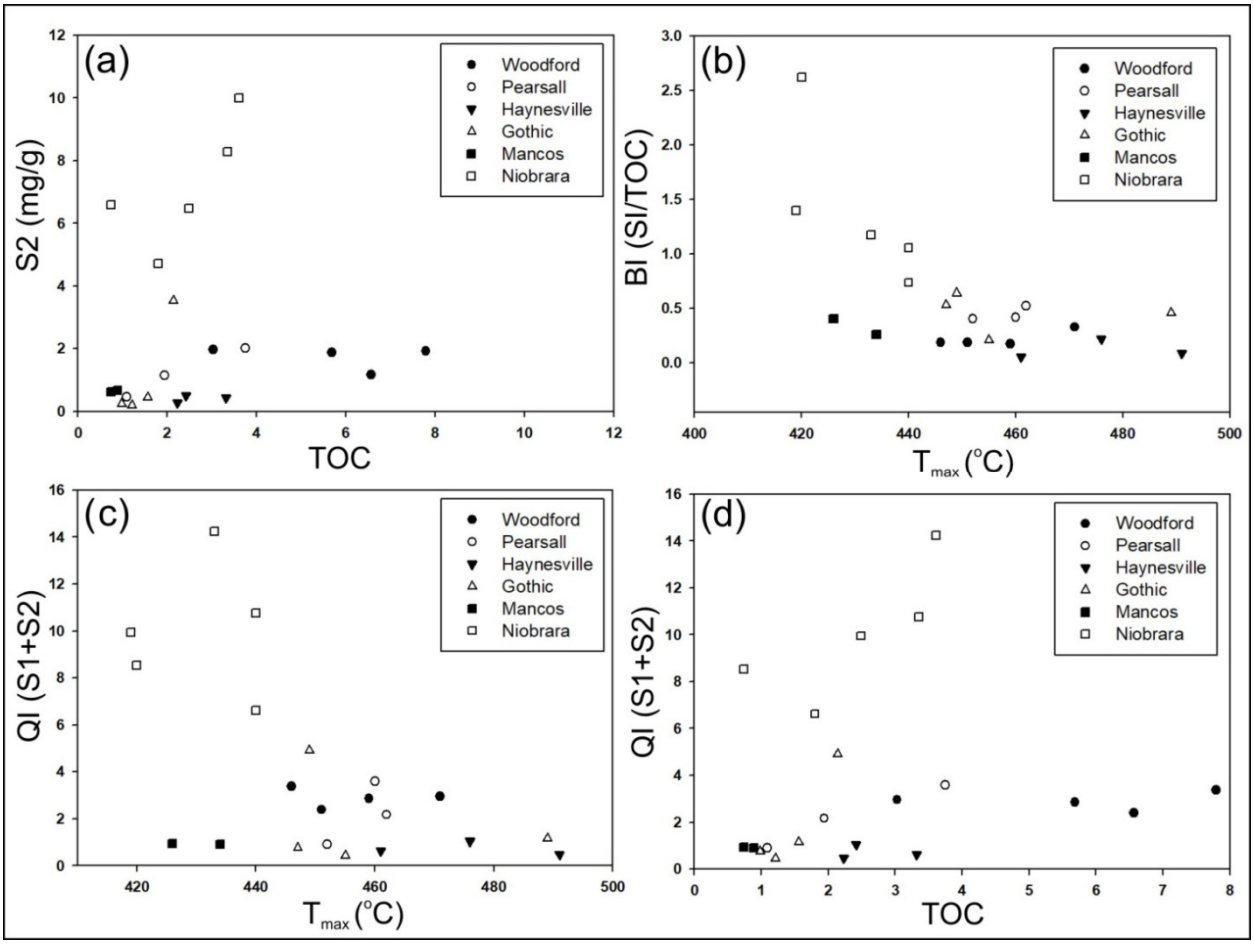

Fig. 2: Correlation between the measured parameters by pyrolysis: a) S2 vs. TOC; b) T_{max} vs. BI (S1/TOC); c) T_{max} vs. QI (S1+S2); d) TOC vs. QI (S1+S2)

3.2. Vitrinite reflectance and thermal maturity

In shale rock, the vitrinite maceral groups are organic matter derived from the woody tissue of post-Silurian vascular plants. The inertinite group maceral may have experienced combustion, oxidation or another carbonization process (e.g., desiccation). Liptinite group macerals include primarily algal material or amorphous organic matter (bituminite) derived from algal or bacterial predecessors. In the present study, organic petrological analyses of 16 samples showed vitrinite distribution and revealed the presence of all major maceral groups – bituminite, vitrinite, and

inertinite (Fig. 3). In general, 0–0.6 % VR_o represents bitumen and degraded vitrinite, 0.7–0.9 %VR_o represent low gray vitrinite, 1– 1.6 %VR_o suggests high grey vitrinite, and above 1.6 %VR_o indicates inertinite (Hackley and Cardott, 2016). Vitrinite reflectance measurements from the shale samples show a broader distribution of different maceral groups. Here some of the representative samples such as TX P-3987, TX EF outcrop, and CO N-910 indicate almost all type of maceral groups within their vitrinite counts (Fig. 3). The reported vitrinite reflectance value is an average of many (~30) measurements of vitrinite reflectance.

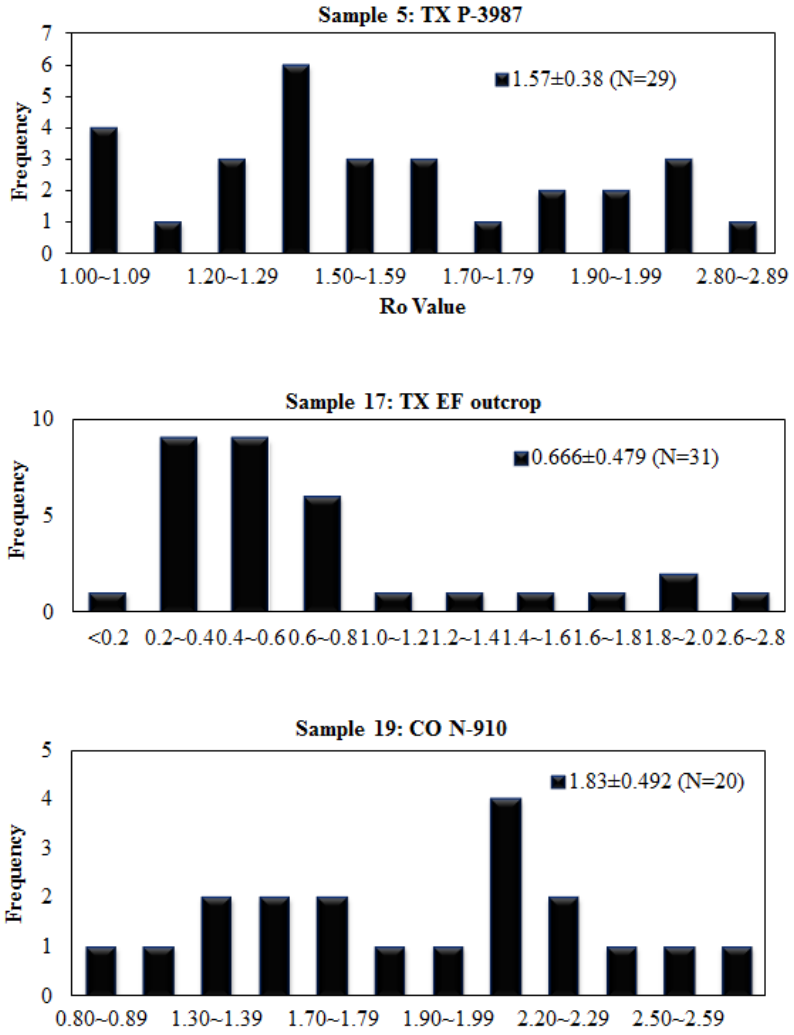

Fig. 3: Histograms of vitrinite reflectances from selected samples.

3.3. Raman Spectroscopy and Thermal maturity

The described fitting procedure was carried out on all sample spectra. An example of fitting spectra (Sample 5: TX P-3987) is shown in Fig. 4 about the position and band names of carbonaceous material on Raman spectra. Best-fit results were achieved by considering G and Dl as purely Gaussian, and D2, D3, and D4 as mixed Gaussian – Lorentzian functions. It is worth mentioning here that RBS is found as a more robust parameter than G and D1 band area ratio while comparing with equivalent reflectance (%VR_e). The efficacy of RBS with thermal maturity was also observed by Sauerer et al. (2017). The RBS vs. vitrinite reflectance (%VR_o) shows a poor correlation suggesting a higher error in petrographic measurements.

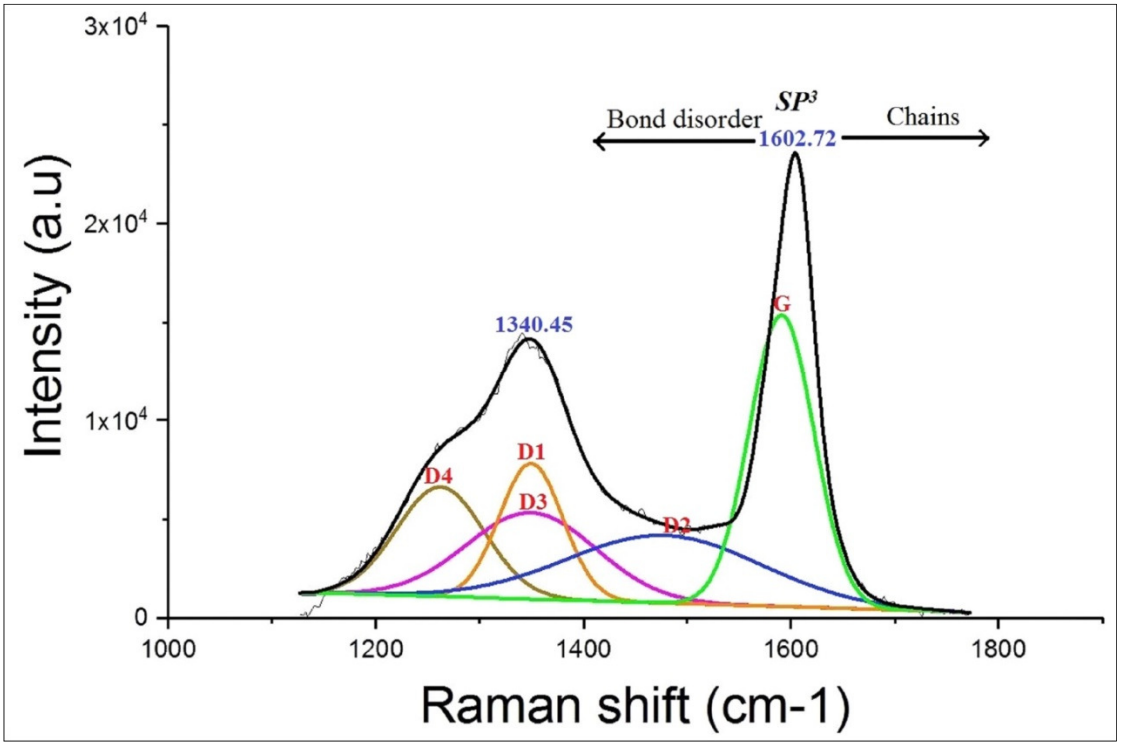

Fig. 4: Raman spectral characteristics of common five band deconvolution outcome for an organic matter spectrum. [Here D = disordered bands (1, 2, 3, 4) and G = graphitic band]

3.3.1. Correlation of Raman band separation (RBS =W_G –W_{D1}) with maturity

The D1 and G Raman bands represent processes occur at different carbonization ranks. The D1 band shift toward lower wavelength can be assigned to the growth of larger aromatic clusters passing from disordered to ordered organic material (Ferrari and Robertson, 2000). The Raman data plot of D1 – G distance vs. sample depth plot of organic shales in different basins shows an increase of RBS with sample depth (R^2=0.38) (Fig. 5a) and this increment in RBS suggests the higher degree of thermal maturity. The RBS distance increases with depth from about 225 cm^{-1} to 270 cm^{-1}. When correlating all the Raman data with both vitrinite reflectance VR_o% and equivalent vitrinite reflectance VR_e%, the higher shift of G position and lower shift of D1 position with vitrinite reflectance VR_o% shows weak relationship (Fig. 5c and 5e). The D1 band position shifts towards lower values with the increase in VR_e% from about 1370 cm^{-1} to 1330 cm^{-1} (Fig. 5d). Similarly, the G band position shows shift from 1592 – 1608 cm^{-1} with an increase in thermal maturity (Fig. 5f). The data show a modest correlation for an increase in the RBS distance with equivalent vitrinite reflectance determined by the shift of D1 position toward lower wavenumber (Fig. 5d, R^2=0.70) and G position toward higher wavenumber position (Fig. 5f, R^2=0.83). This observation is similar for RBS distance with the maturity (Ferrari and Robertson, 2000; Kelemen and Fang, 2001; Guedes et al., 2010; Liu et al., 2012; Lünsdorf and Lünsdorf, 2016). Our data clearly show that vitrinite reflectance-based maturity does not show a good correlation with RBS emphasized by previous researchers (e.g., Khatibi et al., 2018).

Tuinstra and Koenig (1970) reported that a vertical intensity ratio between G and D1 bands (ID1/IG) is related to the in-plane crystallite size in disordered graphite and represent a weak proportional correlation against T_{max} in a range between 420 and 500^{o}C. We observe that the ID1/IG ratio also has a weak correlation with the T_{max} value. Some researchers showed a

significant correlation between G and D1 band intensity vs. thermal maturity (Wilkins et al., 2014, 2015; Schito et al., 2017; Sauerer et al., 2017; Schmidt et al., 2017). However, the current study does not show any significant correlation (Fig. 6). The Raman band intensity largely depends on analytical condition, whereas wavenumber position is independent of the analytical condition and better represents the structural ordered/disordered mode of matter.

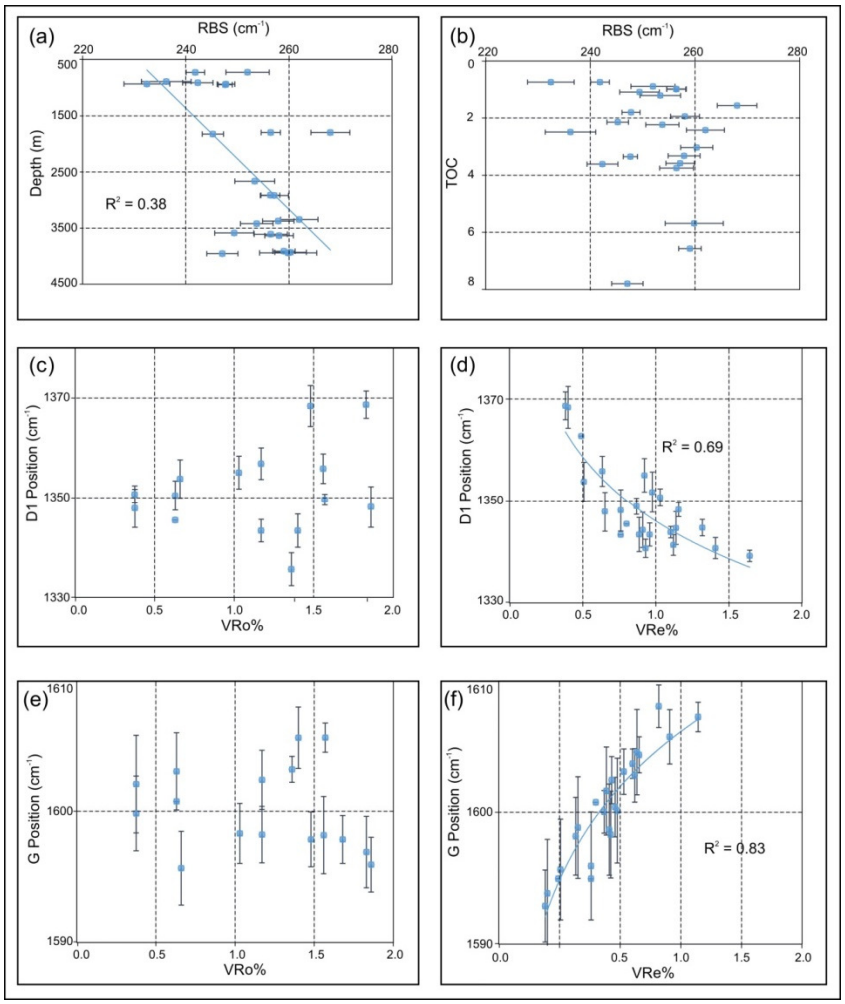

Fig. 5: Raman structural parameters correlation with depth, TOC and known maturity: a) RBS distance vs. depth b) RBS distance vs. TOC c) vitrinite reflectance VR_o% vs. D1 position d) equivalent VR_e% vs. D1 position e) vitrinite reflectance VR_o% vs. G position f) equivalent VR_e% vs. G position.

3.3.2. Correlation of Raman band area and band distance against thermal maturity

In this section, the distance and full width at half maximum (FWHM) of the D and G bands area takes into the consideration of connecting spectral features with thermal maturity. Here we use mainly two area ratios based on Raman spectra:

(1) area ratio 1 = D1 area/ G area

(2) area ratio 2 = D1 area/ (D1+D2+G) area

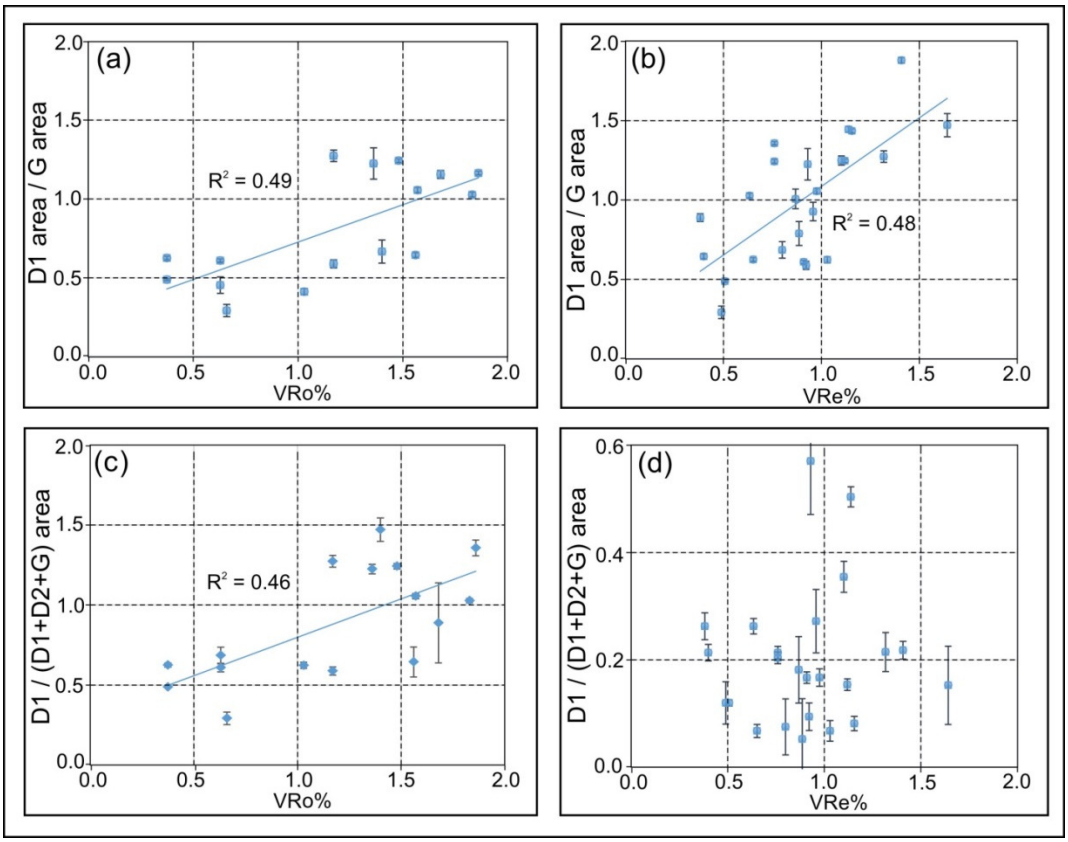

Fig. 6: The relationship between Raman structural parameters, different deconvolution band correlation as a function of known maturity: a) Vitrinite reflectance VR_o% vs. area ratio 1 b) Equivalent reflectance VR_e% vs. area ratio 1 c) Vitrinite reflectance VR_o% vs. area ratio 2 d) Equivalent reflectance VR_e% vs. area ratio 2.

These parameters are plotted against the maturity profile vs. vitrinite reflectance VR_o% and equivalent reflectance VR_e% (Fig. 6). Vitrinite reflectance VR_o% vs. area ratio 1 (D1 area/ G area) shows a moderate correlation ($R^2 = 0.49$). In Fig. 6a, an increase of area1 ratio indicates an increase in thermal maturity. Equivalent reflectance VR_e% vs. area1 also shows a moderate correlation ($R^2 = 0.48$) (Fig. 6b). Vitrinite reflectance VR_o% vs. area ratio 2 [D1 area/ (D1+D2+G) area] also shows a moderate correlation ($R^2 = 0.46$) representing an increase of area ratio 2 proportionally related to the increase of VR_o% (Fig. 6c). Equivalent VR_e% vs. area ratio 2 show very poor correlation (Fig. 6d).

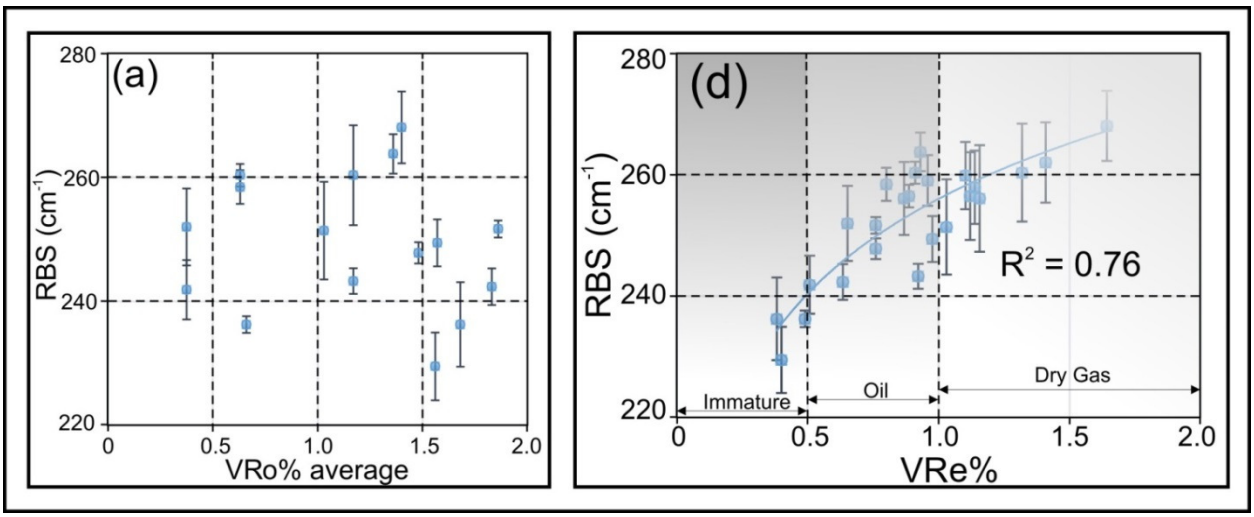

Fig. 7: Raman structural parameter plotted as a function of vitrinite and equivalent reflectance: a) Average vitrinite reflectance VR_o% vs. RBS distance b) Equivalent vitrinite reflectance VR_e% vs. RBS distance.

From Figs. 5c – 5f, it is observed that D1 values exhibit downshifting and G value upshifting with progressively higher thermal maturity. Fig. 7 displays the relationship between thermal maturities vs. RBS distance value and indicates an increasing trend. The correlation between RBS distance vs. vitrinite reflectance (VR_o%) and equivalent vitrinite reflectance (VR_e%)

demonstrates that the equivalent vitrinite reflectance data are more compatible with the Raman maturity method. Vitrinite reflectance VR_o% vs. RBS distance graph shows a weak correlation (Fig. 7a). This graph suggests that the RBS distance and VR_o% are directly proportional because the increase in RBS distance corresponds to higher VR_o%. In comparison, equivalent reflectance VR_e% vs. RBS distance plot displays an excellent nonlinear correlation (R^2= 0.76) (Fig. 7b). The graph shows that the equivalent VR_e% maturity increases with higher RBS distances. This study indicates that based on the relationship between equivalent reflectance VR_e% vs. RBS distance, thermal maturity can be estimated by direct Raman spectroscopic analyses. Pyrolysis-based T_{max} value vs. RBS distance represents a fair linear correlation (R^2 = 0.73), with an increase between D1 – G distance and T_{max}.

3.3.3. Correlation of RBS, pyrolysis, and kerogen type

The relationship between RBS distance and pyrolysis data shows that RBS distance vs. S1 (free remaining hydrocarbon) plot does not exhibit any direct relation. However, in general, it shows that small S1 values have large RBS distances. RBS distance vs. S2 (remaining generating hydrocarbon potential) graph shows a similar trend, with a smaller S2 value indicating higher RBS distance.

Fig. 8 shows the relationship of thermal maturity and RBS distance of different kerogen types. Vitrinite reflectance VR_o% vs. different kerogen type RBS distance graph represents that there is a weak correlation between kerogen type and vitrinite reflectance (Fig. 8a). A plot of equivalent vitrinite reflectance VR_e% vs. kerogen type RBS distance represents an excellent linear correlation for some kerogen type. Kerogen Type II-III signifies an excellent relationship with RBS distance (R^2= 0.98) (Fig. 8b). Kerogen Type III and IV also show a good relationship with

RBS distance. Equivalent vitrinite reflectance VR_e% maturity increase with higher RBS distance (R^2= 0.84) (Fig. 8b).

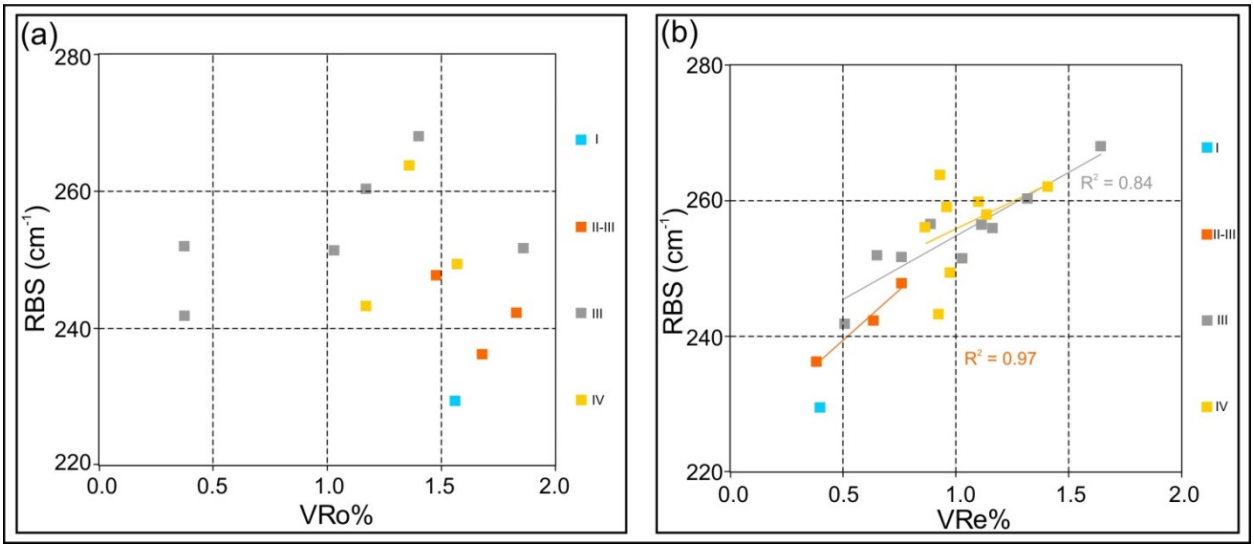

Fig. 8: Raman structural parameter correlations: a) Vitrinite reflectance VR_o% vs. RBS distance b) Equivalent reflectance VR_e% vs RBS distance.

4. Discussion

4.1 Pyrolysis and vitrinite reflectance

The samples used for the present study show a marked difference between vitrinite reflectance based thermal maturity and equivalent reflectance (T_{max}) based maturation. A correlation of thermal maturity with Raman band separation indicates that an equivalent VR_e% is more appropriate for correlation purposes. It is essential to consider both T_{max} and vitrinite reflectance VR_o% values within a geological context for a proper understanding of maturity due to complex relations between paleoenvironment of deposition, organic matter types, and diagenetic development of the sedimentary formation (Snowdon, 1995; Sykes and Snowdon, 2002; Dembicki, 2009; Carvajal-Ortiz and Gentzis, 2015). However, Fig. 9 (vitrinite reflectance VR_o%

vs. HI relationship) and Fig. 1 (equivalent VR_e% vs. HI) show that same samples have discrepancies in thermal maturity estimated by vitrinite reflectance and equivalent VR_e% methods. For example, sample 19 (CO N-910) T_{max} (433°C) values indicate that the organic matter is mature at the oil generation window (a conversion to equivalent VR_e% using the equation of Jarvie (2012) with an equivalent VR_e%=0.63%, while the measured vitrinite reflectance VR_o% values on the same sample 19 (CO N-910) (VR_o%=1.83±0.492%) specifies that the organic matter is postmature and in the dry gas generation window.

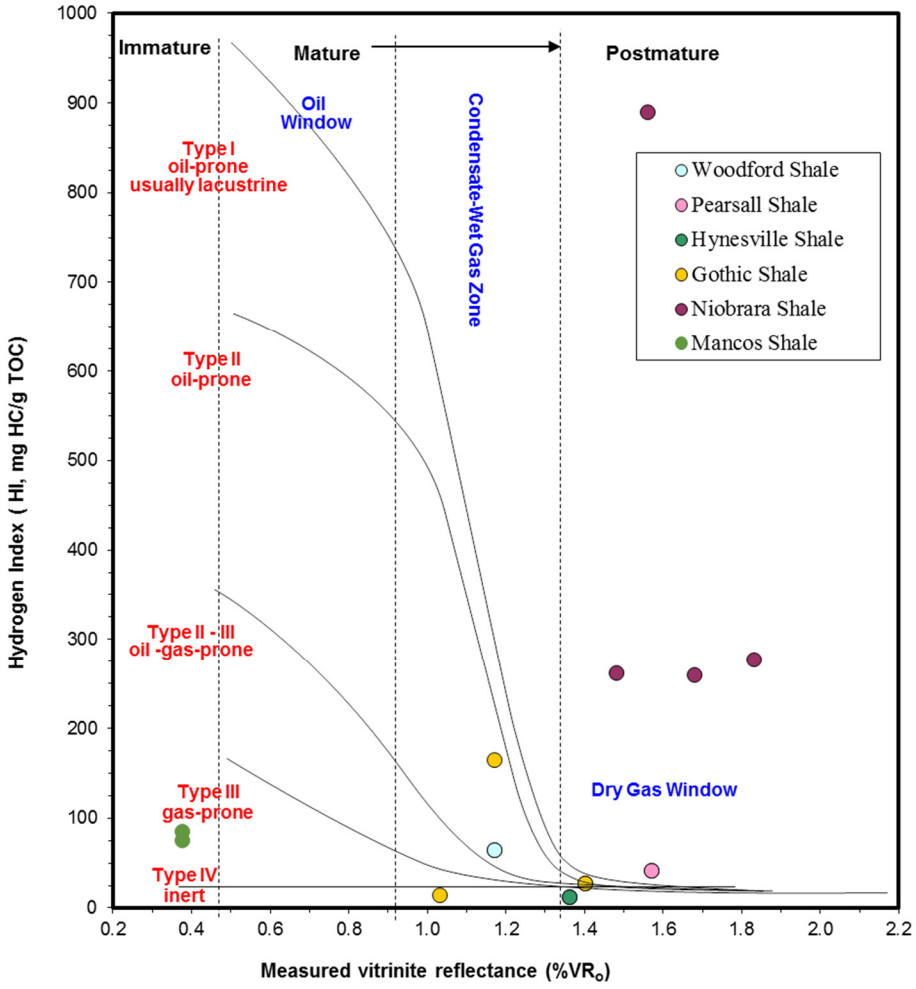

Fig. 9: Plot of Hydrogen index (HI) vs. measured vitrinite reflectance (VR_o%) for the analyzed samples, showing kerogen quality and thermal maturity stages.

Several researches have shown that an application of vitrinite reflectance to the determination of the thermal maturity of marine and lacustrine shales introduces frequent sources of error (Dennis, 1974; Carvajal-Ortiz and Gentzis, 2015). One of the critical issues is that the vitrinite reflectance scale is based on coal materials. Due to the sedimentary reworking process of shale, the properties and volume of carbonaceous matters are expected to be different from coal. For this, the thermal maturity assessment method of shale should be different with respect to coal. Barker (1996) suggested a minimum of 20 maceral measurements for better statistical representation of constituent macerals. However, only 20 measurements can limit the validity of the calculated average value. For example, our sample No. 19 (Fig. 3) has 20 maceral observations. Meanwhile, there are no adequate data to outline a normalized distribution. Hackley and Cardott (2016) described that the most efficient method of the vitrinite reflectance estimation is to look not only at the mean value and the number of measurements, but also to the shape of the reflectance histogram, the spread of values, and photomicrographs of identified vitrinite.

4.2. Raman band parameter, area ratio and assignment for the dispersed organic matter

With the aid of Raman spectroscopy, D1 and G band positions are relevant to the development of different types of carbonaceous material within the shale samples. The long-chain aromatic clusters are transformed from disordered to ordered clusters when D1 bands shift toward lower wavenumbers (Fig. 5b; Ferrari and Robertson, 2000). The change in Raman shift of D1 position towards a lower wavenumber (Fig. 5b) and G position towards higher wavenumber values control the RBS distance (Fig. 5d), which clearly show a direct relation with thermal maturity (Fig. 7b). This observations support the previous researchers for Raman band shift but not with the vitrinite reflectance based maturity (Ferrari and Robertson, 2000; Kelemen and Fang, 2001; Guedes et al., 2010; Liu et al., 2012; Schito et al., 2017). In this current study, Raman spectral

data demonstrate best fits for equivalent vitrinite reflectance from pyrolysis. Fig. 7b demonstrates that the RBS distance is one of the best parameters to compare against thermal maturity.

In this work, the G band is fitted around 1603 cm^{-1} (Fig. 4) surrounded by a Lorentzian right site peak at 1610 cm^{-1}, and a Gaussian D2 peak around 1500 cm^{-1}. Heise et al. (2009) observed that D2 band corresponds to the same vibration of the G band in small size aromatic hydrocarbons. The D band area is decoupled to a central Lorentzian D band at 1340.45 cm^{-1}, and two outer area Gaussian band on D4, left-side of D, and D2, right-side of D respectively at 1250 and 1500 cm^{-1} that were assigned to identical vibrations of the D band but in small size aromatic domains.

In this study, we haven't observed a strong correlation between Raman intensity and maturity rather than strong correlation between D1/G area ratio and VR_e% (Fig. 6b). Moreover, several spot analyses at different analytical conditions from a single sample show a wide variation in Raman spectral intensity. The low correlation coefficient in band intensity vs. T_{max} plot suggests a lack of definite relationship, while Kelemen and Fang (2001) and Schito et al. (2017) found the most significant maturity relation with the G and D1 band intensity. Early workers also noticed that the D2 and D3 band areas decrease with the thermal maturity rise in shale (Li, 2007). The area ratio of D1 and G bands and parameters related to this ratio (area1 and area2) increases with the rise of thermal maturity (Fig. 6). Our results and earlier research showed that an increase of structural ordering increases the Raman shift value of D1 band, the Raman shift values of G, D2, and D3 band decrease (Ferrari and Robertson, 2000; Li, 2007; Rebelo et al., 2016). Rebelo et al. (2016) showed that D4 and D bands have a similar pattern of vibrational modes and structural units for D2 and D3 bands for nanotube. Schito et al. (2017) observed similar coupled behavior for these bands at increasing temperatures. However, our current study does not indicate any

maturation trend for this complex band. This result could be due to the different saturated and unsaturated hydrocarbon components in OM of the shale samples, or a variation of aromatic OM enrichment which has different responses of the excitation bands with increasing thermal maturity. At lower temperature (about 200–320^{o} C), carbonaceous material displays band D4 from $sp^3 - sp^2$ shells around 1250 cm^{-1} (Lahfid et al., 2010), which is also observed in the current study (Fig. 4). Lis et al. (2005) suggested that the heterogeneities in C–C and C–H compounds with aliphatics at low maturity stages ($VR_o\% < 1.5$) is complex, depending on corresponding structural variations. In general, these chemical changes are possible due to lesser numbers of branching in aliphatic chains, shortening of aliphatic chains, and formation of cyclic compounds. Beyssac et al. (2002) observed the presence of two additional bands in the Raman spectrum, one of the bands appears as a right end shoulder of the G band at approximately 1620 cm^{-1} if the sample is over-mature. In the present study, we don't have any over-matured samples; the D2 band is a wide band existing at around 1500 cm^{-1}.

4.3. Thermal maturity and kerogen type correlation from Raman spectroscopy

Estimated vitrinite reflectance equivalences of the samples were correlated with the Raman band separation (G band shift minus D1 band shift), as described in the earlier sections, and were found to correlate with thermal maturity (e.g., Kelemen and Fang, 2001; Schito et al., 2016; Sauerer et al., 2017 Cheshire et al., 2017). In this study, thermal maturity is determined using the equivalent vitrinite reflectance ($VR_e\%$) vs. RBS correlation from Raman measurements (Fig. 7b). Based on this correlation, the estimated thermal maturity is in the range of 0.5–1.8 $\%VR_e$ using unknown samples RBS (Fig. 7b). This correlation is based on type II-III, type III and type IV kerogen samples. It is worth mentioning here that the type IV is not important for hydrocarbon generation. Types II-III represent a nearly perfect correlation for thermal maturity (Fig. 8b) with

RBS (R^2=0.98), while type III showed a good correlation (R^2=0.84; Fig. 8b). This correlation can also be helpful to categorize kerogen types based on their RBS value trends for unknown samples. The most significant result of this study is that equivalent VR_e% has a much stronger correlation than vitrinite reflectance with thermal maturity, accompanying RBS increase with the increase of thermal maturity of the samples. The higher the maturity, the larger the RBS distance. Another important outcome of our study is that the Raman spectral intensity is not a useful parameter to estimate the thermal maturity.

5. Conclusion

Raman spectroscopy is currently a potential method for the assessment of the thermal maturity of shale samples. The present study demonstrates that with an increase in thermal maturity, D1 and G peaks shift towards lower and higher wavelengths respectively, which increases the Raman band separation (RBS). A total of 24 shale samples from different petroleum basins in the USA with a wide range of maturity (0.6 to 2 VR_o%) were used to document that RBS has a good correlation (R^2=0.76) with equivalent thermal maturity (VR_e%). Therefore, we can gauge the thermal maturity of shales by this method of curve fitting for unknown samples using laser Raman spectroscopy. All these correlations show that with the aid of Raman spectroscopy alone, the maturation windows for immature kerogen, oil, wet gas, and dry gas can be evaluated for unknown samples. The present study suggests that the Raman –based thermal maturity can be better correlated with equivalent VR_e% instead of vitrinite reflectance VR_o%. The conventional vitrinite reflectance (VR_o%) determination by petrography might produce a huge error. For this, we claim that the Raman spectroscopy based maturity estimation is a better alternative. We also claim here that the RBS method can be helpful to determine the T_{max}. Additionally, Raman spectra can be generated directly on drill cores and cutting chips without any sample preparation.

Further data mining of Raman spectra collection from different basin samples will be needed to refine and establish a fast, less – strenuous and quantitative method for measuring thermal maturity for unconventional petroleum prospect.

Acknowledgments

This research was partially supported by the Graduate Student Research Grants from the Gulf Coast Association of Geological Societies (GCAGS) and American Association of Petroleum Geologist (AAPG), by the University of Texas at Arlington, and by the Pioneer Natural Resources. We are grateful to Harry Rowe, Robert Villegas, Jordan Bevers, Paul Huggins, Marvin Dunbar, and Scott Leaseburge for their assistance in sample procurement.

References

An, Y.X., Qu, W.J., Yu, P.Z. and Lü, J.G., 2018. The assembly of a composite based on nano-sheet graphene oxide and montmorillonite. Petrol. Sci. 15(2), pp.366-374.

ASTM International, 2015a, ASTM D2798-11a: Standard test method for microscopical determination of the vitrinite reflectance of coal: West Conshohocken, Pennsylvania, ASTM International, 5 pp, doi:10.1520/D2798-11A.

ASTM International, 2015b, ASTM D7708-14: Standard test method for microscopical determination of the reflectance of vitrinite dispersed in sedimentary rocks: West Conshohocken, Pennsylvania, ASTM International, 10 p., doi:10.1520/D7708-14.

Barker, C.E., 1996. A comparison of vitrinite reflectance measurements made on whole-rock and dispersed organic matter concentrate mounts. Org. Geochem. 24(2), 251-256.

Behar, F. and Pelet, R., 1985. Pyrolysis-gas chromatography applied to organic geochemistry: structural similarities between kerogens and asphaltenes from related rock extracts and oils. J. Anal. Appl. Pyroly. 8, 173-187.

Beny-Bassez, C., Rouzaud, J., 1985. Characterization of carbonaceous materials by correlated electron and optical microscopy and Raman microspectroscopy. Scan. Electron Microsc. 1, 119–132.

Beyssac, O., Goffé, B., Chopin, C., Rouzaud, J., 2002. Raman spectra of carbonaceous material in meta-sediments: A new geothermometer. J. Metamorph. Geol. 20 (9), 859–871.

Carr, A.D., 1999. A vitrinite reflectance kinetic model incorporating overpressure retardation. Mar. Pet. Geol. 16 (4), 355-377.

Carvajal-Ortiz, H. and Gentzis, T., 2015. Critical considerations when assessing hydrocarbon plays using Pyrolysis and organic petrology data: Data quality revisited. Int. J. Coal Geol.152, 13-122.

Cheshire, S., Craddock, P.R., Xu, G., Sauerer, B., Pomerantz, A.E., McCormick, D. and Abdallah, W., 2017. Assessing thermal maturity beyond the reaches of vitrinite reflectance and Pyrolysis: A case study from the Silurian Qusaiba formation. Int. J. Coal Geol. 180, 29-45.

Curtis, J.B., 2002. Fractured shale-gas systems. AAPG Bull. 86(11), 1921-1938.

Dembicki Jr, H., 2009. Three common source rock evaluation errors made by geologists during prospect or play appraisals. AAPG Bull. 93(3), 341-356.

Dennis, M.S., 1974. Interpretation of vitrinite reflectance measurements in sedimentary rocks and determination of burial history using vitrinite reflectance and authigenic minerals. Geol. Soc. Am. 153, p.31.

Diessel, C.F.K., Brothers, R.N., Black, P.M., 1978. Coalification and graphitization in high pressure schists in New Caledonia. Contrib. Mineral. Petrol. 68, pp. 63–78.

Dow, W.G., 1977. Kerogen studies and geological interpretations. J. Geochem. Explor. 7, 79-99.

Espitalié, J., 1986. Use of T_{max} as a maturation index for different types of organic matter. Comparison with vitrinite reflectance. J. Burrus (Ed.), Thermal Modelling in Sedimentary Basins, Editions Technip, Paris. 475-496

Ferralis, N., Matys, E.D., Knoll, A.H., Hallmann, C., Summons, R.E., 2016. Rapid, direct and non-destructive assessment of fossil organic matter via microRaman spectroscopy. Carbon 108, 440–449.

Ferrari, A.C., and Robertson, J., 2000. Interpretation of Raman spectra of disordered and amorphous carbon. Phys. Rev. B 61(20), 14095-14107.

Gruber, T., Zerda, T.W. and Gerspacher, M., 1994. Raman studies of heat-treated carbon blacks. Carbon 32(7), 1377-1382.

Guedes, A., Valentim, B., Prieto, A.C., Rodrigues, S. and Noronha, F., 2010. Micro-Raman spectroscopy of collotelinite, fusinite and macrinite. Int. J. Coal Geol.83(4), 415-422.

Hackley, P.C., Cardott, B.J., 2016. Application of organic petrography in North American shale petroleum systems: A review. Int. J. Coal Geol., 163, 8–51.

Hart, B. S., Macquaker, J. H., and Taylor, K. G., 2013. Mudstone ("shale") depositional and diagenetic processes: Implications for seismic analyses of source-rock reservoirs. Interpret. 1(1), B7-B26.

Heise, H., Kuckuk, R., Ojha, A., Srivastava, A., Srivastava, V., Asthana, B., 2009. Characterization of carbonaceous materials using Raman spectroscopy: a comparison of carbon nanotube filters, single-and multi-walled nanotubes, graphitised porous carbon and graphite. J. Raman Spectros. 40, 344–353.

Hu, Q.H., Liu, X.G., Gao, Z.Y., Liu, S.G., Zhou, W. and Hu, W.X., 2015. Pore structure and tracer migration behavior of typical American and Chinese shales. Petrol. Sci. 12(4), pp.651-663.

Jarvie, D.M., Claxton, B., Henk, B., Breyer, J., 2001. Oil and Shale Gas from Barnett Shale, Ft. Worth Basin, Texas. AAPG National Convention, Denver, CO, USA June 3–6. (AAPG Search and Discovery Article #90906).

Jarvie, D.M., 2012. Shale resource systems for oil and gas: Part 2—Shale-oil resource systems. AAPG Memoir 97, 89-119.

Jarvie, D.M., Hill, R.J., Ruble, T.E. and Pollastro, R.M., 2007. Unconventional shale-gas systems: The Mississippian Barnett Shale of north-central Texas as one model for thermogenic shale-gas assessment. AAPG Bull. 91(4), pp.475-499.

Kelemen, S., Fang, H., 2001. Maturity trends in Raman spectra from kerogen and coal. Energy Fuels 15, 653–658.

Khatibi, S., Ostadhassan, M., Tuschel, D., Gentzis, T., Bubach, B. and Carvajal-Ortiz, H., 2018. Raman spectroscopy to study thermal maturity and elastic modulus of kerogen. Int. J. Coal Geol. 185, 103-118.

Kibria, M.G., Hu, Q., Liu, H., Zhang, Y. and Kang, J., 2018. Pore structure, wettability, and spontaneous imbibition of Woodford shale, Permian basin, west Texas. Mar. Pet. Geol., 91, pp.735-748.

Killops, S.D., Funnell, R.H., Suggate, R.P., Sykes, R., Peters, K.E., Walters, C., Woolhouse, A.D., Weston, R.J. and Boudou, J.P., 1998. Predicting generation and expulsion of paraffinic oil from vitrinite-rich coals. Org. Geochem. 29(1-3), 1-21.

Lafargue, E., Marquis, F., Pillot, D., 1998. Pyrolysis 6 applications in hydrocarbon exploration, production, and soil contamination studies. Oil Gas Sci. Technol. 53:421–437.

Lahfid, A., Beyssac, O., Deville, E., Negro, F., Chopin, C., Goffé, B., 2010. Evolution of the Raman spectrum of carbonaceous material in low-grade metasediments of the Glarus Alps (Switzerland). Terra Nova 22(5), 354–360.

Levine, J.R. and Davis, A., 1984. Optical anisotropy of coals as an indicator of tectonic deformation, Broad Top Coal Field, Pennsylvania. Geol. Soc. Am. Bull. 95(1), 100-108.

Li, C.-Z., 2007. Some recent advances in the understanding of the pyrolysis and gasification behaviour of Victorian brown coal. Fuel, 86, 1664–1683.

Lis, G.P., Mastalerz, M., Schimmelmann, A., Lewan, M.D., Stankiewicz, B.A., 2005. FTIR absorption indices for thermal maturity in comparison with vitrinite reflectance R 0 in type-II kerogens from Devonian black shales. Org. Geochem. 36, 1533–1552.

Liu, D., Xiao, X., Tian, H., Min, Y., Zhou, Q., Cheng, P., Shen, J., 2012. Sample maturation calculated using Raman spectroscopic parameters for solid organics: methodology and geological applications. Chin. Sci. Bull. 58, 1285–1298.

Lünsdorf, N.K. and Lünsdorf, J.O., 2016. Evaluating Raman spectra of carbonaceous matter by automated, iterative curve-fitting. Int. J. Coal Geol.160, 51-62.

Marshall, A.O., Wehrbein, R.L., Lieberman, B.S. and Marshall, C.P., 2012. Raman spectroscopic investigations of burgess shale–type preservation: a new way forwardraman spectroscopy of bst deposits. Palaios, 27(5), 288-292

McCartney, J.T. and Teichmüller, M., 1972. Classification of coals according to degree of coalification by reflectance of the vitrinite component. Fuel 51(1), 64-68.

Milliken, K.L., Rudnicki, M., Awwiller, D.N. and Zhang, T., 2013. Organic matter–hosted pore system, Marcellus formation (Devonian), Pennsylvania. AAPG Bull. 97(2), 177-200.

Nemanich, R., Solin, S., 1979. First-and second-order Raman scattering from finitesize crystals of graphite. Phys. Rev. B 20, 392.

Pepper, A.S. and Corvi, P.J., 1995. Simple kinetic models of petroleum formation. Part I: Oil and gas generation from kerogen. Mar. Pet. Geol.12(3), 291-319.

Peters, K.E. and Cassa, M.R., 1994. Applied source rock geochemistry: L.B. Magoon, W.G. Dow (Eds.), The Petroleum System – From Source to Trap. AAPG Memoir 60. 93-120.

Peters, K.E., 1986. Guidelines for evaluating petroleum source rock using programmed pyrolysis. AAPG Bull. 70(3), 318-329.

Rebelo, S.L., Guedes, A., Szefczyk, M.E., Pereira, A.M., Araújo, J.P., Freire, C., 2016. Progress in the Raman spectra analysis of covalently functionalized multiwalled carbon nanotubes: unraveling disorder in graphitic materials. Phys. Chem. Chem. Phys. 18, 12784-12796.

Sadezky, A., Muckenhuber, H., Grothe, H., Niessner, R., Pöschl, U., 2005. Raman microspectroscopy of soot and related carbonaceous materials: spectral analysis and structural information. Carbon 43, 1731–1742.

Sauerer, B., Craddock, P.R., AlJohani, M.D., Alsamadony, K.L., and Abdallah, W., 2017. Fast and accurate shale maturity determination by Raman spectroscopy measurement with minimal sample preparation. Int. J. Coal Geol.173, 150-157.

Schito, A., Corrado, S., Aldega, L., Grigo, D., 2016. Overcoming pitfalls of vitrinite reflectance measurements in the assessment of thermal maturity: the case history of the lower Congo basin. Mar. Pet. Geol.74, 59–70.

Schito, A., Romano, C., Corrado, S., Grigo, D. and Poe, B., 2017. Diagenetic thermal evolution of organic matter by Raman spectroscopy. Org. Geochem. 106, 57-67.

Schmidt, J.L., Hinrichs, R., Araujo, C.V., 2017. Maturity estimation of phytoclasts in strew mounts by micro-Raman spectroscopy. Int. J. Coal Geol. 173, 1–8.

Snowdon, L.R., 1995. Pyrolysis Tmax suppression: documentation and amelioration. AAPG Bull. 79(9), 1337-1348.

Spötl, C., Houseknecht, D.W. and Jaques, R.C., 1998. Kerogen maturation and incipient graphitization of hydrocarbon source rocks in the Arkoma Basin, Oklahoma and Arkansas: a combined petrographic and Raman spectrometric study. Org. Geochem. 28(9-10), 535-542.

Standardization Administration of the People's Republic of China (SAC), 2012. Rock Pyrolysis Analysis; GB/T 18602-2012; Standards Press of China: Beijing (in Chinese).

Sykes, R. and Snowdon, L.R., 2002. Guidelines for assessing the petroleum potential of coaly source rocks using pyrolysis. Org. Geochem. 33(12), 1441-1455.

Taylor, G.H., Teichmüller, M., Davis, A.C.F.K., Diessel, C.F.K., Littke, R. and Robert, P., 1998. Organic Petrology. Borntraeger, Berlin-Stuttgart, 704 p.

Tissot, B.P., 1984. Recent advances in petroleum geochemistry applied to hydrocarbon exploration. AAPG Bull. 68(5), 545-563.

Tuinstra, F., Koenig, J.L., 1970. Raman spectrum of graphite. J. Chem. Phys. 53, 1126–1130.

Wilkins, R.W., Boudou, R., Sherwood, N., Xiao, X., 2014. Thermal maturity evaluation from inertinites by Raman spectroscopy: the 'RaMM' technique. Int. J. Coal Geol.128, 143–152.

Wilkins, R.W., Wang, M., Gan, H. and Li, Z., 2015. A RaMM study of thermal maturity of dispersed organic matter in marine source rocks. Int. J. Coal Geol.150, 252-264.

Xie, Q., Guan, S., Jiao, D. and Geng, H., 2008. Relationship between components of inclusion and hydrocarbon accumulation in the Yunlong Depression, Chuxiong Basin. Petrol. Sci. 5(4), pp.314-321.

Chapter 4

Laboratory assessment of petrophysical characteristics of shales from the Haynesville and Pearsall Formations

Md Golam Kibria[1] and Qinhong Hu[1]

[1]Deapartment of Earth and Environmental Sciences, The University of Texas at Arlington, 500 Yates Street, Arlington, TX 76019, USA

Prepared for:

Journal of Petroleum Geology

* Corresponding author: maxhu@uta.edu

Abstract

This study compares reservoir characteristics of Haynesville and Pearsall Formations in Texas. With an estimated recoverable gas of about 75 trillion cubic feet (TCF), the Upper Jurassic Haynesville Shale Formation is of continual interest to the oil and gas industry. On the other hand, Pearsall Shale is a gas-bearing lower Cretaceous formation still at the development stage. Based on various complementary tests such as XRD, pyrolysis, vacuum saturation, N_2 gas physisorption, mercury intrusion porosimetry (MIP), wettability, and imbibition, this study tests and compares reservoir properties of core samples for these two shales. The upper Haynesville is clay-dominated with a porosity of 6.5-7%, the middle layer is carbonate mixed mudstone with a porosity of ~5.5%, and the lower layer is carbonate-dominated with a porosity of ~2%. These porosity values from vacuum saturation tests are consistent with MIP-based results of 4.2 to 5.9%. TOC values vary from 0.85–3.91 wt.%, and pyrolysis-derived maturity is 1.41 to 3.48 VR_e%. Spontaneous fluid imbibition into Haynesville shale exhibits a connectivity slope, based on log (imbibed mass)-log (time) scales, close to ¼ for deionized (DI) water, consistent with contact angle results of mixed-wet (45-52^o for DI water) but extreme oil-wet nature (<detection limit of 3^o for n-decane). MIP analyses show that the median pore-throat diameters for Haynesville shale are dependent on lithology. 60% of the pore volumes have pore-throats above 100 nm, and permeability from 0.2 to 145 μdarcy. The upper part of the Pearsall Formation is silicate-dominated, where middle and lower layers are carbonated-dominated. The average porosity of 2.5% determined by vacuum saturation and DI water immersion is larger than MIP based porosity of ~0.6%. TOC values vary from 0.84 to 3.9%, and pyrolysis based maturity is 0.98 to 1.16 VR_e%. Pearsall shale MIP analyses show that the median pore-throat diameters lie

between 0.01-3 µm and 70% of the pore throats by volume are greater than 100 nm, with the permeability of about 0.2 to 1.11 µdarcy. The overall findings from these experimental approaches provide an improved understanding of nanopore structure and mixed-wet characteristics of Haynesville and Pearsall Shale.

1. Introduction

The Haynesville Shale was first commercially produced in 2008 by Chesapeake Energy Corp; it was estimated to hold 75 trillion cubic feet of recoverable gas in 2011 and 195 trillion cubic feet in 2017 (Institute for Energy Research, 2011; U.S. Energy Information Administration, 2011; U.S. Geological Survey, 2017). From 2008 to 2009, 275 horizontal wells were drilled in the Haynesville formation and it reached its first production peak in 2011-2012 (Baihly et al., 2010; Rystad Energy, 2019). After three years of decline, production in the Haynesville bounced back in the fourth quarter of 2017. The primary reason for this bounce was the design of new drilling and completion operations (Oil & Gas Journal, 2018). Despite their significance gas recovery from shales, there are no pore structure and fluid movement studies of the Haynesville Shale in the literature.

Shale gas, as a type of clean fossil fuel, was first economically produced in the Barnett Shale by the development of hydraulic fracturing and horizontal drilling (Institute for Energy Research, 2011). After decades of exploration and production, the shale gas industry is facing a critical problem in that shale gas production always exhibits sharp declines after months or a few years of production (Javadpour et al., 2007; Ross and Bustin, 2009; Baihly et al., 2010). Shale heterogeneity and its controls on the evolution of porosity, pore geometry and permeability are still incompletely understood. In order to obtain steady production and reduced decline rate, research on the understanding of hydrocarbon migration behavior in tight shale has attracted continual attention (Soeder, 1988; Javadpour et al., 2007; Makhanov et al., 2012; Jarvie, 2012; Swami & Settari, 2012; Dehghanpour et al., 2013; Slatt & O'Brien, 2011; Zhou et al., 2014; Gao & Hu, 2016b; Shen et al., 2016; Yang et al., 2017).

For unconventional reservoir systems, in-situ permeability <0.1 mD and <10% porosity characterize a tight reservoir (Ross and Bustin, 2009; Zou et al., 2012). Especially when the connectivity of pore network is low, the slow diffusive transport of gas from the shale matrix into the fracture network will result in a low hydrocarbon recovery in tight formation reservoirs (Hu et al., 2015). Such reservoir characteristics are the result of poor macroscopic reservoir quality and complex microscopic pore structure (Zou et al., 2012; Huang et al., 2017; Xiao et al., 2017). The geometric shape, size, and distribution of pore throats and their connectivity express the nanopore system (Fu et al., 2015; Hu et al., 2017), and it has been shown that the nanopores play a critical role in controlling hydrocarbon flow and transport (Anovitz and Cole, 2015; Schmitt et al., 2015; Zhao et al., 2017). For this reason, characterizing the pore structure parameters, such as pore volume, size, surface area, shape, size distribution, connectivity and fractal dimensions, are critical to understanding hydrocarbon adsorption, desorption, diffusion and flow mechanisms (Ross and Bustin, 2009; Chen et al., 2011; Hao et al., 2013; Hu et al., 2014; Kibria et al., 2018).

Moreover, the producibility of the gas mainly depends on pores and their connectivity for storing and releasing gas (Mastalerz et al., 2013). Hence the pore structure, such as the fractal characteristics, is an important issue to study for sustainable fine-grained tight hydrocarbon resource development. Intensive research on shale, tight sandstone and carbonate has been carried out in recent years to improve understanding of the pore networks in fine-grained reservoirs (Loucks et al., 2009; Lønøy, 2006; Curtis et al., 2012; Liu et al., 2017). Insight into the nano-petrophysical properties surrounding porosity, permeability, rock-fluid interactions and dynamics and their relationship with the geochemical properties of formations will better allow

us to evaluate shale reservoir quality, determine how best to produce each formation and assess where they may be most productive.

In recent years, many advanced techniques have been used to study the micro-nano pore structure of tight reservoirs (Chalmers and Bustin, 2007; Ross and Bustin, 2007, 2009; Clarkson et al., 2013; Li et al., 2016). In this study of Haynesville and Pearsall Shales, low-pressure nitrogen (N_2) gas physisorption, mercury intrusion porosimetry (MIP), contact angle measurement, water immersion porosimetry (WIP), and spontaneous fluid imbibition using deionized (DI) water are used to determine the (1) pore structure (e.g., pore volume, pore size, surface area, pore shape, spatial distribution of pores, connectivity and fractal dimensions); (2) pore types (e.g., interparticle pores, inter-crystal pores, intraparticle pores and organic pores); (3) permeability of connected pore networks across mm-nm spectrum; (4) connectivity of pore space (e.g., capillarity, diffusivity, tortuosity, wettability).

2. Geologic background

The Haynesville Shale is a package within the upper part of the Upper Jurassic Haynesville Formation and was deposited in an area in northeast Texas and northwest Louisiana in the northern Gulf of Mexico basin (Figure 1). The total area of the Haynesville covers 9,000 square miles (Ground Water Protection Council, 2009; EIA, 2016). The structure, depositional model, and stratigraphy of the study area have been studied in detail by others (Goldhammer, 1998; Galloway, 2008; Mancini et al., 2008; Adams, 2009; Ewing, 2009; Hammes et al., 2011; Hammes and Frébourg, 2012; Nunn, 2012; Cicero and Steinhoff, 2013). The tectonic opening of the Gulf of Mexico and Sabine uplift played a critical role in the Haynesville Shale deposition by creating accumulation space and introducing sea water to this passive margin basin

(Goldhammer, 1998). The Sabine uplift area did not subside during the Jurassic, which makes itself a relatively high land in the middle of the basin. Haynesville sediments were deposited along the east and west flanks of the uplift forming two depocenters. The Haynesville Shale is at least partially time equivalent to the carbonate-rich Gilmer and Haynesville Lime members of the Haynesville Formation. However, the lithology of the overall Haynesville Formation includes carbonates, siliciclastic, and to a lesser extent evaporates. The lithological variation is related to the shifting of depositional environments (Adams, 2009; Ewing, 2009; Hammes et al., 2011). In northeast Louisiana and western Mississippi, a siliciclastic input from the ancestral Mississippi river was dominant (Cicero and Steinhoff, 2013), whereas in east Texas, Gilmer/Haynesville lime carbonate production was dominant, fringing the Haynesville Shale to the west and south (Cicero and Steinhoff, 2013). In the whole area, the organisms present are mostly plankton, shallow water benthic dwellers, swimming bottom-dwellers, and algae. Foraminifera, radiolaria, ammonites, pelecypods and sponge spicules have been reported in the core and thin section scales (Hammes et al., 2011). Overall, the Late Jurassic was one of the best times for the formation of organic-rich source rocks (Klemme, 1994).

During most of the Early Cretaceous, sediment deposition in the northern Gulf of Mexico Basin occurred on a shallow reef-rimmed carbonate platform (McFarlan and Menes, 1991; Scott, 1993), known as the Maverick Basin area of south Texas (Figure 1). During Pearsall deposition, the carbonate shelf environment was flooded by a regional transgression, and as a result terrestrially-sourced sediments comprise a higher proportion of the rock record than the underlying and overlying carbonate-rich units. No evidence exists for an Early Cretaceous shelf-edge barrier reef during Pearsall deposition; water depths at the underlying Sligo shelf margin were too high for shoal water deposition or reef buildup to occur (Loucks, 2002).

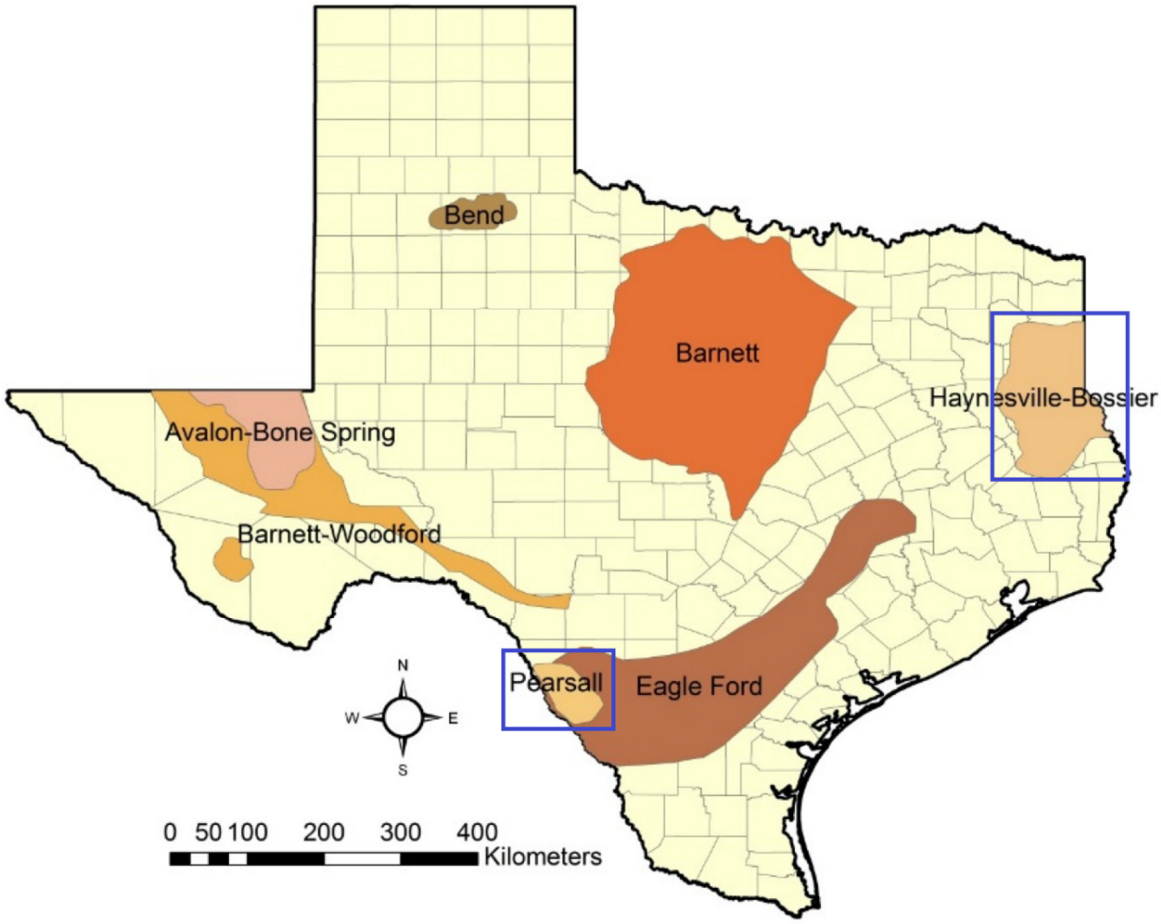

Fig. 1: Several shale plays in Texas with the blue color boxes showing Haynesville-Bossier and Pearsall shales (US EIA, 2012)

3. Materials and methods

3.1. Samples

This work focuses on the detailed study of eight shale samples selected to cover a broad range in mineralogy, total organic carbon (TOC) and porosity. Five samples are from Haynesville Shale formation collected from Huffmann#1 well drilled by NRF Energy in Harrison Co., TX, and the other three samples from the Pearsall shale come from the Tidewater Wilson well located in La Salle Co., TX. The range in TOC, maturity, mineralogy and grain size enables us to study the controls of these parameters on the porosity distribution in the shales.

3.2. Pyrolysis and organic richness

Pyrolysis equipment and its operations, measured parameters, potential pitfalls, and applications to petroleum exploration have been described in detail previously (Behar and Peletet., 1985; Espitalie´ 1986; Peters and Cassa, 1994; Lafargue et al., 1998). The powdered shale sample fractions (< 75 μm) were used to determine TOC using both Shimadzu TOC–VWS wet chemical total organic carbon analyzer and a Leco CS-200 carbon/sulfur analyzer. The pyrolysis on < 75 μm samples was performed on an OCE-II oil–gas evaluation workstation following Chinese Technical Standard GB/T 18602-2012 (SAC, 2012). The OCE-II apparatus performs temperature–programmed heating to (1) thermally distil ‘‘free’’ or adsorbed hydrocarbons (S1 peak) from the sample, (2) pyrolyze the kerogen to produce hydrocarbons (S2 peak) in a second oven, and (3) residual organic carbon content in mg/g (S4 unit mass) of hydrocarbon source rock after pyrolysis. This instrument is not equipped with the S3 measurement unit which can detect the unit mass of released carbon dioxide (mg/g) which is generated during the thermal breakdown of kerogen in source rocks. The T_{max} is estimated based on the S2 peak temperature that coincides with the maximum generation of hydrocarbons. The equivalent vitrinite reflectance is deduced from T_{max} (°C) using the following equation from (Jarvie, 2012): $VR_e\% = [0.018 \times T_{max}] - 7.16$. The total hydrocarbon potential of the sample is defined by (S1+S2), the hydrogen index (HI) = 100*S2/TOC, and Production Index (PI) = S1 / (S1+S2). Other parameters obtainable from pyrolysis are the bitumen index (BI), defined as S1/TOC (Killops et al., 1998), and the quality index (QI) ~ (S1+S2)/TOC.

3.3. Low-pressure N_2 physisorption isotherm

Low-pressure nitrogen (N_2) physisorption analysis has been proven to be an effective method in characterizing pore structures, such as pore volume, specific surface area, and pore size distribution (PSD) in tight reservoirs (Chen et al., 2011; 2016; Clarkson et al., 2013; Labani et al., 2013; Mastalerz et al., 2013) and resulting data indicate that the shale has fractal geometries (Yao et al., 2008; Yang et al., 2016).

Using an Autosorb IQ apparatus of Quantachrome Instruments, this method relies on physical adsorption of N_2 gas at a constant temperature of 77.35 K (-196.15 °C) controlled by liquid nitrogen, at a relative pressure (P/Po) in the range 0.001 to slightly less than 1.0 for nitrogen gas, where P and Po represent balance pressure and saturation pressure respectively for the adsorption and desorption isotherms (Kuila et al., 2014; Mendhe et al., 2015; Quantachrome Instruments, 2015; Li et al., 2016; Mishra et al., 2018). Isotherms are produced as the quantity of N_2 adsorbed under different relative pressures is recorded. The shape of the isotherm and the hysteresis pattern are used to qualitatively predict the type of pores. Specific surface area (m^2/g) is obtained by the Brunauer-Emmett-Teller (BET) method (Brunauer et al., 1940) which is based on the adsorption theory of multimolecular layers. Pore size distribution (PSD) and volume were derived by Dollimore-Heal (1964) (DH) and Barrett-Joyner-Halenda (BJH) methods (Barrrett et al., 1951). Gregg and Sing (1991) used both methodologies to calculate pore size assuming cylindrical shaped pores based on the thickness of the adsorbed layer and the Kelvin equation. The measurement range for PSD is approximately 3.1 to 220 nm for the BJH method.

3.4. Fractal dimension theory

Irregular and fragmental length scales, defined as fractal geometry, can be applied to the understanding of natural porous media (Mandelbrot, 1983; Mahamud and Novo, 2008; Yang et

al., 2016). Several approaches and representations, such as fractal Frenkel-Halsey-Hill (FHH) model (Jaroniec, 1995), thermodynamic method (Neĭmark, 1990), fractal BET model (Brunauer et al., 1938; Avnir and Jaroniec, 1989) have been used to determine fractal dimensions for many porous materials, based on results from small angle X-ray scattering (Jaroniec, 1995), MIP (Bernal and Bello, 2001) and image analysis (Krohn, 1988; Dathe et al., 2001). All of these methods have distinct disadvantages and advantages. Nonetheless, based on gas adsorption isotherms, the fractal FHH model has been demonstrated to be an effective technique and is commonly used for various porous materials (Ismail and Pfeifer, 1994; Tatlier and Erdem-Senatalar, 1999; Yang et al., 2014). Based on the FHH model, the equation is represented as ln (V/Vo) = constant + K[ln(ln(Po/P))], where P is the equilibrium pressure, adsorbed gas molecular volume V, monolayer coverage volume Vo, saturation pressure Po, and constant K is associated with the fractal dimension which can be gained by the slope of the plot of lnV vs. ln(ln(P/Po).

Then the fractal dimension (D) can be determined using the equation of D = K+3. Jaroniec (1995) showed that the value of fractal dimension D usually varies from 2 to 3 which is strongly influenced by the geometrical irregularities and roughness of the pore surface; more complex and irregular pore surfaces will have D values approaching 3.

3.5. Water immersion porosimetry (WIP)

WIP after vacuum saturation is a fundamental method for porosity measurement of geologic media. The vacuum saturation setup consists of a sample chamber connected to a vacuum pump (Varian SD-90) and a compressed gas (CO_2) cylinder, as well as a reservoir of saturating fluid. The goal is to evacuate the sample chamber, and thus the pores connected to the edge of the

sample inside the chamber, after pulling a vacuum to about 0.07 torr (99.993% vacuum, as indicated from 0.01-20 torr Cole-Parmer Pressure/Vacuum Meter for Pirani-Type Sensor). This is then followed with a cycle of CO_2 flushing and vacuum pulling as CO_2 is better dissolved in DI water than air. Next a saturating fluid (cooled boiled DI water) is introduced to the chamber until the samples are immersed under the liquid to occupy the evacuated pore space. After immersion, pressurized CO_2 at 50 psi was applied to the liquid, further driving the fluid into the pores. By weighing the samples before and after saturation, the total mass of fluid saturating the samples is obtained and used to calculate accessible pore volume.

3.6. Mercury intrusion porosimetry (MIP)

Utilizing a mercury intrusion porosimeter AutoPore IV 9510 machine (Micromeritics Instrument Corporation), MIP analyses were conducted to directly measure the porosity, total pore surface area, particle density, bulk density, and pore-throat size distribution of porous media (Webb, 2001; Gao and Hu, 2013; Hu et al., 2018). Because of its high surface energy and nonwetting characteristics, liquid mercury is used for occupying a certain pore throat size for any geological material, when the penetration only occurs under external pressure . Mercury invades the pores due to the pressurization, and the smaller the pores, the higher the pressure required to force the mercury in. Washburn (1921) assumed that the pores are cylindrical, in order to allow the determination of pore throat diameters based on applied mercury pressures. In addition to direct measurement of different properties, permeability (Katz and Thompson, 1986; 1987; Gao and Hu, 2013) and tortuosity (Hager, 1998; Webb, 2001; Hu et al., 2015) are indirectly estimated by MIP method.

For MIP tests, a cube-sized shale sample (linear dimension of each side = 10-11 mm) was placed in an oven at 60ºC for at least two days to remove moisture. Then the sample was kept in a desiccator with less than 10% relative humidity at room temperature (23ºC) to cool. At the beginning of the MICP test, the pore space of air/gas of the samples was evacuated to 50 µm Hg pressure (6.7 Pa or 99.993% vacuum). Experiments were conducted atthe low-pressure condition, and then at high pressure up to 413 MPa or 60,000 psi. The pore throat diameter was 2.8 nm at a high pressure of 60,000 psi using the corrected Washburn equation (Wang et al., 2016). A penetrometer (narrow bore sample holder) for samples less than 3% porosity recorded the largest pore-throat size of 50 µm under low-pressure MICP analysis, while another penetrometer for 3-15% porosity samples had a detectable pore throat diameter of about 1000 µm. At the time of the high-pressure test, the equilibration time [time for pressure proceeding from one step to another pressure level (with a detectable mercury volume change o0.1 µL for each step) was selected as 45 sec.

3.7. Spontaneous fluid imbibition

Spontaneous imbibition apparatus was described by Gao and Hu (2012) and Kibria et al., 2018, using a semi-microbalance at 0.01 mg resolution (Model AUW220D, Shimadzu). Hu et al. (2001) expressed in detail the apparatus set up, operation and data analysis. Because of the importance of imbibition, a large amount of research has been conducted to study the imbibition of reservoir rocks (Hu et al., 2001; Li, 2007; Takahashi and Kovscek, 2010; Graue and Fernø, 2011; Shahri et al., 2012; Kibria et al., 2018). Imbibition-derived pore connectivity for a sample from the slope of log-imbibed fluid mass vs. log time (Ewing and Horton, 2002; Hu et al., 2012). Different depth core plug samples were cut as cubic or rectangular prisms; then four of the sample's sides were painted with a quick-cure epoxy thin layer, leaving the bottom and top faces

unpainted, to produce one directional imbibition process by displacing air in pore space with imbibed fluid in the same direction. To remove any moisture from the samples, all samples were dried in an oven at 60±2°C for a minimum of two days, and then kept below 10% humidity in a desiccator and allowed to cool before the test. In this work, both deionized water and n-decane were used as the imbibing liquid to displace air from pore spaces. Sample weight changes over time were automatically recorded, and fluid mass imbibed within samples was considered after adjusting the buoyancy and evaporation losses (Hu et al., 2001). Each imbibition test ran for approximately 8-9 hrs before the sample was detached from its fluid contact. Triplicate water imbibition experiments, using the same cubic sample after re-drying for at least 48 hrs, were conducted to evaluate the reproducibility of water imbibition. Cumulative imbibition height vs. imbibition time was plotted on log-log coordinates. Hu et al. (2012) reported three types of imbibition slope for different rocks, with values of 0.5, 0.26, and 0.26 transitioning to 0.5. Theoretical values from percolation theory support that the higher slope values are a representation of good pore connectivity and lower slope values are a sign of low pore connectivity of porous media (Stauffer and Aharony, 1994; Ewing and Horton, 2002; Hunt et al., 2014).

3.8. Contact angle measurement

Studying the wettability of tight rock surfaces is essential to understanding the gas flow and the flow-back behavior of fracking fluids in tight rock formations (Fernø et al., 2011). The reservoir can be permanently damaged due to an incorrect evaluation of wettability (Sulucarnain et al., 2012; Singh, 2016). Wettability can be directly measured by the contact angle of diverse fluids on a rock surface and by qualitative drop tests.

The contact angle was measured on polished shale samples using a contact angle meter and interface tensiometer (Model SL200K, Kino). Samples for contact angle measurements were processed by first dry-cutting the core into appropriate dimensions (10 mm wide × 10 mm long x 3 mm tall) using a circular saw. After that, the samples were polished using 240-grit sandpaper. Contact angle measurements were performed for different hydrophilic and hydrophobic fluids, including deionized water (DI water), API brine (8% NaCl and 2% $CaCl_2$ by weight), 20% IPA (isopropyl alcohol) in DI water, and n-decane (representative of an oil phase) (Yang et al., 2017). A droplet of each fluid at 2 μL was placed onto the sample surface, and an image of the air-liquid-solid interface was captured to calculate contact angle using CAST™2.0 software.

4. Results and discussion

4.1. Pyrolysis and organic richness

The Haynesville Shale samples (H-10979, H-11071, H-11122, H-11178, H11226; Table 1) include mainly two types of samples, siliciclastic and carbonate based. Sample H-10979 has more than 60 wt.% clay minerals whereas H-11178 has mainly quartz and feldspar. The remaining Haynesville samples (H-11071, H-11122, and H-11226) have more than 45% carbonate minerals. Pearsall shale sample P-11771 has more than 50 wt.% quartz and feldspar and 10 wt.% clay minerals. The other two Pearsall samples TW-11842 and TW-11926 have more than 70% calcite minerals (Table 1). The TOC value ranges between 0.85–3.91 wt.% (Table 1), All Haynesville shale has a higher amount of TOC value which is above 3.1%.

Table 1: Mineralogy and TOC of the Haynesville and Pearsall Shale samples.

Sample ID	QFM			Sulfide		Carbonate			clay		TOC
	Quartz	Albite	Enstatite	Musovite	Pyrite	Calcite	Ankerite	Dolomite	Illite	others clay	
H-10979	12	3.4		4.9	1.5	15.5		1.3	8.6	52.8	3.51
H-11071	23.5	8.2	1.5	14.4	4	38.6			7.2	2.6	3.59
H-11122	21.6	6.8		11.7	3.4	33.2	3.8	1.2	8.5	5.8	3.87
H-11178	35.7	12	2.3	7.8	2.2	18			15.7	6.4	3.76
H-11226	5.9		3.3			16.5	6.1	62	4.3	1.9	3.09
TW-11771	46.6	5.7			5.7	21.5	7		11.5	1.9	0.85
TW-11842	8.8			2.8	1.6	77.7				9.1	3.91
TW-11926	21.2	2		3.9	2	67.1			3.3	0.5	1.39

Table 1 and 2 shows the values of TOC, S1, S2, kerogen type, and T_{max}, as well as calculated results of HI, and PI, from pyrolysis analyses of 8 samples. S1 values are between 0.20 – 1.56 mg HC/g rock and S2 values around 0.27–2.02 mg HC/g rock (Table 2). The Hydrogen index (HI) of these samples are between 12.11–59.28 mg HC/g TOC. Vitrinite reflectance equivalence from T_{max} is estimated as 0.98 to 0.3.24 VR_e% (Table 2). Calculated PI values are in the range 0.28 – 0.51. Based on the pyrolysis data, all of these eight samples of Haynesville and Pearsall Shales are main types III and IV kerogens.

Table 2: Geochemical characteristics of Haynesville and Pearsall shale derived from pyrolysis method.

Sample	Depth (ft)	S1	S2	Tmax(°C)	%VR_e	% Ro	HI	PI	Type
H-10979	10979	0.53	0.51	476	1.41		21.07	0.51	IV
H-11071	11071	0.18	0.44	461	1.14		13.25	0.29	IV
H-11122	11122	0.24	0.63	523	2.25		14.48	0.28	IV
H-11178	11178	0.33	0.75	578	3.24		14.42	0.31	IV
H-11226	11226	0.2	0.27	491	1.68	1.36	12.11	0.43	IV
TW-11771	11771	0.44	0.46	452	0.98	1.57	42.20	0.49	IV
TW-11842	11842	1.56	2.02	460	1.12		53.87	0.44	III
TW-11926	11926	1.02	1.15	462	1.16		59.28	0.47	III

4.2. Analysis of N_2 physisorption

4.2.1. N_2 adsorption/desorption curves

In this work, the IUPAC classification was used for categorizing pore throat width (IUPAC, 1994): it defines pores greater than 50 nm as macropores, pores in the range of 2 to 50 nm are called mesopores and pores less than 2 nm are micropores. According to the Brunauer, Deming, and Teller classification (Brunauer et al., 1940), reversed S-shaped N_2 adsorption isotherms are type II. Type II isotherms demonstrate that micropores and mesopores are dominant. In Figure 2, five samples of N_2 adsorption isotherms show that all samples have type II isotherms.

Based on the high amount of adsorption at low relative pressure (<0.5) (fig. 2), it is assumed that the monomolecular layer of adsorption is transitioning to a multi-molecular layer in the microporosity. Overall, all samples exhibit similar isotherm shapes (Fig. 2). Samples H-11122 and H-11178 show different behavior in their desorption. Samples H-11122 and H-11178 have a very similar mineral composition, and all Haynesville samples have similar TOC values (Table 1). Yang et al. (2017) showed that the adsorption volume is controlled by several factors other than TOC content, e.g., the mineral composition. At higher relative pressures greater than 0.95, the adsorption volume increases rapidly. In this higher relative pressure no adsorption saturation occurs. This indicates that there may be some large pores or fractures, of >300 nm, not being detected by N_2 physisorption approach, in these samples.

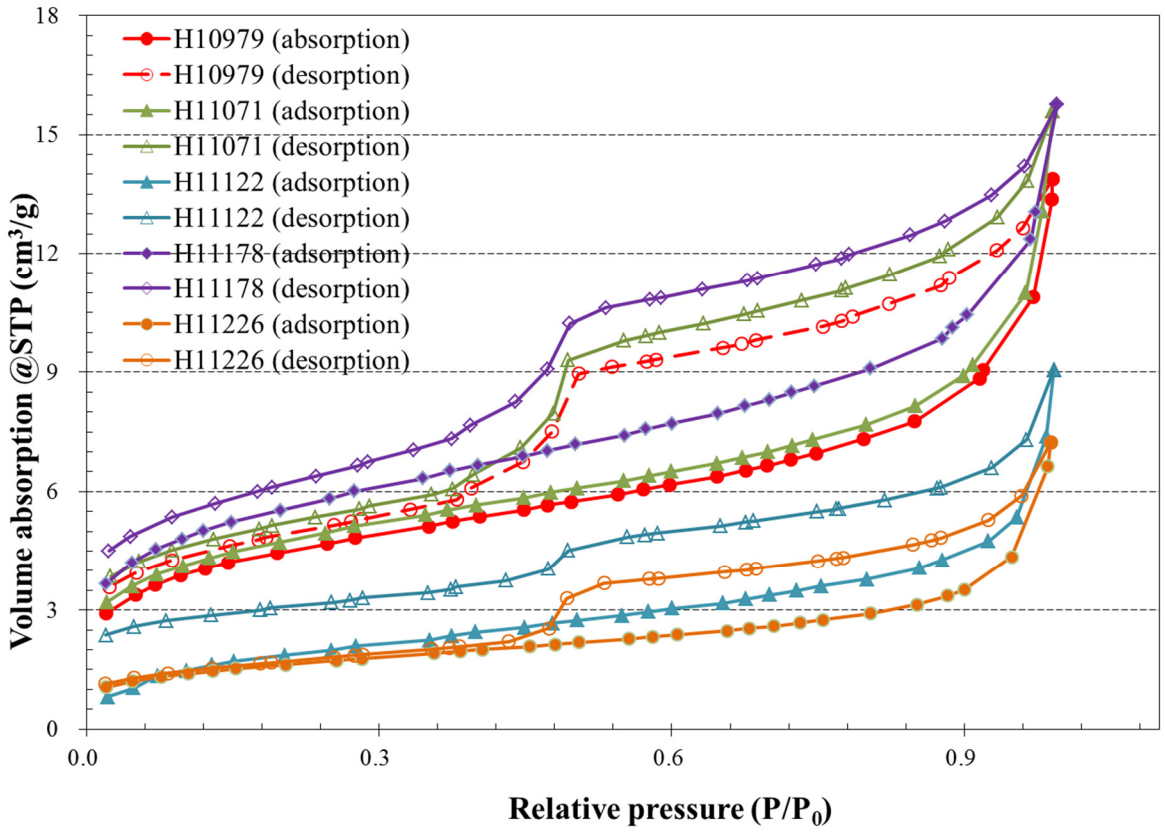

Fig. 2: N_2 adsorption (solid symbols) and desorption (open symbols) isotherms for Haynesville samples.

Figure 2 shows the evident hysteresis for adsorption-desorption isotherms for the examined Haynesville samples, with several explanations being proposed for hysteresis behavior (McGavack and Patrick, 1920; Cohan, 1938; Sing, 1985), for example, capillary condensation in mesoporous structures by Sing (1985). When compared to the different possible shapes of the hysteresis loops, the hysteresis loops of all five samples are classified as H2 type, according to the IUPAC classification. Sing (1985) showed that H2 type of hysteresis loops is mainly linked with "inkbottle" pores (i.e. their shape resembles an old-fashioned ink bottle) and a small number of cylindrical pores or parallel-plates.

4.2.2. Pore-size distribution, pore volume and surface area by N_2 adsorption

Pore size distributions calculated from N_2 adsorption data show that all samples have similar distributions of pore sizes, with the largest peak at approximately 4 nm diameter (Fig. 3a). Over 80% of the total mesopore volumes are contributed by pores with a width less than 40 nm. By enlarging the overlapping area of the distribution (grey box area in Fig. 3a), we can see that all Haynesville samples exhibit tri-modal distributions, at pore widths of approximately 3 nm, 4 nm and 5 nm and a series of small peaks. The TW-11771 sample has double peaks at 2 nm and 3 nm. Because of the limitations of N_2 adsorption, the distribution of pores with a width of less than 2 nm may not be correctly described in Fig. 3a. BET surface areas, obtained from N_2 adsorption analysis, exhibit a wide range of values but a similar distribution character compared with that of pore volume (Fig. 3b). Four Haynesville samples H-10979, H-11071, H-11122, and H-11178, have BET surface area values of 4.42 to 5.93 m^2/g, while the H-11226 sample (mainly a dolomitic limestone) shows a smaller BET surface area of 2.25 m^2/g. Pearsall sample TW-11771 has a low BET surface area of 0.48 m^2/g, with the sample having a lower TOC value of 0.85%. It is clear that the surface area is related to the TOC content and clay mineralogy, indicating that micropores are associated with organic matter and clays. The average BET surface areas of Haynesville and Pearsall shales are smaller than Chinese Longmaxi shale (Yang et al., 2016) and similar to Woodford, other Haynesville samples and Barnett Shales (Clarkson et al., 2013; Liu et al., 2015).

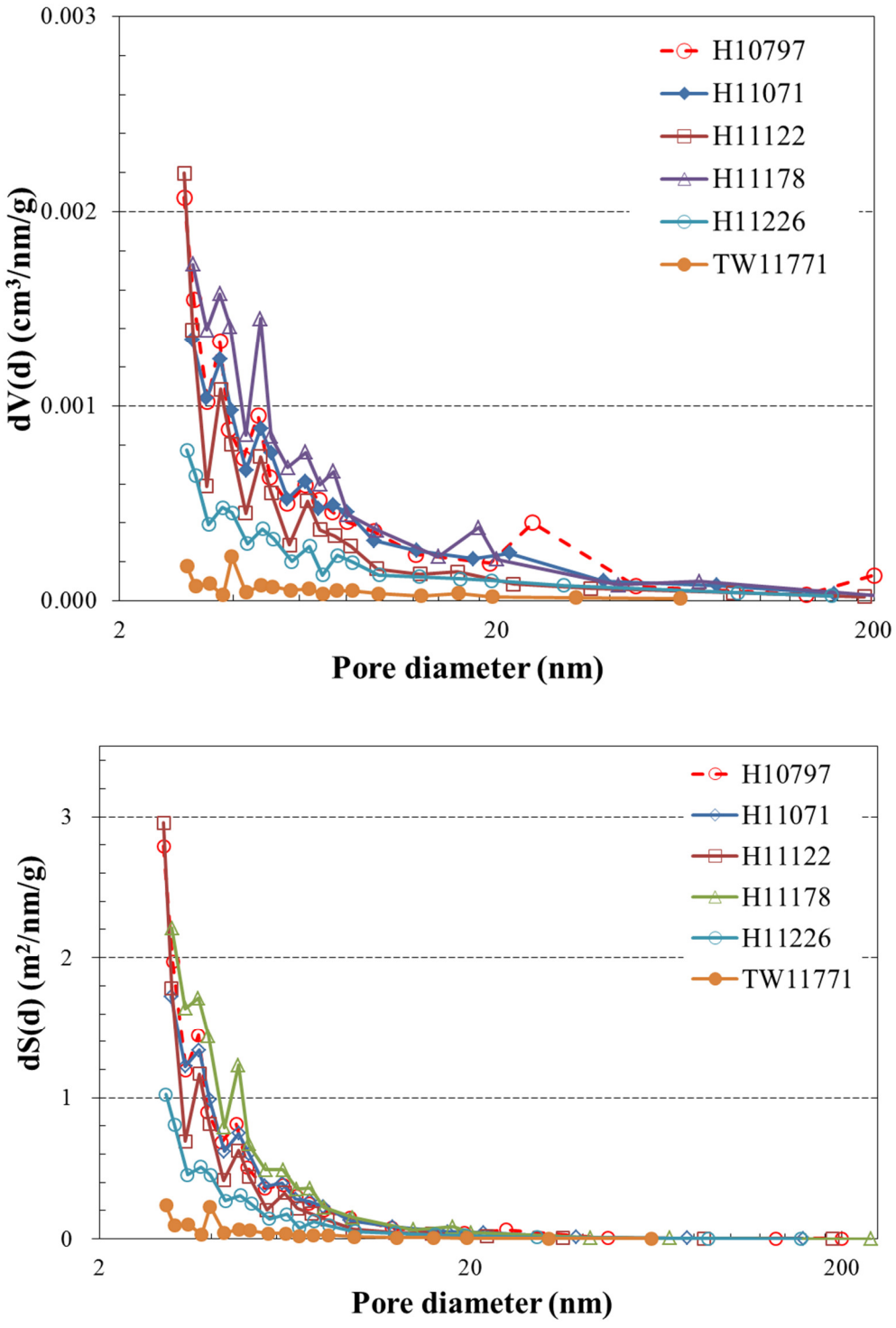

Fig. 3: N_2 adsorption-derived pore size distribution: a) pore volume distribution and b) surface area distribution.

4.2.3. Fractal dimensions from N_2 adsorption isotherms

Figure 4 presents the plots of lnV vs. ln(ln(P/Po)) and calculated fractal dimension results, based on the Frenkel-Halsey-Hill (FHH model). Graphs are separated into two sections of high and low pressures with different gradients, which indicates two different significant phases of N_2 adsorption process (monolayer-multilayer adsorption and pore infilling). Both segments have a good linear relation, with the correlation coefficients above 0.98 and 0.94 for high- and low-pressure segments, respectively. Based on the work of Jaroniec (1995), such results suggest that these samples are fractal. It is also observed that, with the decrease of relative pressure in the low-pressure curve, a few data begin to deviate from the fitted straight line, which is mainly related to the increasing van der Waals force in the micropores. Gregg and Sing (1982) showed that these data also reflect the existence of monolayer adsorption process, which provides the theoretical basis for calculation of surface area in porous media.

The fractal dimension in the high pressure set-up (D1) varies between 2.53 and 2.82, while the fractal dimension in the low pressure (D2) changes from 2.17 to 2.59. From our result we got a higher number than 2 for both D1 and D2. Comparing with the fractal dimensions for different type of lithology and TOC value shows the difference, the fractal dimensions (D1 and D2) for Haynesville shale samples have 2.71-2.82 D1 and 2.23-2.59 for D2, while TW-11771 sample shows D1, 2.53 and D2 2.17, and has a lower TOC (0.85%) and higher amount of silicate minerals.

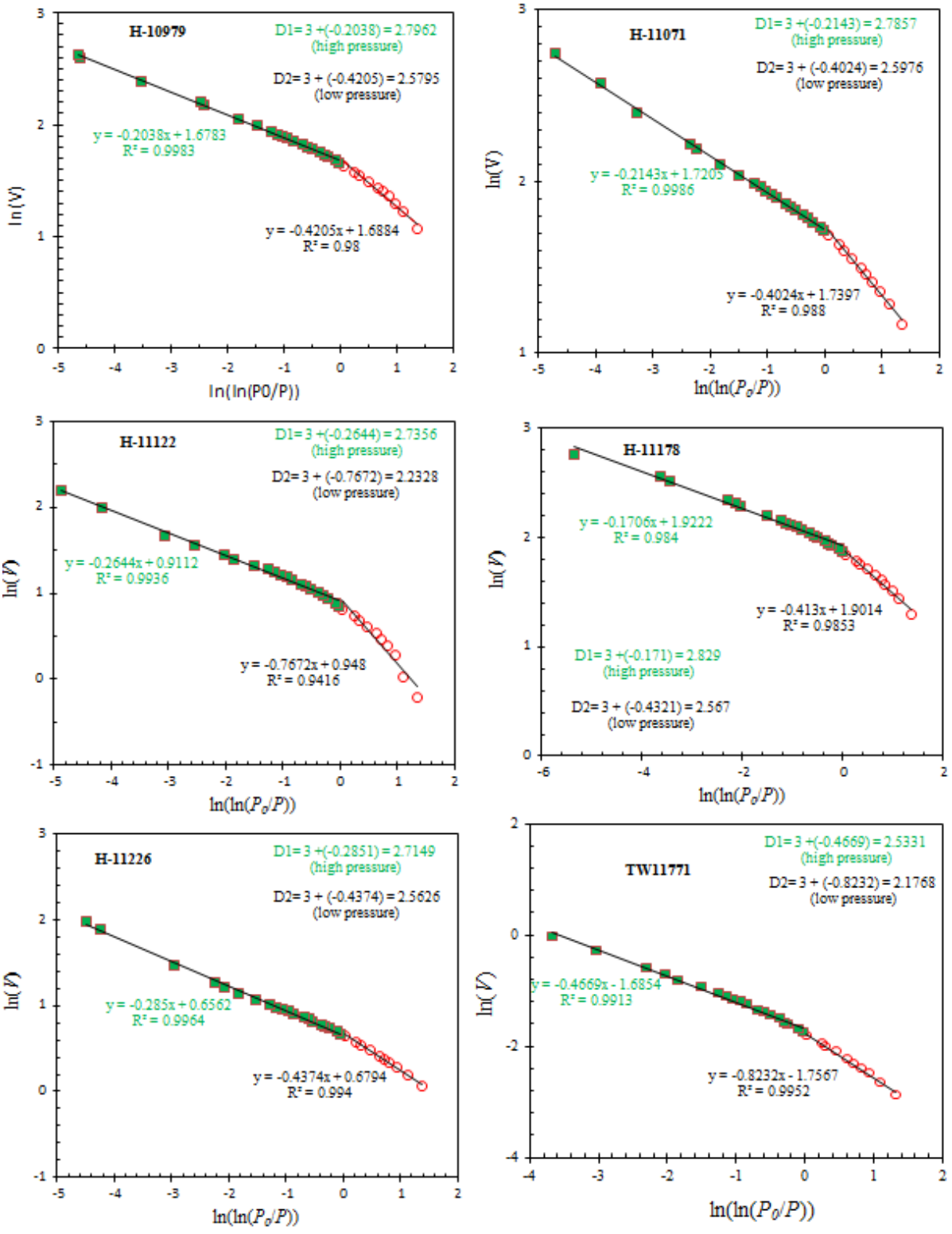

Fig. 4: Fractal dimensions obtained from N_2 adsorption isotherms; R^2 = correlation coefficient.

4.3. Results of MIP tests

MIP based results show that a significant volume of µm-sized pores is present in all eight Haynesville and Pearsall rock samples. The median pore-throat diameter (at 50% by pore volume) shows a variation with sample lithology. The median pore throat diameter for Pearsall shale is 0.46-1.05 µm, and more than 60% pores by volume are above 100 nm in pore-throat diameter (Table 3 and Figure 5). Haynesville samples fall into two categories: i) samples with more than 50% calcite and illite minerals (H-11071 and H-11122) possess more than 50% pores within the 2.8-50 nm pore-throat size range; ii) The other Haynesville samples (H-10979, H-11178, H-11226) have 0.27 to 0.36 µm median pore throat, and more than 65% pores by volume are greater than 100 nm in pore-throat diameter (Figure 5a). Most of the hydrocarbon species in oil/gas exploration have a molecular diameter of 0.5-10 nm (Nelson, 2009). These pore-throat sizes play important roles as the main conduits for hydrocarbon transport at the time of production. Hydrocarbon movement probably occurs mostly within a larger pore network of >5 nm pore-throat size. Therefore the µm size pore-throat diameter at both Haynesville and Pearsall Shales suggest a very good pore network for hydrocarbon movement.

Based on the Katz and Thompson (1986) equation, the MIP-derived permeability of eight samples was calculated. All Haynesville and Pearsall samples (except H11226) have permeability in the range of 0.16 µD to 7.33 µD for the >100 nm pore throat network (Table 3). Haynesville sample H-11226 shows a higher value for permeability of 145 µD, and this sample has a higher amount of dolomite (62%) and TOC (3.09%). 80% of the pores in sample H-11122 have diameters from 2.8 to 50 nm, and this sample also has a high TOC value, high amount of clay and calcite here indicated most of these nanopores are clay palleted and organic matter-hosted pores.

Table 3: MICP analysis-derived pore structure properties for the Haynesville and Pearsall samples.

Sample ID	Total pore area (m^2/g)	Total pore volume (mm^3/g)	Median pore-throat diameter (μm)		Average pore-throat diameter (μm)	Pore-throat diameter %			Predominant (>100 nm) pore-throat network			
			Volume	Area		2.8-50 nm	0.05-0.1 μm	>100 nm	Critical pore-throat diameter (μm)	Permeability k (μD)	Effective tortuosity D0/De	Geometrical tortuosity Le/L
H10979	10.21	0.170	271.14	0.004	0.017	32.57	2.23	65.21	1.14	1.38	1616	14.38
H11071	14.13	0.027	0.23	0.005	0.013	47.38	4.59	48.03	0.95	0.96	1062	8.30
H11122	11.39	0.025	0.01	0.006	0.009	76.27	3.96	19.77	0.97	0.20	86	2.27
H11178	13.43	0.059	364.52	0.005	0.017	32.38	3.15	64.47	2.05	7.33	235	5.78
H11226	12.16	0.025	294.21	0.006	0.025	27.24	0.53	72.23	7.26	145.19	119	3.02
TW11771	0.88	0.010	1.03	0.004	0.017	25.28	10.33	51.61	1.03	0.16	77	0.86
TW11842	0.50	0.003	0.46	0.004	0.020	20.82	9.20	69.98	1.34	0.20	25	0.39
TW11926	0.08	0.001	1.05	0.026	0.100	13.93	9.8	76.30	5.11	1.11	8	0.15

Tortuosity defines the extent of complex passageways for fluid movement within a porous medium (Epstein 1989; Hu and Wang, 2003). Applying Hager's (1998) method to MIP data, the effective tortuosity τ (D_0/De) can be estimated, for the dominant networks controlled by >100 nm pore- throat diameter. The effective tortuosity values for Pearsall Shale are within the range of 8-77, and for Haynesville shale the range is 86-1616 (Table 3). Geometrical tortuosity L_e/L ratios, calculated based on Hu et al. (2015), range within 0.15-0.86 and 2.27-14.4 for Pearsall and Haynesville Shales, respectively (Table 3).

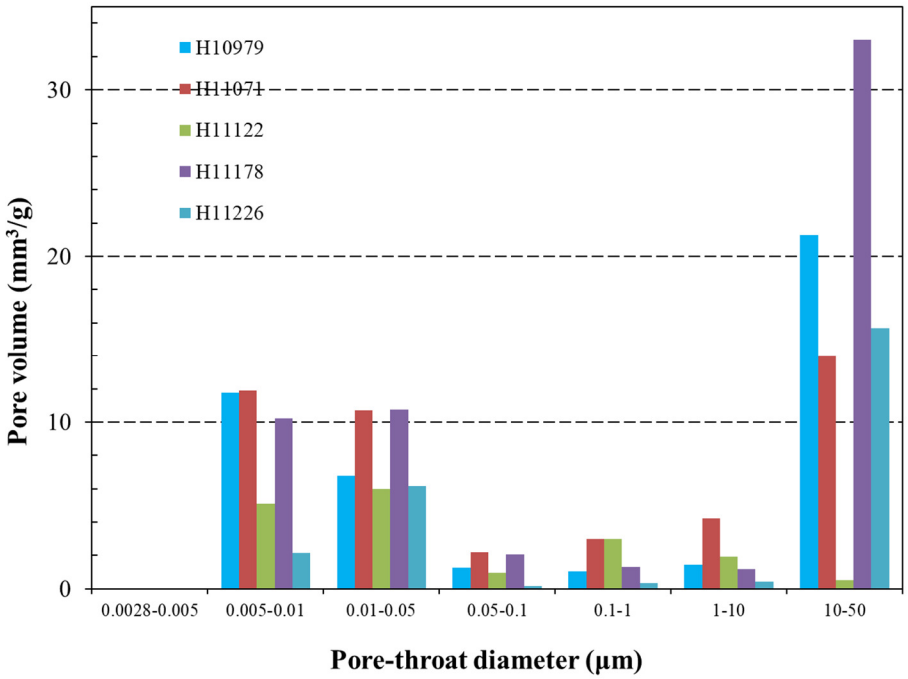

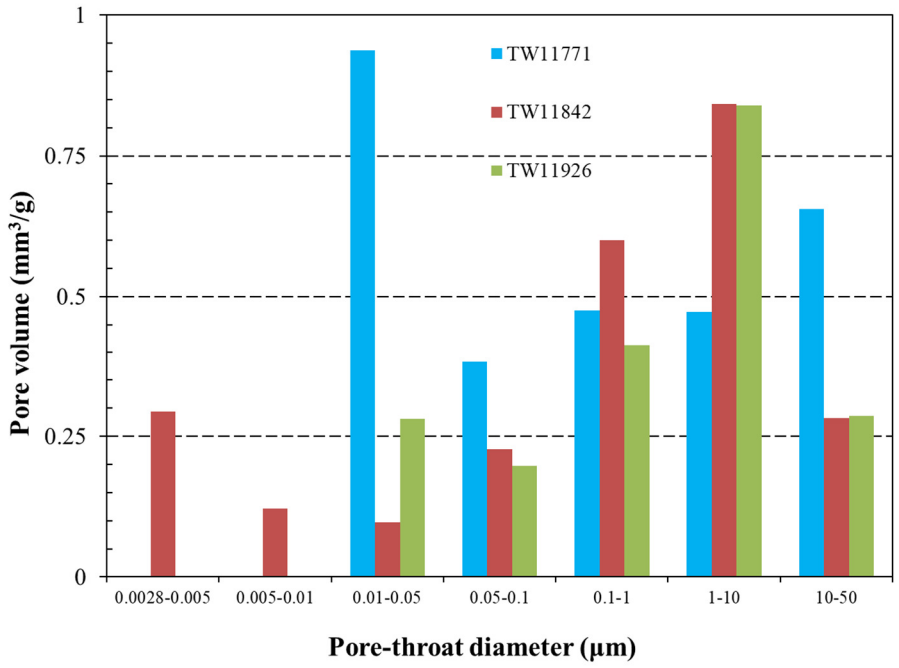

Figure 5: MIP results for pore volume distribution in diverse pore-throat regions for a) Haynesville Shale b) Pearsall Shale rock samples.

4.4. Water immersion porosimetry (WIP)

The bulk density (g/cm^3), grain density (g/cm^3) and porosity (%) values for Haynesville and Pearsall shale samples were obtained using WIP tests. The bulk density and grain density of Haynesville samples are within 2.135- 2.566 and 2.310-2.622 (g/cm^3), respectively. The bulk density and grain density values for cube sizes of Pearsall samples vary from 2.363-2.491 and 2.471-2.549 (g/cm^3) from WIP (Table 4). Bulk density and skeletal density are a little higher from the MIP test. MIP-based bulk and skeletal density are 2.222-2.550 and 2.421-2.723 (g/cm^3) for Haynesville shale. In contrast, Pearsall shale has relatively higher bulk and skeletal densities, which is 2.543-2.591 and 2.559-2.614 (g/cm^3) for MIP. Pearsall shale shows higher bulk and skeletal density because it mainly consists of carbonate minerals. Haynesville and Pearsall shales both give a little higher values for bulk and skeletal density from MICP test because this is automated and machine-generated. Porosity values for Pearsall shale range within 0.52 to 0.88% from MICP (Table 4). Porosity values for Haynesville shale are within the range of 5.96-13.0% from MICP (Table 4). The porosity values for Haynesville and Pearsall shale are higher from WIP tests at 2.147-7.657% and 2.313-3.105%, respectively. Pearsall shale has higher porosity based on the WIP method rather than MICP, for the following reasons. In the MICP test for porosity, mercury is a nonwetting fluid and as a result has to be injected at higher pressure. In contrast, water is a wetting fluid in the WIP test. It is adsorbed more easily within the samples, and these results in increased measured porosity values. Some research has previously shown that the presence of nanopores and reactive clay minerals make precise measurement of porosity in heterogeneous shale samples difficult (Zargari et al., 2014; Klaver et al., 2015; Yang et al., 2016).

Table 4: Bulk density, grain density, and porosity derived from WIP and MIP tests.

Sample name	Vaccum Saturation test			MICP test		
	Bulk density(g/cm3)	Grain density (g/cm3)	Porosity (%)	Bulk density	Skeletal density	Porosity (%)
H-10979	2.297±0.076	2.451±0.074	6.278±0.480	2.320	2.581	10.102
H-11071	2.135±0.241	2.310±0.206	7.657±2.188	2.273	2.421	6.117
H-11122	2.236±0.276	2.360±0.295	5.238±0.131	2.439	2.593	5.965
H-11178	2.235±0.095	2.371±0.088	5.720±0.646	2.222	2.554	13.003
H-11226	2.566±0.106	2.622±0.108	2.147±0.463	2.550	2.723	6.351
TW-11771	2.491±0.087	2.549±0.088	2.313±0.234	2.591	2.614	0.880
TW-11842	2.363±0.121	2.438±0.119	3.105±0.456	2.543	2.559	0.626
TW-11926	2.406±0.155	2.471±0.146	2.651±0.526	2.564	2.571	0.517

4.5. Wettability characteristics

Table 5 shows the contact angle measurements obtained for Haynesville and Pearsall samples using various fluids. DI water and API brine serve as hydrophilic fluids, while n-decane is hydrophobic and 10% IPA mixed with water shows mixed intermediate wettability. N-decane is an organic compound with low viscosity, and 10% IPA chemical also has a similar kind of properties. The contact angles of API for Haynesville samples are in the range 21.05° to 41.74° at 30 s after the droplet meets the sample surface.

Based on contact angle results, it appears that H-10979 and H-11226 samples are more water wetting than others. These two samples mainly consist of clay and dolomite minerals, respectively. The contact angle of n-decane for Haynesville shale samples are between 8.35° and 12.47° at 1 Sec and decreases to <3 degree at 30 sec. Hydrophilic fluid 10% IPA shows a good wettability for two Haynesville sample H-10979 and H-11071, with contact angles of 12.4° and 16.4°, respectively. Haynesville all sample shows an excellent wettability for both hydrophilic fluids (n-decane and 10%IPA). Pearsall Shale samples represent a wide range of contact angles

both for hydrophilic and hydrophobic liquid. For hydrophilic fluids DI water and API brine, the contact angles are 15.64° to 57.82° and 10.47° to 50.9°, respectively. TW-11842 mostly contains calcite minerals (77.7%), and it has a high contact angle for both API brine and DI water, indicating this limestone sample to be poorly hydrophilic. Regardless of the mineralogy of our samples, oil-wetting fluid n-decane and 10% IPA gave relatively low contact angle. n-decane and 10% IPA can access all oil-wetting pores and observe high wettability behavior.

Table 5: Contact angle (in degrees) (at 30 s after droplet contact) and slope values from spontaneous imbibition experiments.

	Contact Angle				DI imbibition
sample ID	DI water	API brine	10% IPA	n-decane	Slop
H10979		28.05	12.4	10.7	0.435
H11071		36.8	16.4	11.25	0.211
H11122		41.74		12.47	0.280
H11178		40.63		9.93	0.234
H11226		21.05		8.35	0.339
TW 11771	25.77	31.05	21.85	9.25	0.440
TW 11842	57.82	50.9	15.46	8.17	0.255
TW 11926	15.64	10.47	4.52	32.78	0.407

4.6. Spontaneous imbibition

In general, low-connectivity porous media show a characteristic imbibition slope of ½ using classical Fickian behavior (Hu et al., 2015; Gao and Hu, 2016). Hu et al. (2012) showed that when a porous surface area increasingly gains moisture in a Fickian manner, Indiana sandstone showed 0.25 slope value and Berea sandstone 0.5; slope values around 0.25 indicate sparsely connected pores, 0.25 to 0.50 moderately connected pores, and > 0.5 indicates well-connected pores. Table 6 presents the spontaneous imbibition results for Haynesville and Pearsall samples.

Sample H-10979 is used as an exemplary DI water imbibition curve. The slope of the first straight line fit for DI water is 1.36, which generally indicates a steep and noisy line up to the 30-sec mark; this is caused by the sample settling from initial contact with the DI water. In Fig. 6, the 2nd slope value is 0.276, which represent that sparse connectivity of side pores and initial suction of water within the time interval of 30sec to 60 min. The sample's internal connectivity over a long duration of 1-6 hrs (the 3rd slope) has a slope of 0.435. This value demonstrates that internal pores are moderately connected. Our DI water imbibition for all Haynesville and Pearsall shale has slopes between 0.211 to 0.435 and 0.255 to 0.407, respectively.

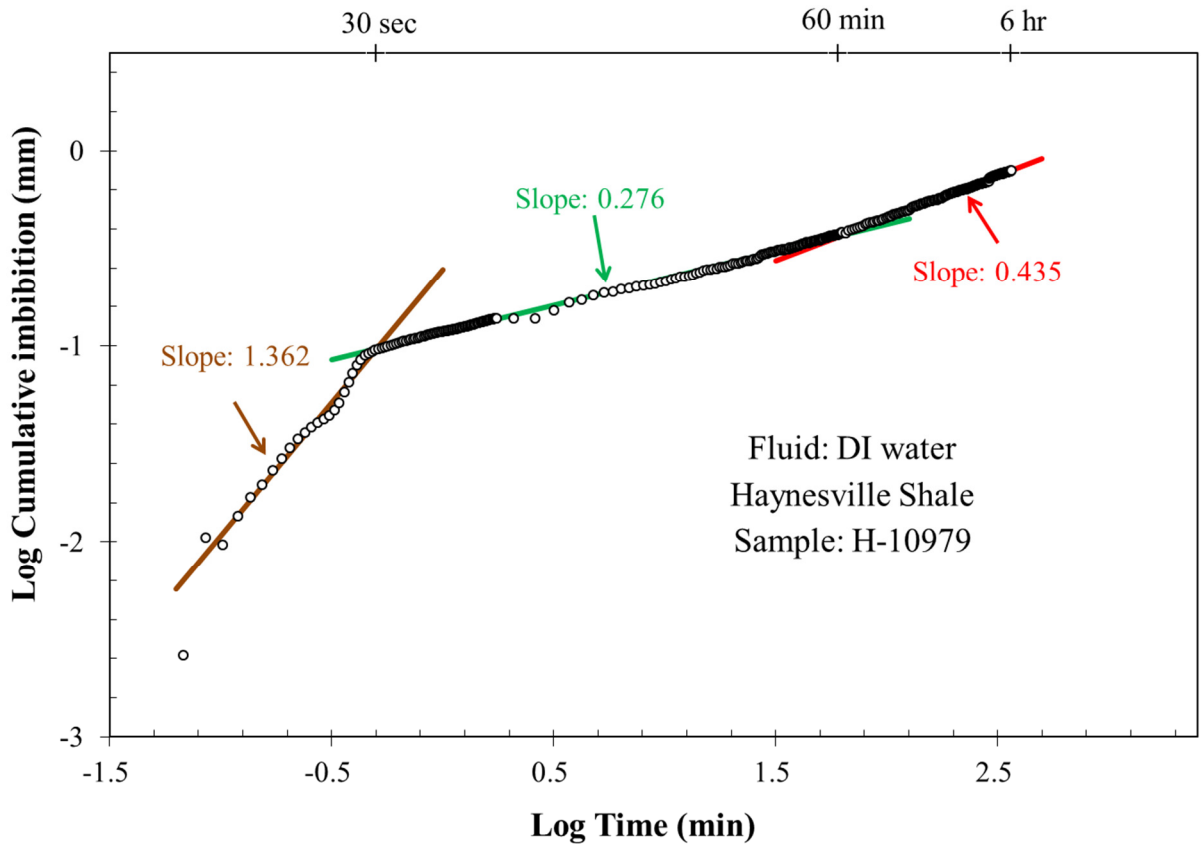

Figure 6: Log cumulative imbibition (mm) vs. Log time (min) for a sample of H-10979 for DI water.

5. Conclusion

Low-pressure N_2 gas adsorption, high-pressure mercury intrusion and vacuum saturation tests on a suite of Haynesville and Pearsall Shale samples reveal differences in pore structure and wettability characteristics, which affect both gas storage and transport properties. Samples with higher amounts of clay and quartz+feldspar contain mainly nanopores, and these also have higher TOC values. Carbonate-dominated samples show low pore volumes, as observed by both MICP and N_2 absorption tests. Porosity and permeability estimates were successfully obtained for Haynesville and Pearsall shale sample from MICP and WIP. Experimental data demonstrate that clay and quartz+feldspar-based samples have mainly nanometer size pore throat diameters, whereas carbonate-based lithology has micrometer size pore throat diameters. Pearsall Shale samples have a very low pore volume, which means it can hold only a small amount of in-place hydrocarbon within the formation. Both Haynesville and Pearsall Shales have substantial differences in BET surface area from nitrogen isotherm results. Similar lithology shows a similar amount of value from all experiment-based porosity data. Pearsall and Haynesville samples show complex fractal dimension behavior of pores which is mainly associated with nanopores less 30 nm. Mostly clay and quartz+feldspar samples have good pore connectivity for hydrophilic fluid, but moderate to sparse connection for a hydrophobic liquid.

Acknowledgments:

This research was partially supported by the Graduate Student Research Grants from the Gulf Coast Association of Geological Societies (GCAGS) and Southwest Section of American Association of Petroleum Geologist (AAPG), by the University of Texas at Arlington. We are

grateful to Harry Rowe, Robert Villegas, Jordan Bevers, Paul Huggins, Marvin Dunbar, and Scott Leaseburge for their assistance in sample procurement.

Reference

Anovitz, L.M., Cole, D.R., Sheets, J.M., Swift, A., Elston, H.W., Welch, S., Chipera, S.J., Littrell, K.C., Mildner, D.F.R. and Wasbrough, M.J., 2015. Effects of maturation on multiscale (nanometer to millimeter) porosity in the Eagle Ford Shale. Interpretation, 3(3), pp.SU59-SU70.

Avnir, D. and Jaroniec, M., 1989. An isotherm equation for adsorption on fractal surfaces of heterogeneous porous materials. Langmuir, 5(6), pp.1431-1433.

Barrett, E.P., Joyner, L.G. and Halenda, P.P., 1951. The determination of pore volume and area distributions in porous substances. I. Computations from nitrogen isotherms. Journal of the American Chemical society, 73(1), pp.373-380.

Behar, F. and Pelet, R., 1985. Pyrolysis-gas chromatography applied to organic geochemistry:

Bernal, J.L.P. and Bello, M.A., 2001. Fractal geometry and mercury porosimetry: comparison and application of proposed models on building stones. Applied Surface Science, 185(1-2), pp.99-107.

Brunauer, S., Deming, L.S., Deming, W.E. and Teller, E., 1940. On a theory of the van der Waals adsorption of gases. Journal of the American Chemical society, 62(7), pp.1723-1732.

Chen, S., Han, Y., Fu, C., Zhu, Y. and Zuo, Z., 2016. Micro and nano-size pores of clay minerals in shale reservoirs: Implication for the accumulation of shale gas. Sedimentary geology, 342, pp.180-190.

Chen, S., Zhu, Y., Qin, Y., Wang, H., Liu, H. and Fang, J., 2014. Reservoir evaluation of the Lower Silurian Longmaxi Formation shale gas in the southern Sichuan Basin of China. Marine and Petroleum Geology, 57, pp.619-630.

Cicero, A. D., & Steinhoff, I. (2013). Sequence stratigraphy and depositional environments of the Haynesville and Bossier Shales, East Texas and North Louisiana. In AAPG Memoir 105 (pp. 25–46).

Clarkson, C.R., Solano, N., Bustin, R.M., Bustin, A.M.M., Chalmers, G.R.L., He, L., Melnichenko, Y.B., Radliński, A.P. and Blach, T.P., 2013. Pore structure characterization of North American shale gas reservoirs using USANS/SANS, gas adsorption, and mercury intrusion. Fuel, 103, pp.606-616.

Dehghanpour, H., Lan, Q., Saeed, Y., Fei, H. and Qi, Z., 2013. Spontaneous imbibition of brine and oil in gas shales: Effect of water adsorption and resulting microfractures. Energy & Fuels, 27(6), pp.3039-3049.

Dehghanpour, H., Zubair, H.A., Chhabra, A. and Ullah, A., 2012. Liquid intake of organic shales. Energy & Fuels, 26(9), pp.5750-5758.

Dollimore, D. and Heal, G.R., 1964. An improved method for the calculation of pore size distribution from adsorption data. Journal of Applied Chemistry, 14(3), pp.109-114.

Epstein, N., 1989. On tortuosity and the tortuosity factor in flow and diffusion through porous media. Chemical Engineering Science, 44(3), 777–779.

Espitalié, J., 1986. Use of Tmax as a maturation index for different types of organic matter.

Ewing, R.P. and Horton, R., 2002. Diffusion in sparsely connected pore spaces: Temporal and spatial scaling. Water Resources Research, 38(12), DOI: 10.1029/2002WR001412.

Ewing, T. E. (2009). The ups and downs of the Sabine Uplift and the Northern Gulf of Mexico

Fernø, M.A., Haugen, Å. and Graue, A., 2011. Wettability effects on the matrix–fracture fluid transfer in fractured carbonate rocks. Journal of Petroleum Science and Engineering, 77(1), 146–153.

Fick, A., 1855. V. On liquid diffusion. Philosophical Magazine Series 4, 10(63), pp.30-39.

Fu, H., Wang, X., Zhang, L., Gao, R., Li, Z., Xu, T., Zhu, X., Xu, W. and Li, Q., 2015. Investigation of the factors that control the development of pore structure in lacustrine shale: A case study of block X in the Ordos Basin, China. Journal of Natural Gas Science and Engineering, 26, pp.1422-1432.

Galloway, W. E. (2008). Chapter 15 Depositional evolution of the Gulf of Mexico sedimentary

Gao, Z.Y., and Hu, Q.H., 2013. Estimating permeability using median pore-throat radius obtained from mercury intrusion porosimetry. Journal of Geophysical Engineering, 10, 025014.

Gao, Z.Y., and Hu, Q.H., 2016. Wettability of Mississippian Barnett Shale samples at different depths: Investigations from directional spontaneous imbibition. AAPG Bulletin, 100(1), 101–114.

Ghanbari, E. and Dehghanpour, H., 2015. Impact of rock fabric on water imbibition and salt diffusion in gas shales. International Journal of Coal Geology, 138, 55–67.

Ground Water Protection Council. (2009). Modern shale gas development in the United States: A 90 Primer. https://energy.gov/sites/prod/files/2013/03/f0/ShaleGasPrimer_Online_4-2009.pdf

Hager, J., 1998. Steam drying of porous media. Ph.D. thesis, Department of Chemical Engineering, Lund University, Sweden.

Handy, L.L., 1960. Determination of effective capillary pressures for porous media from imbibition data. Trans. AIME 219, 75-80.

Hu, Q.H., and Wang, J.S.Y., 2003. Aqueous-phase diffusion in unsaturated geological media: A review. Critical Reviews in Environmental Science and Technology, 33(3), 275–297.

Hu, Q.H., Ewing, R.P. and Rowe, H.D., 2015. Low nanopore connectivity limits gas production in Barnett formation. Journal of Geophysical Research: Solid Earth, 120(12), 8073–8087.

Hu, Q.H., Ewing, R.P., and Dultz, S., 2012. Pore connectivity in natural rock. Journal of Contaminant Hydrology, 133, 76–83.

Hu, Q.H., Liu, H., Yang, R., Zhang, Y.X., Kibria, G., Sahi, S., Alatrash, N., MacDonnell, F.M. and Chen, W., 2017. Applying molecular and nanoparticle tracers to study wettability and

connectivity of Longmaxi Formation in Southern China. Journal of Nanoscience and Nanotechnology, 17(9),6284–6295.

Hu,Q.H., Persoff, P., and Wang, J.S.Y., 2001. Laboratory measurement of water imbibition into low-permeability welded tuff. Journal of Hydrology, 242, 64–78.

Huang, X. and Zhao, Y.P., 2017. Characterization of pore structure, gas adsorption, and spontaneous imbibition in shale gas reservoirs. Journal of Petroleum Science and Engineering, 159, pp.197-204.

Hunt, A., Ewing, R. and Ghanbarian, B., 2014. Percolation Theory for Flow in Porous Media (Vol. 880): Springer.

Institute for Energy Research. (2011). Haynesville Shale fact sheet. Retrieved from Institute for Energy Research website: http://instituteforenergyresearch.org/wpcontent/ uploads/2012/08/Haynesville-Shale-Fact-Sheet.pdf

I.U.P.A.C., 1994. Recommendations for the characterization of porous solids. Pure Appl. Chem, 66(8), pp.1739-1758.

Ismail, I.M. and Pfeifer, P., 1994. Fractal analysis and surface roughness of nonporous carbon fibers and carbon blacks. Langmuir, 10(5), pp.1532-1538.

Jaroniec, M., 1995. Evaluation of the fractal dimension from a single adsorption isotherm. Langmuir, 11(6), pp.2316-2317.

Jarvie, D.M., 2012. Shale resource systems for oil and gas: Part 2—Shale-oil resource systems.

Javadpour, F., Fisher, D., and Unsworth, M., 2007. Nanoscale gas flow in shale gas sediments. Journal of Canadian Petroleum Technology, 46(10), 55-61

Katz, A.J. and Thompson, A.H., 1987. Prediction of rock electrical conductivity from mercury injection measurements. Journal of Geophysical Research: Solid Earth, 92(B1), 599–607.

Katz, A.J., and Thompson A.H., 1986. Quantitative prediction of permeability in porous rock. Physical Review B, 34, 8179–81.

Killops, S.D., Funnell, R.H., Suggate, R.P., Sykes, R., Peters, K.E., Walters, C., Woolhouse, A.D., Weston, R.J. and Boudou, J.P., 1998. Predicting generation and expulsion of paraffinic oil from vitrinite-rich coals. Org. Geochem. 29(1-3), 1-21.

Klemme, H. D. (1994). Petroleum system of the world involving Upper Jurassic Source Rocks. In AAPG Memoir (Vol. 60). 51-72.

Kuila, U., McCarty, D.K., Derkowski, A., Fischer, T.B., Topór, T. and Prasad, M., 2014. Nano-scale texture and porosity of organic matter and clay minerals in organic-rich mudrocks. Fuel, 135, pp.359-373.

Labani, M.M., Rezaee, R., Saeedi, A. and Al Hinai, A., 2013. Evaluation of pore size spectrum of gas shale reservoirs using low pressure nitrogen adsorption, gas expansion and mercury porosimetry: A case study from the Perth and Canning Basins, Western Australia. Journal of Petroleum Science and Engineering, 112, pp.7-16.

Li, M., Yin, G., Xu, J., Cao, J. and Song, Z., 2016. Permeability evolution of shale under anisotropic true triaxial stress conditions. International Journal of Coal Geology, 165, pp.142-148.

Liu, J., Yao, Y., Liu, D. and Elsworth, D., 2017. Experimental evaluation of CO2 enhanced recovery of adsorbed-gas from shale. International Journal of Coal Geology, 179, pp.211-218.

Makhanov, K., Dehghanpour, H. and Kuru, E., 2013. Measuring liquid uptake of organic shales: A workflow to estimate water loss during shut-in periods. In SPE Unconventional Resources Conference Canada, Calgary, Alberta, Canada. SPE-167157-MS.

Mastalerz, M., Schimmelmann, A., Drobniak, A. and Chen, Y., 2013. Porosity of Devonian and Mississippian New Albany Shale across a maturation gradient: Insights from organic petrology, gas adsorption, and mercury intrusion. AAPG bulletin, 97(10), pp.1621-1643.

Mathia, E.J., Rexer, T.F., Thomas, K.M., Bowen, L. and Aplin, A.C., 2019. Influence of Clay, Calcareous Microfossils, and Organic Matter on the Nature and Diagenetic Evolution of Pore Systems in Mudstones. Journal of Geophysical Research: Solid Earth, 124(1), pp.149-174.

Matyka, M., Khalili, A. and Koza, Z., 2008. Tortuosity-porosity relation in porous media flow. Physical Review E, 78(2), p. 026306.

Morrow, N.R., 1990. Wettability and its effect on oil recovery. Journal of Petroleum Technology, 42(12), 1476–1484.

Nelson, P.H., 2009. Pore-throat sizes in sandstones, tight sandstones, and shales. AAPG Bulletin, 93(3), 329–340.

Odusina, E.O., Sondergeld, C.H. and Rai, C.S., 2011. NMR study of shale wettability. In The Canadian Unconventional Resources Conference, Alberta, Canada. Society of Petroleum Engineers. SPE-147371-MS.

Oil & Gas Journal. (2018). Goodrich to commence completion operations in Haynesville. https://www.ogj.com/articles/2018/03/goodrich-to-commence-completionoperations-in-haynesville.html

Peters, K.E. and Cassa, M.R., 1994. Applied source rock geochemistry: L.B. Magoon, W.G. Dow (Eds.), The Petroleum System – From Source to Trap, AAPG Memoir 60. 93-120.

Ross, D.J. and Bustin, R.M., 2009. The importance of shale composition and pore structure upon gas storage potential of shale gas reservoirs. Marine and petroleum Geology, 26(6), pp.916-927.

Salathiel, R., 1973. Oil recovery by surface film drainage in mixed-wettability rocks. Journal of Petroleum Technology, 25, 1216–1224.

Slatt, R.M. and O'Brien, N.R., 2011. Pore types in the Barnett and Woodford gas shales: Contribution to understanding gas storage and migration pathways in fine-grained rocks. AAPG bulletin, 95(12), pp.2017-2030.

Soeder, D.J., 1988. Porosity and permeability of eastern Devonian gas shale. SPE Formation Evaluation, 3(01), pp.116-124.

Stauffer, D., and Aharony, A., 1994. Introduction to Percolation Theory. 2nd ed., Taylor and Francis, London.

Takahashi, S. and Kovscek, A.R., 2010. Wettability estimation of low-permeability, siliceous shale using surface forces. Journal of Petroleum Science and Engineering, 75(1), 33–43.

U.S. Energy Information Administration. (2011). Review of Emerging Resources: U.S. Shale Gas and Shale Oil Plays. U.S. Energy Information Administration Report, (July), 105. Retrieved from ftp://ftp.eia.doe.gov/natgas/usshaleplays.pdf

Wang, S., Javadpour, F. and Feng, Q., 2016. Confinement correction to mercury intrusion capillary pressure of shale nanopores. Scientific Reports, 6: 20160, doi: 10.1038/srep20160.

Washburn, E.W., 1921. Note on a method of determining the distribution of pore sizes in a porous material. Proceedings of National Academy of Sciences in the United States of America, 7, 115–116.

Webb, P.A., 2001. An introduction to the physical characterization of materials by mercury intrusion porosimetry with emphasis on reduction and presentation of experimental data. Micromeritics Instrument Corporation, Norcross, GA. Instrument Corporation, 22 pp.

Wu, Y., Tahmasebi, P., Lin, C., Zahid, M.A., Dong, C., Golab, A.N. and Ren, L., 2019. A comprehensive study on geometric, topological and fractal characterizations of pore systems in low-permeability reservoirs based on SEM, MICP, NMR, and X-ray CT experiments. Marine and Petroleum Geology, 103, pp.12-28.

Yang, R., Hao, F., He, S., He, C., Guo, X., Yi, J., Hu, H., Zhang, S. and Hu, Q., 2017. Experimental investigations on the geometry and connectivity of pore space in organic-rich Wufeng and Longmaxi shales. Marine and Petroleum Geology, 84, 225–242.

Zhou, S., Liu, D., Karpyn, Z.T., Cai, Y. and Yao, Y., 2018. Effect of coalification jumps on petrophysical properties of various metamorphic coals from different coalfields in China. Journal of Natural Gas Science and Engineering, 60, pp.63-76.

Zhou, S., Yan, G., Xue, H., Guo, W. and Li, X., 2016. 2D and 3D nanopore characterization of gas shale in Longmaxi formation based on FIB-SEM. Marine and Petroleum Geology, 73, pp.174-180.

Chapter 5: Conclusions

In this dissertation, experimental studies with different techniques are applied to investigate nano- and micropore structures (geometry and topology) and their interactions with different fluids for different shale samples of Woodford, Haynesville, and Pearsall formations. For API brine and DI water, we observed low to moderate wettability, and spontaneous imbibition tests showed a low pore connectivity slope, typical of sparsely connected hydrophilic pore networks. Edge-accessible pore throat distribution measured by spontaneous tracer imbibition and high-pressure intrusion display a steep decline in accessible porosity with distance from the sample's external periphery, which indicates that only a small number of the inner pores are connected to the sample pores on edge.

Results from Chapter 3 showed that pores within the Woodford Shale are predominantly in the nanometer size range, with a median pore throat diameter ranging from 3.7-5.4 nm, which is consistent with other shale basins. Based on these geometrical properties (narrow pore throat diameter, very low porosity, 0.8 to 4%, and 0.5-1.97 nD matrix permeability), the Woodford Shale is predicted to display restricted fluid flow. In chapter 4 using low-pressure N_2 gas adsorption, high-pressure mercury intrusion and vacuum saturation of a suite of Haynesville and Pearsall Shale samples reveal differences in pore structure that in turn will affect both gas storage and transport properties. Carbonate-dominated samples showed low pore volumes observed by both MICP and N_2 absorption tests. Experimental data reveal that clay and quartz+feldspar based samples have mainly nanometer size pore throat diameter, whereas samples with carbonate based lithology have micrometer size pore throat diameters. Raman spectroscopy in Chapter 3 represents an alternative method for the assessment of the thermal

maturity of shale samples. The experimental results on the shales demonstrate that with an increase in thermal maturity, D1 and G peaks shift towards lower and higher wavelengths respectively, which increases the Raman band separation (RBS). We can gauge the thermal maturity of shales by a curve fitting method for unknown samples using laser Raman spectroscopy. All these correlations show that with the aid of Raman spectroscopy alone, the maturation windows for immature kerogen, oil, wet gas, and dry gas can be evaluated for unknown samples. Raman spectra can be generated directly on drill cores and cutting chips without any sample preparation (only need to remove/washing drilling mud). Further data mining of Raman spectra collection from different basin samples will be needed to refine and establish a fast, less strenuous than vitrinite reflectance and quantitative method for measuring thermal maturity of unconventional petroleum prospects.

This study combined MIP, N_2 gas physisorption, vacuum saturation, wettability, imbibition and understanding thermal maturation over a wide pore length range from micrometer scale (~50 μm) to nanometer scale (2.8 nm). This research bridges the gap between pore structure, pore connectivity, and wettability characteristics of three shale plays. The results demonstrate that wettability and pore structure may be the most important constraints on petroleum movement and production. Nano-sized pore throats and mixed wettability characteristics may be the reasons for rapid production declines in shale hydrocarbon extraction.